UNIVERSITY OF LIVERPOOL

Atomic layer deposition zinc oxide devices for transparent electronics

Thesis submitted in accordance with the requirements of the University of Liverpool for the degree of Doctor in Philosophy in the Faculty of Science and Engineering by

Andrew Shaw

June 2018

Department of Electrical Engineering and Electronics

Abstract

Zinc oxide (ZnO) films deposited using atomic layer deposition (ALD) and plasma enhanced (PE)-ALD for transparent electronics have been explored in this thesis by characterising the films electrically and physically. Thin-film transistors (TFTs) and Schottky diodes have been successfully demonstrated using ALD based thin-films as active layers. The challenge of reducing the intrinsically high conductivity is addressed through two approaches namely the use of substitutional dopants via ALD and tuning of the plasma conditions during PEALD deposition.

Initial characterisation established that using Mg as a substitutional alloy, reduced the films conductivity. TFTs were fabricated using lithography, on highly doped Si wafers with thermally grown SiO_2 as the gate oxide. The effect of using Mg was to reduce the off-current by a factor of 10^5. An optimum ratio between the Mg and Zn precursor of 12.5 % was established, defined by a maximum saturation mobility (μ_{sat}) of 4 cm^2/Vs. In addition, the band gap of the Mg doped ZnO film increased from 3.3 eV to 3.44 eV, through the formation of MgO states within the film.

The first instance of Nb doped ZnO for TFTs applications are reported in this thesis. TFTs were fabricated in the same manner as for Mg doped ZnO, however, a capping layer of 5 nm of Al_2O_3 prior to NbZnO deposition was required to mitigate gate oxide leakage and improve the interface quality. Optimal characteristics were achieved with a lower ratio of 3.8 % between the Nb and Zn precursor. A maximum μ_{sat} of 8 cm^2/Vs was achieved. The higher mobility and lower precursor percentages for Nb originate from the higher oxidation state of the dopant. A lower sub-threshold swing of 220 mV/dec was achieved for Nb doped films compared to 900 mV/dec for Mg doped films, supporting the advantage of using Nb to control the conductivity of ZnO ALD thin-films for TFT applications. In addition, the sub-band gap states in ZnO film was modelled from current-voltage and capacitance-voltage measurements, where good correlation between both techniques was achieved.

Optimisation of PEALD ZnO for Schottky diode applications was established with a deposition temperature of 80 ^oC and plasma time of 50 s. The use of oxidised metals for the Schottky contact, namely Ag_xO and PtO_x was required to obtain good Schottky parameters. These contact metals aim to mitigate the oxygen deficiencies at surface of ZnO. Relatively low ideality factors of < 1.4 are achieved using both Schottky contacts. Thermionic emission was established as the dominant conduction mechanism. The relatively large ideality factors are thought to originate from the polycrystalline nature of the ZnO film.

Contents

List of Figures

List of Tables

List of Publications

Conference Presentations

1. **Physical and electrical characterization of Mg-doped ZnO thin-film transistors**
   A. Shaw, T. J. Whittles, I. Z. Mitrovic, J. D. Jin, J. S. Wrench, D. Hesp, V. R. Dhanak, P. R. Chalker, S. Hall
   45th European Solid State Device Research Conference (ESSDERC), pp. 206-209, Graz, Austria, 14th-18th September 2015

2. **Controlling the physical and electrical properties of ALD grown ZnO using Nb as a dopant**
   A. Shaw, J. D. Jin, I. Z. Mitrovic, S. Hall, J. S. Wrench, P. R. Chalker
   Joint International EUROSOI Workshop and International Conference on Ultimate Integration on Silicon (EUROSOI-ULIS), pp. 28-31, Vienna, Austria, 25th-27th January 2016

3. **Extraction of the sub-band gap density of states of Nb doped ZnO thin film transistors using C-V measurements**
   A. Shaw, J. D. Jin, I. Z. Mitrovic, S. Hall, J. S. Wrench and P. R. Chalker
   20th Insulating Films on Semiconductors (INFOS), Postdam, Germany, 27th-30th June 2017

Journal Papers

1. **Compositional tuning of atomic layer deposited MgZnO for thin film transistor**
   J. S. Wrench, I. F. Brunell, P. R. Chalker, J. D. Jin, **A. Shaw**, I. Z. Mitrovic and S. Hall, *Applied Physics Letters*, vol. 105, pp. 201209, 2014
   DOI: http://dx.doi.org/10.1063/1.4902389

2. **Atomic layer deposition of Nb-doped ZnO for thin film transistors**
   A. Shaw, J. S. Wrench, J. D. Jin, T. J. Whittles, I. Z. Mitrovic, M. Raja, V. R. Dhanak, P. R. Chalker, and S. Hall
   Applied Physics Letters, vol. 109, pp. 222103, 2016
   DOI: http://dx.doi.org/10.1063/1.4968194

3. **Schottky Diodes on ZnO Thin Films Grown by Plasma-Enhanced Atomic Layer Deposition**

   J. D. Jin, J. S. Wrench, J. T. Gibbon, D. Hesp, **A. Shaw**, I. Z. Mitrovic, N. Sedghi, L. J. Phillips, J. Zou, V. R. Dhanak, P. R. Chalker and S. Hall

   IEEE Transactions on Electron Devices, vol. 64, no. 3, pp. 1225-1230, 2017

   DOI: 10.1109/TED.2016.2647284

4. **Extraction of the sub-band gap density of states of Nb doped ZnO thin film Transistors using C - V measurements**

   A. Shaw, J. D. Jin, I. Z. Mitrovic, S. Hall, J. S. Wrench, P.R. Chalker

   Microelectronic Engineering, vol. 178, pp. 213-216, 2017

   DOI: https://doi.org/10.1016/j.mee.2017.05.043

5. **A high speed PE-ALD ZnO Schottky diode rectifier with low interface-state density**

   J. D. Jin, J. Zhang, **A. Shaw**, V. N. Kudina, I. Z. Mitrovic, J. S. Wrench, P. R. Chalker, C. Balocco, A. Song and S. Hall

   Journal of Physics D: Applied Physics, vol. 51, no. 6, pp. 065102, 2018

   DOI: https://doi.org/10.1088/1361-6463/aaa4a2

Acknowledgements

There are a number of people who I would like to thank for their help during my time for this PhD. Firstly, I would like to thank my supervisor Professor Steve Hall for his guidance and supervision.

Also, I would like to thank the project team for the support provided, Dr Ivona Mitrovic, Dr Jidong Jin, Professor Paul Chalker and Dr Jacqueline Wrench for whom this PhD would not have been possible. I would like to thank Dr Vin Dhanak's group in the Stevenson Institute at The University of Liverpool for their contribution to the XPS measurements and analysis.

Finally, I would like to thank the EPSRC for funding my PhD.

Chapter 1

1. Introduction

Ever since the invention of the transistor and integrated circuits, the methodology of reducing device dimensions to improve performance and capability has been the overriding goal. This trend is described by Moore's law [1] where the number of transistors per integrated circuit doubles approximately every 18 months. However, in 2009, the International Technology Roadmap for Semiconductors (ITRS) predicted the slowing down of Moore's law and importance of alternative areas of interest, which were subsequently added to the Roadmap. These additional branches of interest focus on applications that do not have to follow Moore's law but add value to the end user with the main groups of bio-applications, passives, high voltage power, analogue/RF and sensors. They fall under the category known as 'More than Moore's law'. A pictorial representation of the ITRS is shown in Fig. 1.1.

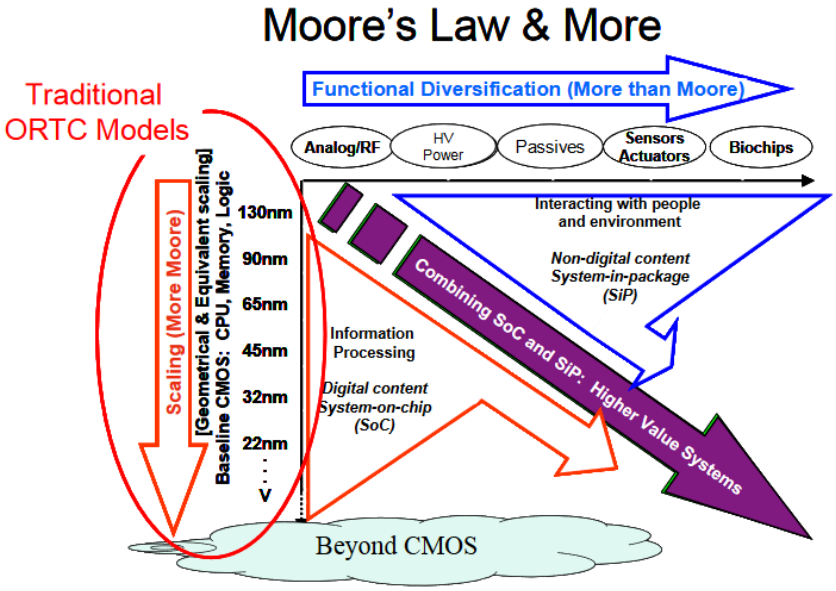

Fig. 1.1 ITRS 2009 Moore's Law and More [2]

Since the turn of the millennium, the realisation to protect the desired trend of new emerging technologies has driven the requirement of extensive research into novel materials and structures. Through the advancement of deposition techniques, new materials such as carbon nanotubes, graphene and wide band gap semiconductors have been realised whilst providing potential new applications such as transparent electronics and new high-power applications. The advancement of large area electronics, predominantly driven by display manufacturers, requires low cost production of thin-film transistors (TFTs) for active matrix driving circuits. Currently hydrogenated amorphous silicon (a-Si:H) and polycrystalline silicon (poly-Si) are widely used as the active layer [3, 4], however, that technology cannot sustain the continual improvement of performance required. In particular, there is a requirement for transistors with

sufficient drive capability to realise both pixel and peripheral driver transistors on the same panel. Along with solar technology, these have been some of the driving factors for the development of new semiconductors. Metal oxide materials have been at the forefront of research into TFTs which have been based on zinc oxide (ZnO) and indium oxide (In_2O_3) [5-7]. Transistors based on this technology can satisfy the performance requirement for fully integrated displays. Currently the most research effort into metal oxide semiconductor development is on indium-gallium-zinc-oxide (IGZO) and was commercialised in 2012 [8] for back panel display technology by Sharp Corporation. Moreover, there is an economic motivation for the removal of the dominance of indium and gallium which are expensive; this presents a driving force for the work in this thesis. Moreover, another motivation of the removal of indium is due to its toxicity levels and is considered as a carcinogen [9].

ZnO belongs to the II-VI compound semiconductor family and is a highly versatile material. It exists typically in a wurtzite phase with a large direct band gap of ~ 3.3 eV [10]. Furthermore, it has a large exciton energy of ~ 60 meV, ideal for LED applications. ZnO is intrinsically an n-type semiconductor with a relatively large electron mobility compared to amorphous Si and competitive with poly-Si. It is transparent in the optical spectrum, hence attractive for display and other semiconductor applications.

Since the invention of TFTs in the 1950s, ZnO has been considered as a potential candidate for the active layer with considerable research having been conducted in the 1960s [11]. However, the focus shifted away from ZnO with the discovery of hydrogenated amorphous silicon (a-Si:H) until the early 2000s, when Nomura *et al.* [5] successfully demonstrated IGZO active layers with considerably higher electron mobilities > 10 cm^2/Vs. ZnO based materials routinely have electron mobility > 10 cm^2/Vs, whereas a-Si:H ~ 1 cm^2/Vs [4] and poly-Si < 13 cm^2/Vs [3]. Although poly-Si has reasonable electron mobilities, it requires deposition temperature exceeding 600 ^oC. In comparison ZnO can be deposited at relatively low temperatures (< 200 ^oC) presenting the prospect of using plastic substrates for flexible displays. Currently polymers such as Pentacene have a hole mobility < 5 cm^2/Vs for vapour deposited [12] and ~ 1 cm^2/Vs for solution processed material [13, 14]. In comparison with these alternatives, ZnO based materials are one of the main candidates with the advantage of optically transparent devices.

An advantage of ZnO is the range of low temperature deposition techniques available (< 200 ^oC) including; atomic layer deposition (ALD) [15, 16], pulse layer deposition [17], metal organic chemical vapour deposition [18, 19], sputtering [20, 21] and solution processing [22]. Among these techniques, sputtering and solution processing can be achieved at room temperature, ideal for plastic substrates. Along with low deposition temperatures,

ALD films have a high degree of controllability in relation to film composition, highly uniform layers for complex surface morphologies and low surface roughness.

Since the publication of IGZO TFTs by Nomura *et al.* [5], this material has come to the forefront of transparent conductive oxide (TCO) technology for active layers in TFT applications. Currently the state of the art of IGZO TFTs can achieve a saturation mobility > 20 cm^2/Vs, low threshold voltages < 1 V and subthreshold swing < 200 mV [23-26]. Although these characteristics are ideal for active matrix displays, the use of indium is undesirable due to the low abundance in the Earth's crust and volatility of the cost over the last decade [27]. Therefore, research into alternative ZnO base thin-films without the use of indium for TFTs has exploded [20, 28-30]. A range of solutions have been proposed such as sputtered ZnO for which high mobilities > 50 cm^2/Vs are achievable [20].However, stability of the films remains a challenge. Alternatively, different dopants have been utilised to reduce the native defects within ZnO to achieve the desired conductivity. Dopants such as gallium and silicon [31-34] have been explored but these films suffer from saturation mobilities below 1 cm^2/Vs. To date ALD ZnO films prove challenging for TFT applications due to the inherently high conductivity, resulting in a low on/off ratio and saturation mobility.

For Schottky diodes, ZnO has received similar interest as IGZO based Schottky diodes. The best performing diodes are based on hydrothermally grown bulk ZnO material, where high controllability of the effective carrier concentration is achievable. More importantly the challenge has been to provide a good interface between the ZnO and the Schottky contact. ZnO suffers from a high density of oxygen vacancies at the metal-semiconductor interface resulting in Fermi-level pinning. Hence, it is common for the theoretical barrier height to be greater than 0.2 eV compared to the measured value. To offset the effect of Fermi-level pinning, Allen *et al*. [35] proposed the use of slightly oxidised metal such as silver oxide, platinum oxide and palladium oxide. The effect of using an oxygen rich environment to deposit these metals is that it helps to alleviate the oxygen deficiencies at the surface of ZnO and therefore, reduce the effect of Fermi-level pinning.

Although the Schottky characteristics for bulk ZnO can achieve low ideality factors, the integration of these thin film ZnO for the transparent electronics industry remain an area of significant interest. There is limited research into Schottky contacts on non-bulk grown ZnO which can achieve low ideality factors; however, evaporated [36, 37] and pulse layer deposition (PLD) [38, 39] are the preferred deposition methods. For both methods, annealing in air or O_2 has been shown to reduce the surface oxygen deficiencies. ZnO based Schottky diodes deposited by ALD or PEALD, over recent years, have seen significant improvement where the ideality factors have reduced from > 4 to approximately 2.5 [40, 41]. However,

these large ideality factors present the need for further research into the improvement of Schottky contacts on ALD/PEALD based ZnO.

In summary, the use of ALD ZnO based thin-films remains a distinct challenge where the reduction of the conductivity is the primary goal for both TFT and Schottky diode applications. The primary focus of this thesis is to explore and realise the potential of ZnO thin-films deposited by ALD and PEALD for TFTs and Schottky diodes by optimising the deposition conditions. Two avenues are investigated in this thesis; doping ZnO with metals to replace the Zn ions within the ZnO matrix and the effect of plasma conditions and deposition temperatures are investigated for improving the Schottky diode performance.

The structure of this thesis is outlined as follows. Chapter 2 provides an extensive literature review into the state of the art performance of ZnO based TFTs and Schottky didoes. The basic operation of TFTs and Schottky diodes is also presented. Chapter 3 introduces the experimental techniques used throughout this thesis, required for the fabrication of the devices, thin film characterisation and electrical characterisation. Chapter 4 presents the feasibility of using magnesium as a dopant for improving the electrical characteristics of ZnO TFTs. Along with electrical characterisation, the effect on the physical properties of the ZnO thin-film with increasing magnesium concentrations is also investigated. Chapter 5 investigates the effect of ALD ZnO films doped with niobium, where the physical and electrical properties are examined. Chapter 6 demonstrates the effectiveness of using plasma enhanced ALD (PEALD) ZnO films for Schottky diodes using oxidised silver and platinum. Finally, the conclusions and suggestions for potential future work are presented in chapter 7.

1.1. References

[1] G. E. Moore, "Cramming more components onto integrated circuits, Reprinted from Electronics, volume 38, number 8, April 19, 1965, pp.114," *IEEE Solid-State Circuits Society Newsletter,* vol. 11, no. 5, pp. 33-35, 2006.

[2] ITRS, "International Technology Roadmap For Semiconductors 2009 Edition Executive Summary ", 2009. Accessed on: 08/09/2017, Available: https://www.dropbox.com/sh/ia1jkem3v708hx1/AAB1fo1HrYIKClJNk0dB7YrCa?dl=0&preview=1_Executive+Summary.pdf

[3] S. D. Brotherton, "Polycrystalline silicon thin film transistors," *Semiconductor Science and Technology,* vol. 10, no. 6, p. 721, 1995.

[4] R. A. Street, "Thin-Film Transistors," *Advanced Materials,* vol. 21, no. 20, pp. 2007-2022, 2009.

[5] K. Nomura, H. Ohta, A. Takagi, T. Kamiya, M. Hirano, and H. Hosono, "Room-temperature fabrication of transparent flexible thin-film transistors using amorphous oxide semiconductors," *Nature,* 10.1038/nature03090 vol. 432, no. 7016, pp. 488-492, 2004.

[6] T. Kamiya, K. Nomura, and H. Hosono, "Present status of amorphous In–Ga–Zn–O thin-film transistors," *Science and Technology of Advanced Materials,* vol. 11, no. 4, p. 044305, 2010.

[7] H. Yabuta, M. Sano, K. Abe, T. Aiba, T. Den, H. Kumomi, K. Nomura, T. Kamiya, and H. Hosono, "High-mobility thin-film transistor with amorphous $InGaZnO_4$ channel fabricated by room temperature rf-magnetron sputtering," *Applied physics letters,* vol. 89, no. 11, p. 112123, 2006.

[8] Sharp. (2012, 01/08/2017). *Sharp Begins Production of World's First LCD Panels Incorporating IGZO Oxide Semiconductors*. Available: http://www.sharp-world.com/corporate/news/120413.html

[9] D. R. Lide, "Magnetic susceptibility of the elements and inorganic compounds," in *CRC Handbook of Chemistry and Physics* 86th ed. Boca Raton (FL): CRC Press, 2005.

[10] Ü. Özgür, Y. I. Alivov, C. Liu, A. Teke, M. A. Reshchikov, S. Doğan, V. Avrutin, S.-J. Cho, and H. Morkoç, "A comprehensive review of ZnO materials and devices," *Journal of Applied Physics,* vol. 98, no. 4, p. 041301, 2005.

[11] G. F. Boesen and J. E. Jacobs, "ZnO field-effect transistor," *Proceedings of the IEEE,* vol. 56, no. 11, pp. 2094-2095, 1968.

[12] N. Wrachien, A. Cester, D. Bari, G. Meneghesso, J. Kovac, J. Jakabovic, M. Sokolsky, D. Donoval, and J. Cirak, "Low-energy UV effects on Organic Thin-Film-Transistors," in *2011 International Reliability Physics Symposium*, 2011, pp. 2E.2.1-2E.2.8.

[13] S. K. Park, T. N. Jackson, J. E. Anthony, and D. A. Mourey, "High mobility solution processed 6,13-bis(triisopropyl-silylethynyl) pentacene organic thin film transistors," *Applied Physics Letters,* vol. 91, no. 6, p. 063514, 2007.

[14] M. Raja, D. Donaghy, R. Myers, and B. Eccleston, "Impact of universal mobility law on polycrystalline organic thin-film transistors," *Journal of Applied Physics,* vol. 112, no. 8, p. 084503, 2012.

[15] T. Tynell and M. Karppinen, "Atomic layer deposition of ZnO: a review," *Semiconductor Science and Technology,* vol. 29, no. 4, p. 043001, 2014.

[16] E. Guziewicz, M. Godlewski, L. Wachnicki, T. Krajewski, G. Luka, S. Gieraltowska, R. Jakiela, A. Stonert, W. Lisowski, and M. Krawczyk, "ALD grown zinc oxide with controllable electrical properties," *Semiconductor Science and Technology,* vol. 27, no. 7, p. 074011, 2012.

[17] R. D. Vispute, V. Talyansky, S. Choopun, R. P. Sharma, T. Venkatesan, M. He, X. Tang, J. B. Halpern, M. G. Spencer, Y. X. Li, L. G. Salamanca-Riba, A. A. Iliadis, and K. A. Jones, "Heteroepitaxy of ZnO on GaN and its implications for fabrication of hybrid optoelectronic devices," *Applied Physics Letters,* vol. 73, no. 3, pp. 348-350, 1998.

[18] K. Black, A. C. Jones, P. R. Chalker, J. M. Gaskell, R. T. Murray, T. B. Joyce, and S. A. Rushworth, "MOCVD of ZnO thin films for potential use as compliant layers for GaN on Si," *Journal of Crystal Growth,* vol. 310, no. 5, pp. 1010-1014, 2008.

[19] N. M. Sbrockey and S. Ganesan, "ZnO thin films by MOCVD," *III-Vs Review,* vol. 17, no. 7, pp. 23-25, 2004.

[20] C. Brox-Nilsen, J. Jin, Y. Luo, P. Bao, and A. M. Song, "Sputtered ZnO Thin-Film Transistors With Carrier Mobility Over 50 cm^2/Vs," *IEEE Transactions on Electron Devices,* vol. 60, no. 10, pp. 3424-3429, 2013.

[21] E. M. C. Fortunato, P. M. C. Barquinha, A. C. M. B. G. Pimentel, A. M. F. Gonçalves, A. J. S. Marques, R. F. P. Martins, and L. M. N. Pereira, "Wide-bandgap high-mobility ZnO thin-film transistors produced at room temperature," *Applied Physics Letters,* vol. 85, no. 13, pp. 2541-2543, 2004.

[22] B. S. Ong, C. Li, Y. Li, Y. Wu, and R. Loutfy, "Stable, Solution-Processed, High-Mobility ZnO Thin-Film Transistors," *Journal of the American Chemical Society,* vol. 129, no. 10, pp. 2750-2751, 2007.

[23] M. K. Dai, J. T. Lian, T. Y. Lin, and Y. F. Chen, "High-performance transparent and flexible inorganic thin film transistors: a facile integration of graphene nanosheets and amorphous InGaZnO," *Journal of Materials Chemistry C,* 10.1039/C3TC30890A vol. 1, no. 33, pp. 5064-5071, 2013.

[24] H. Oh, K. Cho, S. Park, and S. Kim, "Electrical characteristics of bendable a-IGZO thin-film transistors with split channels and top-gate structure," *Microelectronic Engineering*, vol. 159, pp. 179-183, 2016.

[25] N. C. Su, S. J. Wang, C. C. Huang, Y. H. Chen, H. Y. Huang, C. K. Chiang, and A. Chin, "Low-Voltage-Driven Flexible InGaZnO Thin-Film Transistor With Small Subthreshold Swing," *IEEE Electron Device Letters*, vol. 31, no. 7, pp. 680-682, 2010.

[26] M. J. Yu, Y. H. Yeh, C. C. Cheng, C. Y. Lin, G. T. Ho, B. C. M. Lai, C. M. Leu, T. H. Hou, and Y. J. Chan, "Amorphous InGaZnO Thin-Film Transistors Compatible With Roll-to-Roll Fabrication at Room Temperature," *IEEE Electron Device Letters*, vol. 33, no. 1, pp. 47-49, 2012.

[27] ECORYS, "Mapping resource prices: the past and the future," 2012.

[28] L. Zhang, J. Li, X. W. Zhang, D. B. Yu, X. Y. Jiang, and Z. L. Zhang, "Glass-substrate-based high-performance ZnO-TFT by using a Ta2O5 insulator modified by thin SiO2 films," *physica status solidi (a)*, vol. 207, no. 8, pp. 1815-1819, 2010.

[29] W.-Y. Chen, J.-S. Jeng, and J.-S. Chen, "Improvement of Mobility in ZnO Thin Film Transistor with an Oxygen Enriched MgO Gate Dielectric," *ECS Solid State Letters*, vol. 1, no. 5, pp. N17-N19, 2012.

[30] C. I. Kuan, H. C. Lin, P. W. Li, and T. Y. Huang, "High-Performance Submicrometer ZnON Thin-Film Transistors With Record Field-Effect Mobility," *IEEE Electron Device Letters*, vol. 37, no. 3, pp. 303-305, 2016.

[31] W. J. Park, H. S. Shin, B. D. Ahn, G. H. Kim, S. M. Lee, K. H. Kim, and H. J. Kim, "Investigation on doping dependency of solution-processed Ga-doped ZnO thin film transistor," *Applied Physics Letters*, vol. 93, no. 8, p. 083508, 2008.

[32] V. Bhosle, A. Tiwari, and J. Narayan, "Electrical properties of transparent and conducting Ga doped ZnO," *Journal of Applied Physics*, vol. 100, no. 3, p. 033713, 2006.

[33] S.-H. Lee, K.-W. Cha, and J.-S. Park, "Effects of furnace annealing and hot pressing on the properties of SZO thin films and on the characteristics of SZO-TFTs," *Thin Solid Films*, vol. 596, pp. 72-76, 2015.

[34] L. Yu-Rong, Z. Gao-Wei, L. Pai-To, and Y. Ruo-He, "Improvement in the electrical performance and bias-stress stability of dual-active-layered silicon zinc oxide/zinc oxide thin-film transistor," *Chinese Physics B*, vol. 25, no. 8, p. 088503, 2016.

[35] M. W. Allen, M. M. Alkaisi, and S. M. Durbin, "Metal Schottky diodes on Zn-polar and O-polar bulk ZnO," *Applied Physics Letters*, vol. 89, no. 10, p. 103520, 2006.

[36] D. Somvanshi and S. Jit, "Mean Barrier Height and Richardson Constant for Pd/ZnO Thin Film-Based Schottky Diodes Grown on n-Si Substrates by Thermal Evaporation Method," *IEEE Electron Device Letters*, vol. 34, no. 10, pp. 1238-1240, 2013.

[37] G. M. Ali, A. D. D. Dwivedi, S. Singh, and P. Chakrabarti, "Interface properties and junction behavior of Pd contact on ZnO thin film grown by vacuum deposition technique," *physica status solidi (c)*, vol. 7, no. 2, pp. 252-255, 2010.

[38] H. Frenzel, A. Lajn, H. von Wenckstern, G. Biehne, H. Hochmuth, and M. Grundmann, "ZnO-based metal-semiconductor field-effect transistors with Ag-, Pt-, Pd-, and Au-Schottky gates," *Thin Solid Films*, vol. 518, no. 4, pp. 1119-1123, 2009.

[39] H. v. Wenckstern, G. Biehne, R. A. Rahman, H. Hochmuth, M. Lorenz, and M. Grundmann, "Mean barrier height of Pd Schottky contacts on ZnO thin films," *Applied Physics Letters*, vol. 88, no. 9, p. 092102, 2006.

[40] T. A. Krajewski, G. Luka, L. Wachnicki, A. J. Zakrzewski, B. S. Witkowski, M. I. Lukasiewicz, P. Kruszewski, E. Lusakowska, R. Jakiela, M. Godlewski, and E. Guziewicz, "Electrical parameters of ZnO films and ZnO-based junctions obtained by atomic layer deposition," *Semiconductor Science and Technology*, vol. 26, no. 8, p. 085013, 2011.

[41] M. Shen, A. Afshar, Y. Y. Tsui, K. C. Cadien, and D. W. Barlage, "Performance of Nanocrystal ZnO Thin-Film Schottky Contacts on Cu by Atomic Layer Deposition," *IEEE Transactions on Nanotechnology*, vol. 16, no. 1, pp. 135-139, 2017.

Chapter 2

2. Literature review and background

The general topics and background outlined within this thesis are discussed in this chapter; zinc oxide, thin-film transistors and Schottky diodes. Also presented is an overview of the relevant literature of the state of the art for the respective devices, relevant in this thesis.

2.1. Zinc oxide

Zinc oxide (ZnO) is a highly versatile transparent conducting oxide with a large direct band gap ~ 3.3 eV and an exciton binding energy 60 meV, which is highly advantageous for optoelectronics [1, 2]. An exciton is a bound electron-hole pair, which occurs just below the conduction band edge. On annihilation of this pair, a photon is released with an energy equal to the band gap minus the exciton energy. The large exciton energy is advantageous as it enables emission at room temperature and higher, which in turn provides the prospect of the use of ZnO for LEDs and lasers in the UV spectrum. The resurgence in the use of ZnO is mainly due to the improved quality of the fabrication of films and single crystal bulk structures. ZnO is an intrinsic n-type semiconductor with an extensive range of conducting properties from almost metal-like to insulator-like. This versatile range is controlled by deposition techniques, impurity doping and annealing [3-5], hence the possibility of an electronic device fabricated from ZnO based materials resulting in fully transparent devices.

Controlling the conductivity of ZnO by doping or alloying is commonly achieved by using metals such as Al, Ga and In [2, 6, 7] which replace Zn atoms within the lattice structure. However, achieving p-type ZnO is highly challenging due to the lack of availability of suitable dopants [1, 2, 8]. Typically, dopants such as Li or Na produce large concentrations of deep states that do not contribute to conductivity [1, 2]. Moreover, these donors have significantly different atomic radii to that of Zn resulting in large energies to act as a substitutional donor [8]. A limited number of studies are reported for achieving p-type doping ZnO with nitrogen [9], but the reproducibility remains questionable. An added advantage of doping ZnO is the ability to tailor the band gap, through the alloying process. Notably the use of Mg and Ca can achieve wider band gaps of over 4 eV [10]. The underlying origins of n-type conductivity of ZnO originate from the defects within the crystal lattice due to zinc interstitials, oxygen vacancies [11] and contamination of hydrogen [12]. The zinc interstitials account for defects with high energy near to the conduction band, whereas oxygen vacancies are associated with defects of lower energies towards the valence band.

The crystal structures for ZnO are rocksalt (B1), zinc blende (B3) and wurtzite (B4) as shown in Fig. 2.1 (a-c) respectively. Rocksalt crystal can only be grown under relatively high pressures, whereas, zinc blende crystals are only stable on cubic substrates. Under ambient conditions ZnO is typically deposited with a wurtzite crystal structure and is stable [1].

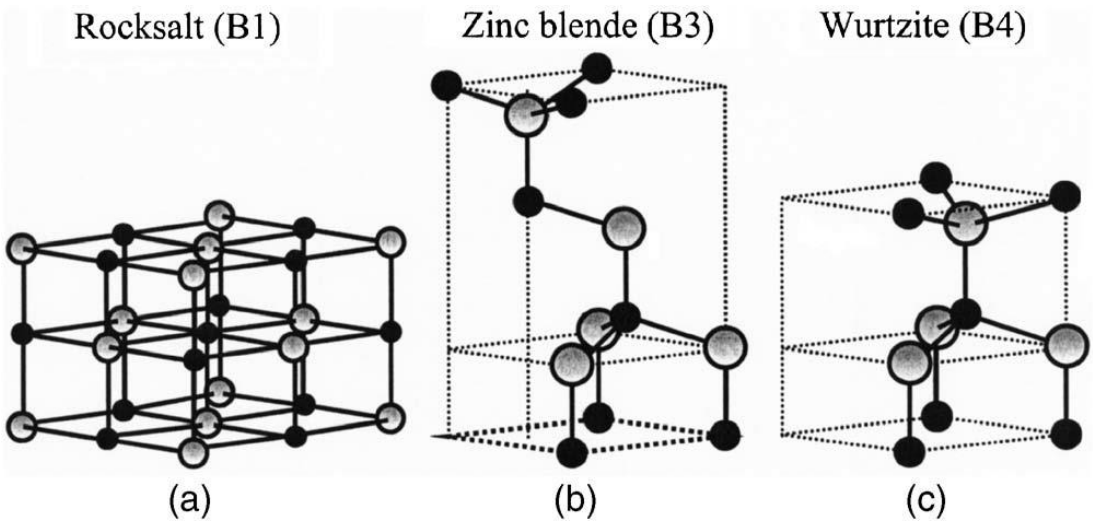

Fig. 2.1 Stick and ball representation of ZnO crystal structures: (a) cubic rocksalt (B1), (b) cubic zinc blende (B3) and (c) hexagonal wurtzite (B4). The shaded and black spheres denote Zn and O atoms, respectively [1].

High quality ZnO thin-films are deposited by a variety of techniques including; RF sputtering, metal-organic chemical vapour deposition (MOCVD), pulse laser deposition (PLD), molecular beam epitaxy (MBE) and atomic layer deposition (ALD). MOCVD [13], MBE [14] and PLD [15] thin-films are preferable for ultra-high quality epitaxial deposited ZnO required for optoelectronic applications. Conversely RF sputtered [16] and ALD [5] thin-films are typically polycrystalline. RF sputtered ZnO remains the preferred deposition technique due to the scalability of deposition, room temperature and potentially high mobilities [2, 16]. ALD films are inherently conductive in comparison to sputtered films. To control the conductivity of ZnO thin-film deposited by ALD three factors are considered; deposition temperature, substitutional doping and the use of plasma processing [5, 17, 18].

2.2.Thin-film transistors

Thin-film transistors (TFTs) were first developed in the 1960s with a similar principle of modulating the channel as metal-oxide semiconductor field effect transistors (MOSFETs). However, the distinct difference between the two devices is MOSFETs operate in inversion mode whereas TFTs are in accumulation.

2.2.1 Device structure

The four-main device topologies for TFTs are shown in Fig. 2.2 (a) top gate bottom contact, (b) top gate top contact, (c) bottom gate bottom contact and (d) bottom gate top contact, where S and D refers to the source and drain contacts respectively. In this thesis, all TFT devices are fabricated with the device structure shown in Fig. 2.2(d).

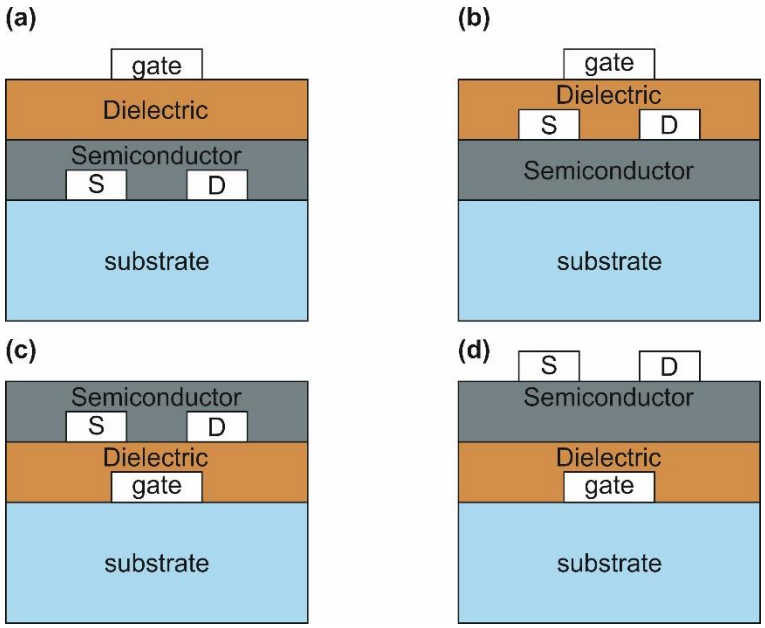

Fig. 2.2 TFT device structures (a) top gate bottom contact, (b) top gate top contact, (c) bottom gate bottom contact and (d) bottom gate top contact

2.2.2 Metal – oxide semiconductor capacitor

The metal-oxide semiconductor (MOS) capacitor is an integral component of the TFT as shown in Fig. 2.2, where the gate metal and semiconductor are separated by an insulator. In the following discussion, only an ideal n-type MOS capacitor will be considered. Where it is assumed that charge only exists when a bias is applied, and no transport occurs through the oxide. Below, Fig. 2.3(a) – (d) indicate the four regions of operation for a MOS capacitor; flat band, accumulation, depletion and inversion respectively. E_C is the conduction band, E_f is the Fermi-level, E_i is the intrinsic level and E_V is the valence band.

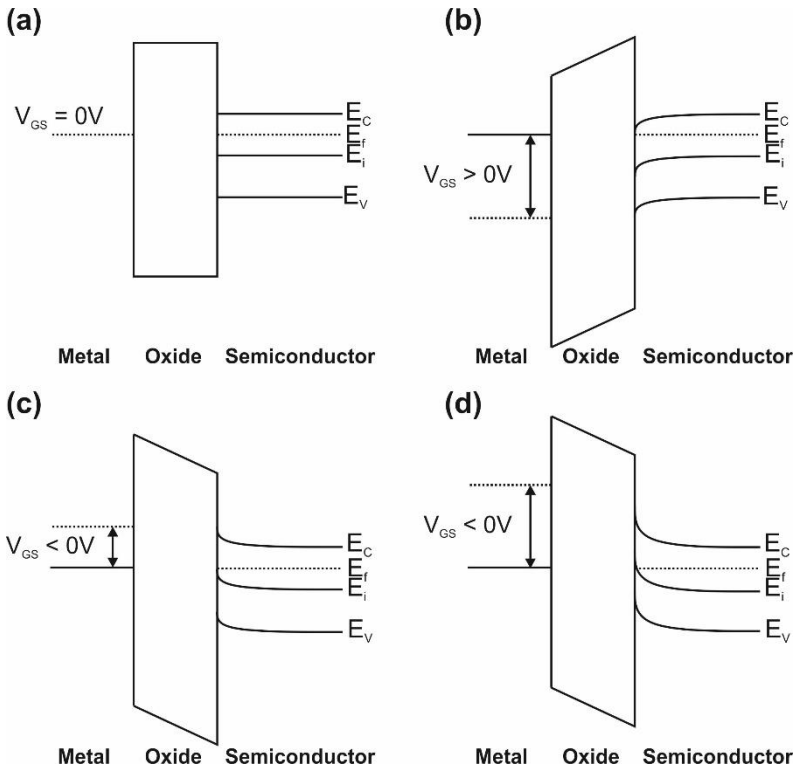

Fig. 2.3 Ideal band diagrams for the TFTs showing (a) flat band condition, (b) forward bias V_{GS} > 0 V, where an accumulation region is formed, (c) reverse bias V_{GS} < 0 V, where a depletion region is formed and (d) inversion.

Fig. 2.3(a) indicates the flat band region, where no bias is applied to the metal. Under this condition the Fermi-levels of the metal and semiconductor are aligned. When a positive bias is applied to the metal contact ($V > 0$), the band bend upwards and is closer to E_f. This causes the electrons (majority) carriers to accumulate at the metal-oxide interface as indicated by Fig. 2.3(b). When a small negative bias is applied (V < 0), the bands bend downwards, and the carriers are depleted away from the interface, as shown in Fig. 2.3(c). The final condition occurs when a large negative bias is applied and the E_i crosses over E_f, resulting in the density of the hole (minority carriers) exceeding that of the electrons (majority carriers). At this point the layer at the surface is inverted with respect to the semiconductor layer and is shown in Fig. 2.3(d). The operating regimes shown in Fig. 2.3(a) – (c) are of particular interest for TFT operation and will be discussed in the following section.

2.2.3 TFT operation

The device structure used is bottom gate top contact shown in Fig. 2.2(d) and the work function of the S/D and the gate are the same. When no bias is applied between the gate and source (V_{GS} = 0 V), the E_f of the gate metal and semiconductor in the electron bands diagram are aligned. This point, shown in Fig. 2.3(a). To turn the TFT on, a forward bias (V_{GS} > 0 V) is applied to the gate contact, resulting in E_C bending towards and E_V away from E_f. This band

bending is shown in Fig. 2.3(b). When the potential between the drain and source contacts (V_{DS}) > 0V, electrons can flow from the ohmic source contact to the drain contact. This occurs along the semiconductor/oxide interface in the accumulation channel.

However, if the applied potential at the gate, $V_{GS} < 0$ V, E_V bends towards E_f and electrons in the semiconductor are depleted away from the oxide-semiconductor interface. By further increasing the potential, the depletion width is increased and the TFT is described to be in an off-state. The effect of applying a negative bias is shown in Fig. 2.3(c).

Thus, the drain current, I_D, is dependent on the flow of electrons between the source and drain contacts, which is controlled by the modulation of the accumulation layer at the semiconductor-insulator interface. This is where the TFT differs from the MOSFET. The channel for a MOSFET is created under the inversion regime. For TFTs, strong inversion is unlikely due to the intrinsic physical properties of the semiconductor. The semiconductor is typically amorphous or small polycrystalline and contains a high concentration of defects with associated energy levels within the band gap. These defect-related levels or traps cause pinning of the Fermi-level and hence inhibit the formation of an inversion layer. An inversion mode device also requires the formation of p-n junctions which would be very challenging in this material as well as adding considerable cost in the fabrication process.

To determine I_D, the threshold voltage (V_T) is required, that is, the minimum gate potential necessary to induce a charge at the insulator-semiconductor interface. The exact definition of V_T for TFTs is subject to debate due to the different nature of channel formation compared to MOSFETs. For MOSFETs, V_T is the voltage required to form an inversion layer. For a TFT, the flat-band condition could be considered analogous to the V_T of a MOSFET. It is sometimes referred to as V_{ON} and is the potential required to form the accumulation layer. Although the formation of the channel is in contrast with a MOSFET, due to the space charge region, a TFT is still considered analogous with a MOSFET.

Moreover, it is widely accepted to apply MOSFET theory to obtain quick analysis and benchmarking across a wide range of technologies. In this thesis, the effective V_T obtained in this manner is adopted for benchmarking purposes. Therefore, the effective V_T gives a useful indication when a substantial current is induced in the channel; an integral parameter for compact models used in circuit design. The flat band voltage (V_{FB}) is also an important figure of merit as this describes the required gate potential to form an accumulation channel. This will be discussed in further detail in chapter 3.

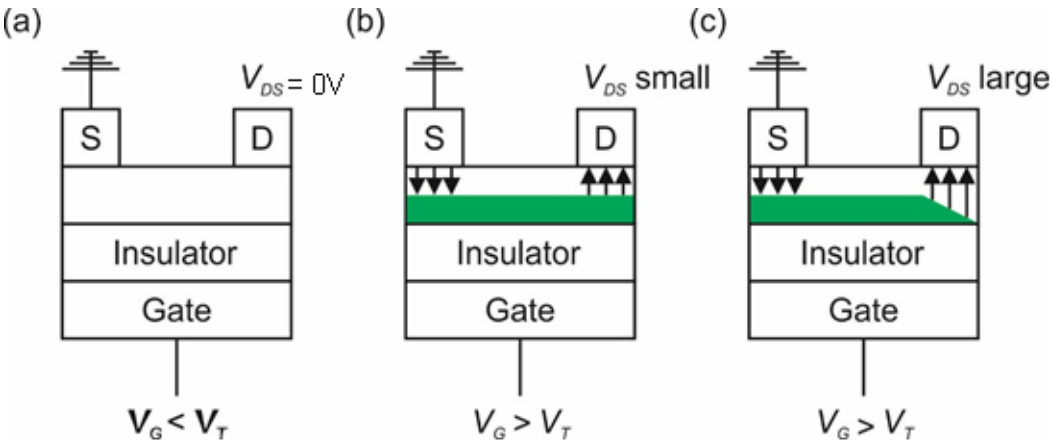

Fig. 2.4 Cross section of bottom gate top contact demonstrating the channel conditions for (a) the off-state, (b) linear-regime and (c) saturation-regime

The operation modes for an n-type TFT are shown in Fig. 2.4(a)-(c), showing the off-state, linear and saturation regimes respectively. Fig. 2.4(a) shows that if V_{GS} is less than the required threshold voltage, no channel is formed at the semiconductor-insulator interface. If $V_{GS} > V_T$ and a small drain potential (V_{DS}) is applied, current will flow between the source and drain, and a channel will be formed, as indicated in Fig. 2.4(b). Under this condition the flow of current is Ohmic with the applied V_{DS} and is often referred to as the linear-regime. As V_{DS} is further increased so that $V_{DS} = V_{GS} - V_T$, pinch-off occurs and is indicated in Fig. 2.4(c). If, V_{DS} is further increased past the pinch-off point, the drain current only exhibits a small, insignificant increase, with respect to V_{DS}. This region is known as saturation. Interestingly, pinch-off for TFTs differs to that seen in MOSFETs, where for large V_{DS} the pinch-off point moves down the channel towards the source.

The effect of pinch-off for $V_{GS} > V_T$ increasing V_{DS} is shown in Fig. 2.5, using Silvaco TCAD simulations. For low $V_{DS,1}$, it is evident that the well-established channel extends under the drain contact, as indicated by the high electron concentration (red region) at the semiconductor-insulator interface. By increasing the drain potential to $V_{DS,2}$, at the onset of pinch-off, the electron concentration is reduced by 2-3 orders of magnitude under the drain contact. At $V_{DS,3}$, pinch-off in the lateral direction has been fully established and does not move past the drain contact region. Electrons are now depleted vertically in the film under the drain contact as indicated by the light blue region. Finally, for the case of $V_{DS,4}$, the TFT is fully pinched-off.

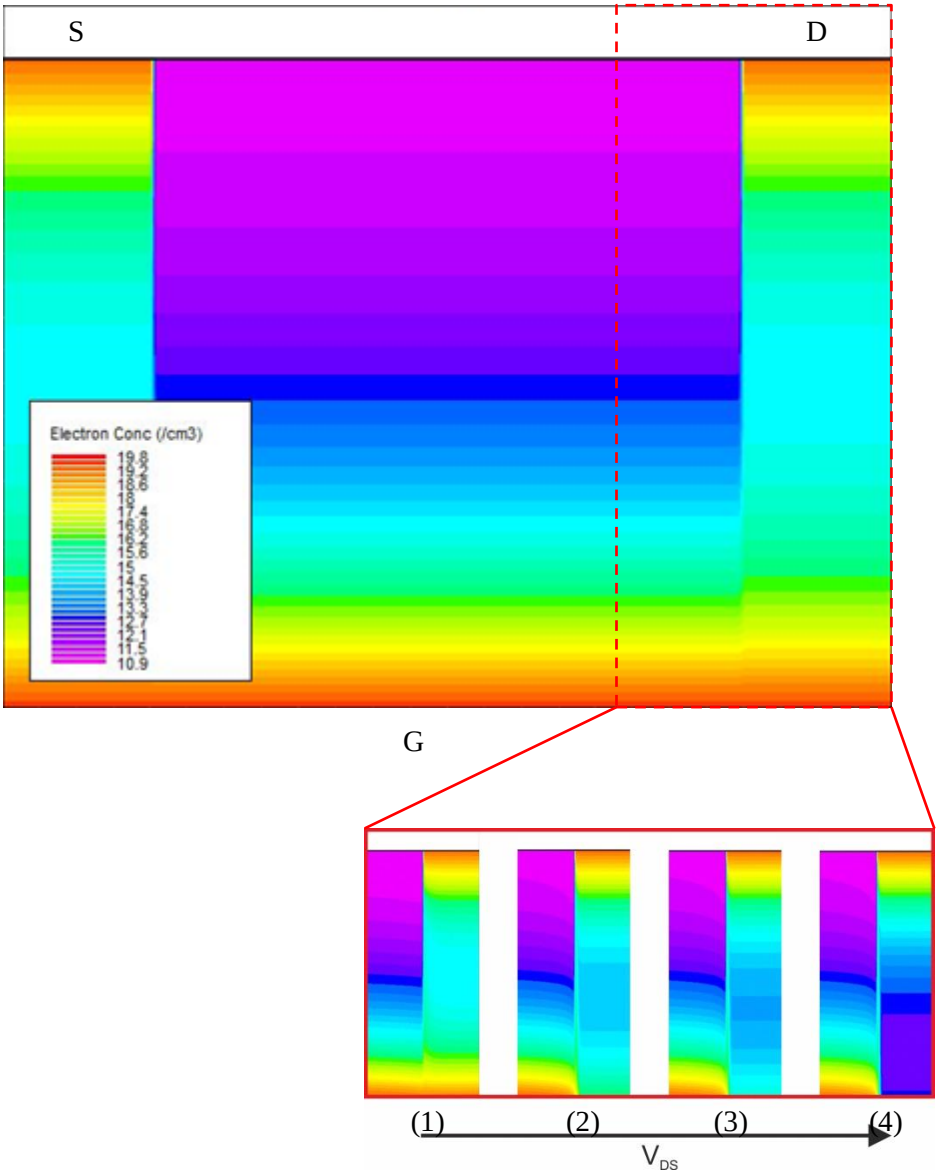

Fig. 2.5 The effect of pinch-off observed in bottom-gate top-contact TFTs for increasing V_{DS} using TCAD. The simulation depicts the electron concentration in the ZnO film, where G represents the oxide-semiconductor interface, S/D indicate the source and drain contact regions.

A simplified model for the drain current behaviour of an ideal TFT is adopted for the purposes of benchmarking using the same principles and assumptions as the ideal MOSFET:

- The gate insulator is ideal with no defects such as interface traps, mobile charge and pin holes
- Doping in the channel is uniform
- Reverse leakage is negligible
- Gradual channel approximation is valid i.e. the vertical field is much greater than the lateral field.
- The drift current dominates the conduction.

Using those assumptions, the drain current is described as

$$I_D = \frac{W}{L} C_i \mu \left[(V_{GS} - V_T) V_{DS} - \frac{{V_{DS}}^2}{2} \right] \rightarrow \text{Linear regime: } V_{DS} < V_{GS} - V_T \quad (2.1a)$$

$$I_D = \frac{W}{2L} C_i \mu (V_{GS} - V_T)^2 \rightarrow \text{Saturation regime: } V_{DS} \geq V_{GS} - V_T \quad (2.1b)$$

where W is the channel width, L is the channel length, C_i is the capacitance of the gate insulator per unit area, V_T is the effective threshold voltage and μ is the effective mobility of electrons in the channel.

2.2.4 Zinc oxide based TFTs

Over recent years Zinc oxide based TFTs using a range of deposition techniques and gate insulators have been reported. As mentioned in section 2.2.3, typically Eqn. (2.1) are employed to benchmark and compare advances in the state of the art. Table 2.1 shows the state of the art performance of ZnO TFTs in relation to material, deposition method, device structure, gate insulator, effective mobility, effective threshold voltage and sub-threshold swing (*SS*). The devices are of bottom-gate top-contact type, the favoured structure due to the ease of fabrication. Furthermore, a range of gate insulators are used with Ta_2O_5, HfO_2 and Al_2O_3 being preferred. It is evident that RF sputtered TFTs present typically larger mobilities than MOCVD, PLD and Sol-gel deposited layers, potentially due to the dominant (002) crystal orientation [19]. Brox-Nilsen *et al.* [20] demonstrated exceptionally high saturation mobilities up to 80 cm^2/Vs with Ta_2O_5 as the gate insulator. The high mobility ZnO for MOCVD TFTs were attributed to excellent crystal orientation between the Al_2O_3 substrate and ZnO [21]. This demonstrates the effect of obtaining single crystal orientation ZnO for high mobilities. The threshold voltage is dependent on the gate metal, oxide and ZnO thin-films. However, it is evident that by using either MgO [22], HfO_2 [23-25] or Ta_2O_5 [20, 26] as the gate oxide, lower V_T is achievable. A broad range of subthreshold swings are obtained for all processing techniques and is highly dependent on the interface properties between the semiconductor and insulator. The best interfaces were obtained by Kuan *et al.* [27], however, the *SS* requires further reduction below 400 mV/dec to rival other deposition techniques for ZnO.

Table 2.1 State of the art ZnO TFTs fabricated using various deposition techniques, acronyms: LIN is for linear, SAT is for saturation and Hall for Hall mobility

	Structure	**Material**	**Deposition Method**	**Gate Insulator**	***On/Off ratio***	***μ* (cm^2/Vs)**	***V_T*** **(V)**	***SS*** **(mV/dec)**	**Post Deposition Treatment**	**Ref**
Brox-Nilsen *et al.*	BG-TC	ZnO	RF sputter	Ta_2O_5	10^5	80 (SAT)	1.1	300	N/a	[20]
Zhu *et al.*	TG-TC	ZnO	MOCVD	SiO_2	10^8	35 (LIN)	-25.4	940	N/a	[21]
Chen *et al.*	BG-TC	ZnO	RF sputter	MgO	$>10^4$	78 (SAT)	0.7	N/a	N/a	[22]
				HfO_2		12 (SAT)	2.5			
Carcia *et al.*	BG-BC	ZnO	RF sputter	$HfSiO_x$	N/a	4.5 (SAT)	1.7	N/a	N/a	[23]
				Al_2O_3		17 (SAT)	6.0			
Sun *et al.*	TG-TC	ZnO	PLD	HfO_2	10^7	4.4 (HALL)	0.5	300	N/a	[24]
Yoshida *et al.*	TG-TC	ZnO	PLD	HfO_2	10^6	21	-2.9	260	N/a	[25]
Zhang *et al.*	BG-TC	ZnO	RF sputter	Ta_2O_3	10^5	46 (SAT)	1	320	N/A	[26]
Kuan *et al.*	BG-TC	ZnO:N	RF sputter	TiN	10^9	71 (LIN)	2.0	180	N_2 atmosphere 1.5 h	[27]
Fortunato *et al.*	BG-TC	ZnO	RF sputter	ATO	10^5	20 (SAT)	21	1240	N/a	[28]
Hirao *et al.*	BG-TC	ZnO	RF sputter	SiO_x/SiN_x	10^8	5.2 (SAT)	N/a	N/a	SiN_x passivation	[29]
Remashan *et al.*	BG-TC	MgZnO/ZnO	MOCVD	Si_3N_4	10^8	9.1 (SAT)	7.1	380	N/a	[30]
Mi *et al.*	BG-TC	ZnO	MOCVD	Al_2O_3	10^6	23 (SAT)	-4.8	800	Si_3N_4 passivation	[31]
You *et al.*	BG-TC	ZnO	Sol-gel	SiO_2	10^7	0.9 (SAT)	12.3	N/a	300°C anneal	[32]

Table 2.2 Summary table benchmarking ALD and PEALD ZnO based TFTs, acronyms: LIN is for linear and SAT is for saturation mobility

	Structure	**Material**	**Deposition Method**	**Gate Insulator**	***On/Off ratio***	***μ*** **(cm^2/Vs)**	***V_T*** **(V)**	***SS*** **(mV/dec)**	**Post Deposition Treatment**	**Ref**
Wang *et al.*	BG-TC	ZnO	ALD (200 °C)	Al_2O_3	10^8	21.3 (SAT)	4.1	244	200 °C anneal in air 1.5 h	[33]
Ma *et al.*	TG-BC	ZnO	ALD (130 °C)	HfO_3	10^8	1.4 (SAT)	0.9	89	N/a	[34]
Lin *et al.*	BG-TC	ZnO	ALD (<110 °C)	Al_2O_3/ HfO_2	10^5	20	2.4	380	Passivation TiO_2 or TAO	[35]
Yan *et al.*	BG-TC	ZnO	ALD (150 °C)	SiO_2 SiO_2/HfO_2 SiO_2/Al_2O_3	10^6 10^5 10^7	0.9 0.4 3.9	N/a	2260 4450 1350	300 °C anneal in O_2, 3 min	[36]
Yumi *et al.*	BG-TC	ZnO	PEALD (100 °C)	SiO_2	10^8	3.2	-1.3	300	300 °C anneal in O_2 1 h	[37]
Oruc *et al.*	BG-TC	ZnO	ALD (130 °C)	Al_2O_3	10^8	15.9	1.58	165	N/a	[38]
Ding *et al.*	BG-TC	ZnO HfZnO	ALD (150 °C)	Al_2O_3	10^6 10^7	11.3 9.4	N/a	400 300	250 °C anneal in air 20 min	[39]
Kawamura *et al.*	BG-TC	ZnO:N	PEALD (100 °C)	SiO_2 Al_2O_3	N/a 10^9	0.3 (SAT) 5.1 (SAT)	N/a	N/a 200	N/a	[40]
Sheng *et al.*	TG-TC	IZO	ALD (200 °C)	Al_2O_3	10^9	42	-0.7	210	200 °C anneal in air 20 min	[41]
Alshammari *et al.*	BG-TC	ZnO	ALD	Al_2O_3/ Ta_2O_5	10^8	13.3 (SAT)	1.1	190	160 °C anneal in air 1h	[42]
Li *et al.*	BG-TC	ZnO	PEALD (200 °C)	Al_2O_3	10^8	12 (LIN)	N/a	300	Al_2O_3 passivation	[43]
Geng *et al.*	TG-BC	ZnO	ALD (200 °C)	Al_2O_3	10^7	21 (LIN)	4.8	390	400 °C anneal in O_2 2 min	[44]

Table 2.2 demonstrates that ALD ZnO TFTs have a broad range of values for mobility, threshold voltage and subthreshold swing. The highest achievable mobility obtained for ALD films are reported by *Sheng et al.* [41], where the indium within the film helped to increase the linear mobility, as observed in IGZO TFT. Furthermore, mobilities > 20 cm^2/Vs were achieved using ZnO on Al_2O_3 *by* Wang *et al*. [33], Lin *et al*. [35] and Geng *et al*. [44]. Wang *et al.* [33] and Geng *et al.* [44] attributed the increased mobility to a reduction of oxygen deficiency within the film with post deposition annealing. Whereas *Lin et al.* [35] achieved similar effects by selecting a passivation layer with low oxygen extraction energies such as TiO_2. For doped and un-doped ZnO films, low subthreshold swings are obtainable with Al_2O_3 as the gate oxide. Another notable technique used for ALD ZnO is the use of post deposition treatments, predominantly annealing. Typically, ALD thin-films are inherently highly conductive and annealing serves to reduce the conductivity by the removal of oxygen vacancies.

2.3. Schottky and Ohmic contacts

The interface between metal-semiconductors are categorised as either Schottky or Ohmic contacts. Schottky contacts have rectifying properties, which produces asymmetric current-voltage characteristics. Conversely an Ohmic contact exhibits linear conduction and is independent of the polarity of the applied potential.

A range of factors affect the classification of the contact, however, in ideal cases it is dependent on the work function of the metal (ϕ_m), semiconductor work function (ϕ_s) and the type of the semiconductor (n-type or p-type). Table 2.3 shows metal-semiconductor contacts for an ideal case. The following discussion will concentrate on n-type semiconductor material; however, the principles for both Schottky and Ohmic contacts remain the same for p-type but are reversed.

Table 2.3 The four possible combinations of metal-semiconductor contacts

	Semiconductor	**Contact**
$\phi_m > \phi_s$	n-type	Schottky
$\phi_m > \phi_s$	p-type	Ohmic
$\phi_m < \phi_s$	n-type	Ohmic
$\phi_m < \phi_s$	p-type	Schottky

2.3.1 Ohmic contacts

Ohmic contacts are formed when a semiconductor and metal are brought into contact, where ϕ_s is greater than ϕ_m. For this condition, linear current behaviour is observed for varying potentials applied to the metal contact. A schematic for the formation of an ohmic contact is shown in Fig. 2.6 demonstrating before and after contact of the metal and semiconductor.

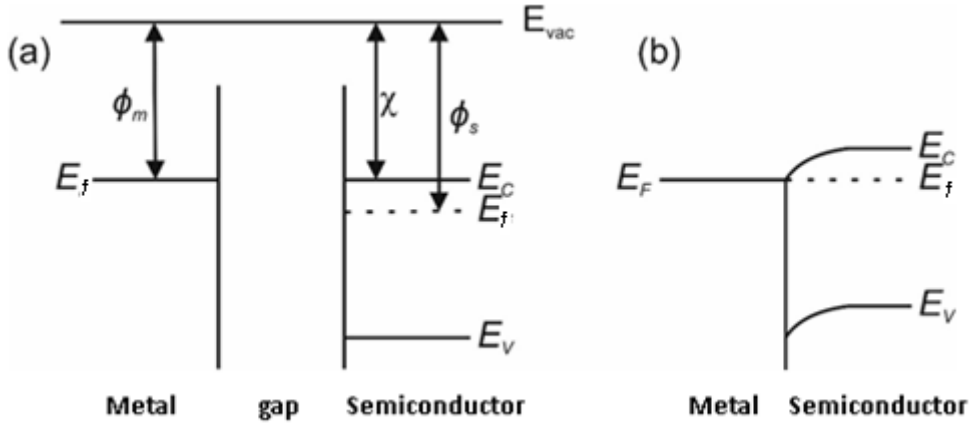

Fig. 2.6 Energy band diagram for the formation of an ohmic contact for metal-semiconductor junctions at (a) before and (b) after contact

Ohmic contacts are characterised by the specific contact resistance (ρ_c), which is defined as the differential between the current and the applied voltage. The equation for the specific contact resistance at zero bias given below

$$\rho_c = \left[\frac{dJ}{dV}\right]^{-1}_{V=0} \tag{2.2}$$

Two mechanisms for conduction in Ohmic contacts are considered; thermionic emission and tunnelling. The former can occur when the barrier is small giving rise to linear behaviour, with the resultant specific resistance proportional to $exp(q\phi_B/kT)$. This condition may be problematic for wide-band gap materials depending on whether the barriers are formed by Fermi-level pinning or work function difference; the ideal case. Tunnelling current can be considered if the doping of the semiconductor is high enough so that the depletion region is small. This will facilitate the possibility of carrier tunnelling through the barrier. Therefore, the specific contact resistance is proportional to the tunnelling process and is defined as:

$$\rho_c \propto \exp\left(\frac{q\phi_B}{E_{00}}\right) \tag{2.3}$$

where E_{00} is a function that can be used to determine the dominant the conduction mechanism in metal-semiconductor contacts and is given by

$$E_{00} = \frac{q\hbar}{2}\sqrt{\frac{N_d}{m^* \varepsilon_s}} \tag{2.4}$$

where $\hbar$ is Planck's constant and m^* is the effective mass of an electron. The tunnelling current is said to be dominant if $kT \ll E_{00}$.

2.3.2 Schottky contacts

For n-type semiconductors, a Schottky contact is formed when a metal with a higher work function, ϕ_m, is deposited onto the semiconductor and is shown in Fig. 2.7(a). As the separation between the two materials is reduced until contact, electrons from the semiconductor will flow into the metal, causing the formation of a depletion region (W_d) [45]; the Fermi levels align to establish thermal equilibrium as shown in Fig. 2.7(b).

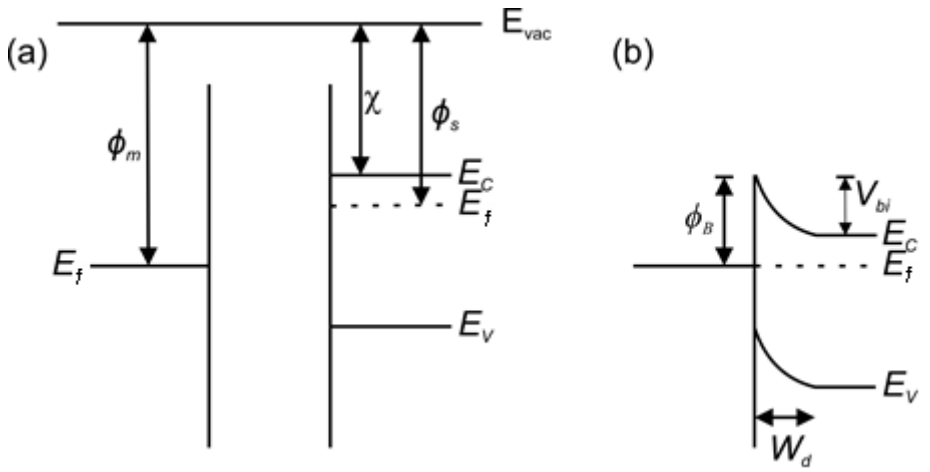

Fig. 2.7 Energy band diagrams for metal-semiconductors (a) before contact and (b) after contact in thermal equilibrium

A potential barrier is formed for both electrons in the metal and semiconductor. The flow of electrons from the semiconductor to metal is controlled by the built-in potential (V_{bi}), whereas, for electrons in the metal, the barrier height (ϕ_B) controls the flow. The ideal barrier height and built-in potentials are defined as:

$$q\phi_B = q\phi_m - q\chi \tag{2.5}$$

$$qV_{bi} = q\phi_m - q\chi - \frac{E_C - E_F}{q} \tag{2.6}$$

where q is the charge of an electron. The band diagrams for forward and reverse bias conditions are shown in Fig. 2.8 in order to understand the current flow. Fig. 2.8(a) demonstrates the forward bias condition when a potential V_F is applied to the Schottky contact. Under this condition the Fermi-level of the metal is lowered with respect to that of the semiconductor and the electron bands are less bent so that ($V_{bi} - V_F$) is reduced. This causes an increase in electron flow from semiconductor to metal. Conversely for reverse bias (V_R) shown in Fig. 2.8(b), the Fermi-level of the metal is increased compared to the semiconductor, resulting in a widening of the depletion region and increase in ($V_{bi} + V_R$). As a consequence, current is limited by the increased barrier resulting in the rectifying properties of a Schottky contact.

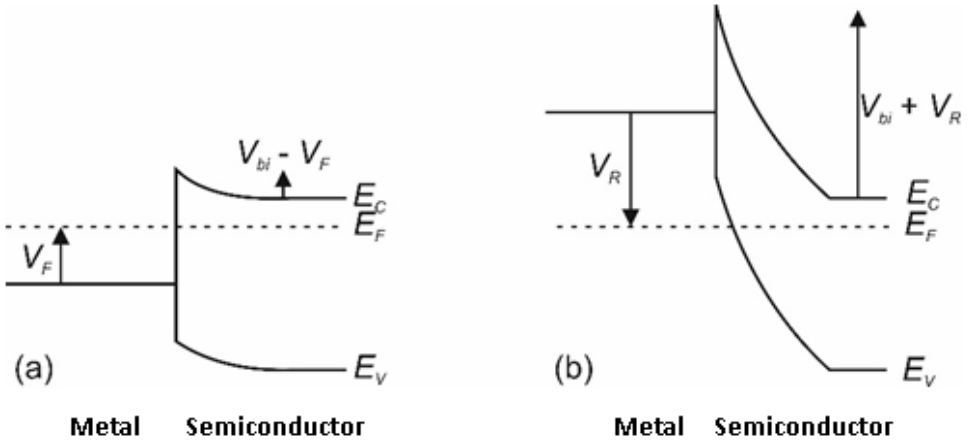

Fig. 2.8 Energy band diagrams for a Schottky contact under (a) forward bias (V_F) and (b) reverse bias (V_R)

The conduction in a Schottky contact due to majority carriers. The main conduction mechanisms considered for Schottky diodes are thermionic emission [46] and diffusion [47], which dominates in low mobility materials. This stipulates that diffusion current accounts for charge transport across the entire depletion region. Whereas, thermionic emission only considers carriers which have energies at least equal to the conduction band at the metal-semiconductor interface [45]. Firstly, thermionic emission will be considered, where the current density (J) is described as

$$J = A^* T^2 \exp\left(\frac{-q\phi_B}{kT}\right)\left[\exp\left(\frac{qV_a}{\eta kT}\right) - 1\right] \tag{2.7}$$

where A^* is the Richardson constant for thermionic emission, V_a is the applied potential at the Schottky contact and η is the ideality factor. The Richardson constant quantifies the emission

of carriers with respect to temperature. It is dependent on the effective mass of material, where in this case is the semiconductor. The ideality factor accounts for non-ideal behaviour in the diode including tunnelling. The following properties have a detrimental effect on the ideality factor; dipoles at the surface, unintentional oxide and lateral inhomogeneity along the surface. Surface inhomogeneity is of particular interest in our case and is likely to arise from the presence of grain boundaries intersecting with the surface. This will be discussed in chapter 6. Typically for a Schottky diode, a value of η between 1 – 1.1 can be taken as an indication that thermionic emission is the dominant conduction mechanism and is given as:

$$J = J_{SD}\left[\exp\left(\frac{qV_a}{\eta kT}\right)-1\right] \tag{2.8}$$

where J_{SD} is the saturation diffusion current given as:

$$J_{SD} = \frac{q^2 D_n N_C}{V_{th}}\sqrt{\frac{2q(V_{bi}-V_a)N_d}{\varepsilon_0\varepsilon_s}}\exp\left(\frac{q\varphi_B}{kT}\right) \tag{2.9}$$

where D_n is the diffusion constant for carriers, N_C is the effective density of states in the conduction band, V_{th} is the thermal voltage (kT/q), N_d is the free donor concentration, ε_0 is the permittivity of free space and ε_s is the permittivity of the semiconductor. In many aspects thermionic emission and diffusion current reduce to the same equation, with different limiting saturation currents. Crowell and Sze determined that a combination of current mechanisms can contribute to emission over the barrier [48]. It is stated that thermionic emission dominates, if the recombination velocity is limited, i.e. under a large electric field.

The reverse bias characteristics for ideal Schottky contacts, is expected to be limited by the barrier, hence $A^*T^2\exp(-q\phi_B/kT)$. Taking account of the effect of the image force, leads to a dependence on the electric field, serving to reduce the barrier height. The reverse current follows a $\ln(J)$ - $V^{1/4}$, dependence and the doping density can be obtained from a straight-line plot [45].

The Schottky barrier is also influenced by so-called surface states which originate from defects on the semiconductor surface such as dangling bonds, contamination and dipoles arising from metal induced gap states (MIGS). MIGS are formed due to mismatching of Fermi-levels, between the deposited metal and semiconductor. The surface states are present at energies within the conduction band and are shown in Fig. 2.8. They are accounted for in the charge neutral level model [45]. It is assumed that the band structure at the surface is the same as that in the bulk and that the distribution of surface states is linear. It should be noted however that

many systems have large localised peaks of interface states which dominate the Fermi-level pinning. A neutral potential (ϕ_0) is introduced to define the classification of the states. At absolute zero degrees, the states are filled from the lowest energy up to the Fermi-level. Occupied states below ϕ_0 are donor- like (positive when empty and neutral when occupied by an electron). Conversely occupied states above the neutral level are acceptor-like (negatively charged when full and neutral when empty of an electron). When a metal-semiconductor interface is formed, the Fermi-level is pinned at the neutral level, which defines the barrier height as shown below:

$$\phi_B = E_g - \phi_0 \tag{2.10}$$

where E_g is the band gap of the semiconductor. For Fermi-level pinning, the barrier height is independent of the metal work function [45].

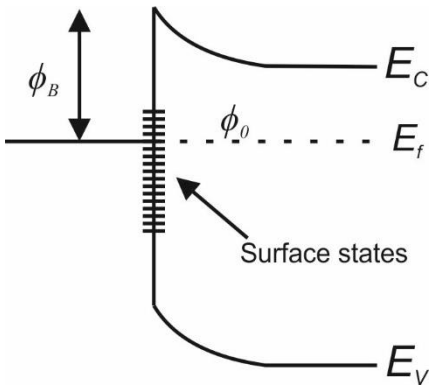

Fig. 2.9 Energy band diagram demonstrating the effect of surface states present at the metal-semiconductor interface

2.3.3 Zinc oxide based Schottky diodes

The formation of good ZnO Schottky diodes remains a challenge with a wide range of achievable characteristics dependent on the ZnO material, surface treatment and Schottky contact. Table 2.4 summaries the state of the art diode characteristics, comparing the key parameters.

As indicated in Table 2.4 bulk ZnO is the preferred growth method for ZnO based Schottky diodes, with O-polar cut material providing the best parameters. A range of barrier heights have been reported for Pd and Ag contacts and it is apparent, that the obtained barrier height is highly dependent on the nature of the surface Allen *et al.* [49] determined that to achieve high barrier heights and low ideality factors, surface treatment of the ZnO and the use of lightly oxidised metal are mandatory for good Schottky characteristics. It has been found that the presence of oxygen vacancies at the ZnO surface result in Fermi-level pinning. Good Schottky contacts can be realised by either treating the surface with an O_2 plasma or using a metal-oxide

such as AgO_x, Similarly Mayes *et al.* [50] achieved the same effect using IrO_x to achieve an ideality factor of 1.05. Currently, few reports for high performance Schottky diodes on ALD ZnO have been published. Table 2.4 list the results of two studies where good barriers are obtained of 0.7 [51] and 0.55 eV [52] for Ag and Cu respectively. However, ideality factors remain above 2.5, indicating that thermionic emission may not be the dominant conduction mechanism for these ALD based Schottky diodes. Although it is worth noting that large ideality factors can be explained by inhomogeneity of barrier height at the junction due to the granular nature of the film [53, 54].

Table 2.4 State of the art ZnO Schottky diodes with various contacts and deposition techniques. The method of extraction for the barrier height is given from either *I-V* or *C-V* measurements. Abbreviations: *RR* (rectification ratio), S.C. (solvent clean)

	Deposition Technique	**Surface Treatment**	**Schottky Contact**	ϕ_b **(eV)**	η	***RR***	**Ref**
Allen *et al.*	Bulk	O_2 plasma	Au	0.69 (*I-V*)	1.10	10^6	**[49]**
		S.C	Pd	0.59 (*I-V*)	1.20	10^4	
		H_2O_2	Pt	0.68 (*I-V*)	1.20	10^6	
Mayes *et al.*	Bulk	S.C	IrO_x	0.85 (*I-V*)	1.05	10^7	**[50]**
Krajewski *et al.*	ALD	N_2 anneal, HfO_2 capping layer	Ag	0.70 (*I-V*)	2.65	10^7	**[51]**
Shen *et al.*	PEALD	O_2 plasma on Cu	Cu	0.55 (*I-V*)	2.70	75	**[52]**
Wenckstern *et al.*	PLD	As-received	Pd	0.81 (*I-V*)	1.49	10^7	**[54]**
Polyakov *et al.*	Bulk	HCl	Au	0.65 (*I-V*)	1.60	10^5	**[55]**
		HCl	Ag	0.70 (*I-V*)		10^4	
Coppa *et al.*	Bulk (0001)	O_2 plasma	Au	0.67 (*I-V*)	1.86	10^4	**[56]**
		O_2 plasma	Au	0.60 (*I-V*)	1.03	10^8	
Kim *et al.*	Bulk (0001)	As-received	Ag	0.89 (*I-V*)	1.31	10^8	**[57]**
		O_2 plasma	Ag	0.85 (*I-V*)	1.45	10^3	
Schifano *et al.*	Bulk (0001)	S.C. and H_2O_2	Pd	1.00 (*C-V*)	1.80	10^9	**[58]**
Mtangi *et al.*	Bulk	S.C and H_2O_2	Pd	0.64 (*I-V*)	1.76	10^8	**[59]**
Grossner *et al.*	Bulk	S.C.	Pd	0.75 (*I-V*)	1.40	10^4	**[60]**
Frenzel *et al.*	PLD	As-received	Ag	0.95 (*I-V*)	1.70	10^8	**[61]**
			Au	0.69 (*I-V*)	2.37	10^3	
			Pd	0.79 (*I-V*)	1.53	10^5	
			Pt	0.90 (*I-V*)	2.04	10^6	
Somvanshi *et al.*	Evaporation	Annealed in N_2	Pd	0.89 (*C-V*)	1.48	10^3	**[62]**
Ali *et al.*	Evaporation	Air annealed	Pd	1.20 (*I-V*)	1.12	10^5	**[63]**
Weichsel *et al.*	MOCVD	S.C.	Pd	0.83 (*I-V*)	1.60	10^8	**[64]**
Sheng *et al.*	MOCVD	-	Ag	0.89 (*I-V*)	1.33	-	**[65]**

2.4. Conclusions

Through background reading, it has been highlighted that for ZnO TFT and Schottky diode applications, ALD is a promising deposition technique. However, it requires considerable research to reduce the native conductivity of the films. Two approaches of interest will be studied in this thesis; substitutional doping with metal and plasma enhanced ALD. Both these techniques aim to reduce the native defects within the ZnO crystal.

2.5. References

[1] Ü. Özgür, Y. I. Alivov, C. Liu, A. Teke, M. A. Reshchikov, S. Doğan, V. Avrutin, S.-J. Cho, and H. Morkoç, "A comprehensive review of ZnO materials and devices," *Journal of Applied Physics,* vol. 98, no. 4, p. 041301, 2005.

[2] A. Janotti and C. G. Van De Walle, "Fundamentals of zinc oxide as a semiconductor," *Reports on Progress in Physics,* vol. 72, no. 12, p. 126501, 2009.

[3] J. S. Park, "The annealing effect on properties of ZnO thin film transistors with Ti/Pt source-drain contact," *Journal of Electroceramics,* vol. 25, no. 2, pp. 145-149, 2010.

[4] S. J. Lim, S. Kwon, and H. Kim, "ZnO thin films prepared by atomic layer deposition and rf sputtering as an active layer for thin film transistor," *Thin Solid Films,* vol. 516, no. 7, pp. 1523-1528, 2008.

[5] E. Guziewicz, M. Godlewski, L. Wachnicki, T. A. Krajewski, G. Luka, S. Gieraltowska, R. Jakiela, A. Stonert, W. Lisowski, M. Krawczyk, J. W. Sobczak, and A. Jablonski, "ALD grown zinc oxide with controllable electrical properties," *Semiconductor Science and Technology,* vol. 27, no. 7, p. 074011, 2012.

[6] Y. Liu, Y. Li, and H. Zeng, "ZnO-Based Transparent Conductive Thin Films: Doping, Performance, and Processing," *Journal of Nanomaterials,* vol. 2013, p. 9, 2013.

[7] E. Fortunato, P. Barquinha, and R. Martins, "Oxide Semiconductor Thin-Film Transistors: A Review of Recent Advances," *Advanced Materials,* vol. 24, no. 22, pp. 2945-2986, 2012.

[8] C. H. Park, S. B. Zhang, and S. H. Wei, "Origin of p-type doping difficulty in ZnO: The impurity perspective," (in English), *PHYSICAL REVIEW -SERIES B,* vol. 66, p. 073202, 2002.

[9] R. Ding, H. Zhu, and Q. Zeng, "Fabrication of p-type ZnO thin films via magnetron sputtering and phosphorus diffusion," *Vacuum,* vol. 82, no. 5, pp. 510-513, 2008.

[10] L. Cao, J. Jiang, and L. Zhu, "Realization of band-gap engineering of ZnO thin films via Ca alloying," *Materials Letters,* vol. 100, pp. 201-203, 2013.

[11] D. C. Look, "Recent advances in ZnO materials and devices," *Materials Science and Engineering B: Solid-State Materials for Advanced Technology,* vol. 80, no. 1-3, pp. 383-387, 2001.

[12] C. G. Van de Walle, "Hydrogen as a Cause of Doping in Zinc Oxide," *Physical Review Letters,* vol. 85, no. 5, pp. 1012-1015, 2000.

[13] K. Black, A. C. Jones, P. R. Chalker, J. M. Gaskell, R. T. Murray, T. B. Joyce, and S. A. Rushworth, "MOCVD of ZnO thin films for potential use as compliant layers for GaN on Si," *Journal of Crystal Growth,* vol. 310, no. 5, pp. 1010-1014, 2008.

[14] P. Fons, K. Iwata, S. Niki, A. Yamada, and K. Matsubara, "Growth of high-quality epitaxial ZnO films on α-Al_2O_3," *Journal of Crystal Growth,* vol. 201–202, pp. 627-632, 1999.

[15] R. D. Vispute, V. Talyansky, S. Choopun, R. P. Sharma, T. Venkatesan, M. He, X. Tang, J. B. Halpern, M. G. Spencer, Y. X. Li, L. G. Salamanca-Riba, A. A. Iliadis, and K. A. Jones, "Heteroepitaxy of ZnO on GaN and its implications for fabrication of hybrid optoelectronic devices," *Applied Physics Letters,* vol. 73, no. 3, pp. 348-350, 1998.

[16] E. M. C. Fortunato, P. M. C. Barquinha, A. C. M. B. G. Pimentel, A. M. F. Gonçalves, A. J. S. Marques, R. F. P. Martins, and L. M. N. Pereira, "Wide-bandgap high-mobility ZnO thin-film transistors produced at room temperature," *Applied Physics Letters,* vol. 85, no. 13, pp. 2541-2543, 2004.

[17] S. C. Gong, S. Bang, H. Jeon, H.-H. Park, Y. C. Chang, and H. J. Chang, "Effects of atomic layer deposition temperatures on structural and electrical properties of ZnO films and its thin film transistors," *Metals and Materials International,* vol. 16, no. 6, pp. 953-958, 2010.

[18] H. Makino, A. Miyake, T. Yamada, N. Yamamoto, and T. Yamamoto, "Influence of substrate temperature and Zn-precursors on atomic layer deposition of polycrystalline ZnO films on glass," *Thin Solid Films,* vol. 517, no. 10, pp. 3138-3142, 2009.

[19] D. Han, Y. Wang, S. Zhang, L. Sun, R. Han, S. Matsumoto, and Y. Ino, "Influence of sputtering power on properties of ZnO thin films fabricated by RF sputtering in room temperature," *Science China Information Sciences,* vol. 55, no. 4, pp. 951-955, 2012.

[20] C. Brox-Nilsen, J. Jin, Y. Luo, P. Bao, and A. M. Song, "Sputtered ZnO Thin-Film Transistors With Carrier Mobility Over 50 cm^2/Vs," *IEEE Transactions on Electron Devices,* vol. 60, no. 10, pp. 3424-3429, 2013.

[21] J. Zhu, H. Chen, G. Saraf, Z. Duan, Y. Lu, and S. T. Hsu, "ZnO TFT Devices Built on Glass Substrates," *Journal of Electronic Materials,* vol. 37, no. 9, pp. 1237-1240, 2008.

[22] W. Y. Chen, J. S. Jeng, and J. S. Chen, "Improvement of Mobility in ZnO Thin Film Transistor with an Oxygen Enriched MgO Gate Dielectric," *ECS Solid State Letters,* vol. 1, no. 5, pp. N17-N19, 2012.

[23] P. F. Carcia, R. S. McLean, and M. H. Reilly, "High-performance ZnO thin-film transistors on gate dielectrics grown by atomic layer deposition," *Applied Physics Letters,* vol. 88, no. 12, p. 123509, 2006.

[24] Y. Sun, K. Ashida, S. Sasaki, M. Koyama, T. Maemoto, S. Sasa, S. Kasai, I. Iñiguez-de-la-Torre, and T. González, "Fabrication and Characterization of Fully Transparent ZnO Thin-Film Transistors and Self-Switching Nano-Diodes," *Journal of Physics: Conference Series,* vol. 647, no. 1, p. 012068, 2015.

[25] T. Yoshida, T. Tachibana, T. Maemoto, S. Sasa, and M. Inoue, "Pulsed laser deposition of ZnO grown on glass substrates for realizing high-performance thin-film transistors," *Applied Physics A,* vol. 101, no. 4, pp. 685-688, 2010.

[26] L. Zhang, J. Li, X. W. Zhang, D. B. Yu, X. Y. Jiang, and Z. L. Zhang, "Glass-substrate-based high-performance ZnO-TFT by using a Ta_2O_5 insulator modified by thin SiO_2 films," *physica status solidi (a),* vol. 207, no. 8, pp. 1815-1819, 2010.

[27] C. I. Kuan, H. C. Lin, P. W. Li, and T. Y. Huang, "High-Performance Submicrometer ZnON Thin-Film Transistors With Record Field-Effect Mobility," *IEEE Electron Device Letters,* vol. 37, no. 3, pp. 303-305, 2016.

[28] E. M. C. Fortunato, P. M. C. Barquinha, A. C. M. B. G. Pimentel, A. M. F. Gonçalves, A. J. S. Marques, L. M. N. Pereira, and R. F. P. Martins, "Fully Transparent ZnO Thin-Film Transistor Produced at Room Temperature," *Advanced Materials,* vol. 17, no. 5, pp. 590-594, 2005.

[29] T. Hirao, M. Furuta, T. Hiramatsu, T. Matsuda, C. Li, H. Furuta, H. Hokari, M. Yoshida, H. Ishii, and M. Kakegawa, "Bottom-Gate Zinc Oxide Thin-Film Transistors (ZnO TFTs) for AM-LCDs," *IEEE Transactions on Electron Devices,* vol. 55, no. 11, pp. 3136-3142, 2008.

[30] K. Remashan, Y. S. Choi, S. J. Park, and J. H. Jang, "High Performance MOCVD-Grown ZnO Thin-Film Transistor with a Thin MgZnO Layer at Channel/Gate Insulator Interface," *Journal of The Electrochemical Society,* vol. 157, no. 12, pp. H1121-H1126, 2010.

[31] H. Mi, J. H. Seo, C. J. Ku, J. Shi, X. Wang, Y. Lu, and Z. Ma, "Microwave TFTs Made of MOCVD ZnO With ALD Al_2O_3 Gate Dielectric," *IEEE Journal of the Electron Devices Society,* vol. 4, no. 2, pp. 55-59, 2016.

[32] H. C. You and Y. H. Lin, "Investigation of the sol-gel method on the flexible ZnO device," *International Journal of Electrochemical Science,* vol. 7, no. 10, pp. 9085-9094, 2012.

[33] Y. H. Wang, Q. Ma, L. L. Zheng, W. J. Liu, S. J. Ding, H. L. Lu, and D. W. Zhang, "Performance Improvement of Atomic Layer-Deposited ZnO/Al_2O_3 Thin-Film Transistors by Low-Temperature Annealing in Air," *IEEE Transactions on Electron Devices,* vol. 63, no. 5, pp. 1893-1898, 2016.

[34] A. M. Ma, M. Shen, A. Afshar, Y. Y. Tsui, K. C. Cadien, and D. W. Barlage, "Interfacial Contact Effects in Top Gated Zinc Oxide Thin Film Transistors Grown by Atomic Layer Deposition," *IEEE Transactions on Electron Devices,* vol. 63, no. 9, pp. 3540-3546, 2016.

[35] Y. Y. Lin, C. C. Hsu, M. H. Tseng, J. J. Shyue, and F. Y. Tsai, "Stable and High-Performance Flexible ZnO Thin-Film Transistors by Atomic Layer Deposition," *ACS Applied Materials & Interfaces,* vol. 7, no. 40, pp. 22610-22617, 2015.

[36] J. Yang, J. K. Park, S. Kim, W. Choi, S. Lee, and H. Kim, "Atomic-layer-deposited ZnO thin-film transistors with various gate dielectrics," *physica status solidi (a),* vol. 209, no. 10, pp. 2087-2090, 2012.

[37] K. Yumi, H. Nozomu, M. Naomasa, H. Masahiro, and U. Yukiharu, "ZnO Thin Films Fabricated by Plasma-Assisted Atomic Layer Deposition," *Japanese Journal of Applied Physics,* vol. 50, no. 4S, p. 04DF05, 2011.

[38] F. B. Oruc, L. E. Aygun, I. Donmez, N. Biyikli, A. K. Okyay, and H. Y. Yu, "Low temperature atomic layer deposited ZnO photo thin film transistors," *Journal of Vacuum Science & Technology A: Vacuum, Surfaces, and Films,* vol. 33, no. 1, p. 01A105, 2015.

[39] X. Ding, C. Qin, J. Song, J. Zhang, X. Jiang, and Z. Zhang, "The Influence of Hafnium Doping on Density of States in Zinc Oxide Thin-Film Transistors Deposited via Atomic Layer Deposition," *Nanoscale Research Letters,* vol. 12, no. 1, p. 63 2017.

[40] Y. Kawamura, M. Horita, Y. Ishikawa, and Y. Uraoka, "Effects of Gate Insulator on Thin-Film Transistors With ZnO Channel Layer Deposited by Plasma-Assisted Atomic Layer Deposition," *Journal of Display Technology,* vol. 9, no. 9, pp. 694-698, 2013.

[41] J. Sheng, H. J. Lee, S. Oh, and J. S. Park, "Flexible and High-Performance Amorphous Indium Zinc Oxide Thin-Film Transistor Using Low-Temperature Atomic Layer Deposition," *ACS Applied Materials & Interfaces,* vol. 8, no. 49, pp. 33821-33828, 2016.

[42] F. H. Alshammari, P. K. Nayak, Z. Wang, and H. N. Alshareef, "Enhanced ZnO Thin-Film Transistor Performance Using Bilayer Gate Dielectrics," *ACS Applied Materials & Interfaces,* vol. 8, no. 35, pp. 22751-22755, 2016.

[43] H. U. Li and T. N. Jackson, "Oxide Semiconductor Thin Film Transistors on Thin Solution-Cast Flexible Substrates," *IEEE Electron Device Letters,* vol. 36, no. 1, pp. 35-37, 2015.

[44] Y. Geng, W. Yang, H. L. Lu, Y. Zhang, Q. Q. Sun, P. Zhou, P. F. Wang, S. J. Ding, and D. W. Zhang, "Mobility Enhancement and OFF Current Suppression in Atomic-Layer-Deposited ZnO Thin-Film Transistors by Post Annealing in O_2," *IEEE Electron Device Letters,* vol. 35, no. 12, pp. 1266-1268, 2014.

[45] S. M. Sze and K. K. NG, "Metal-Semiconductor Contacts," in *Physics of Semiconductor Devices,* 3rd ed. Hoboken, NJ: John Wiley & Sons, Inc., 2012, pp. 134-196.

[46] H. A. Bethe, "Theory of the Boundary Layer of Crystal Rectifiers," *MIT Radiat. Lab. Rep.,* vol. 43, no. 12, p. 46, 1942.

[47] W. Schottky, "Zur Halbleitertheorie der Sperrschicht- und Spitzengleichrichter," *Zeitschrift für Physik,* vol. 113, no. 5, pp. 367-414, 1939.

[48] C. R. Crowell and S. M. Sze, "Current transport in metal-semiconductor barriers," *Solid-State Electronics,* vol. 9, no. 11, pp. 1035-1048, 1966.

[49] M. W. Allen, M. M. Alkaisi, and S. M. Durbin, "Metal Schottky diodes on Zn-polar and O-polar bulk ZnO," *Applied Physics Letters,* vol. 89, no. 10, p. 103520, 2006.

[50] E. L. H. Mayes, J. G. Partridge, M. R. Field, D. G. McCulloch, S. M. Durbin, H.-S. Kim, and M. W. Allen, "The interface structure of high performance ZnO Schottky diodes," *Physica B: Condensed Matter,* vol. 407, no. 15, pp. 2867-2870, 2012.

[51] T. A. Krajewski, G. Luka, L. Wachnicki, A. J. Zakrzewski, B. S. Witkowski, M. I. Lukasiewicz, P. Kruszewski, E. Lusakowska, R. Jakiela, M. Godlewski, and E. Guziewicz, "Electrical parameters of ZnO films and ZnO-based junctions obtained by atomic layer deposition," *Semiconductor Science and Technology,* vol. 26, no. 8, 2011.

[52] M. Shen, A. Afshar, Y. Y. Tsui, K. C. Cadien, and D. W. Barlage, "Performance of Nanocrystal ZnO Thin-Film Schottky Contacts on Cu by Atomic Layer Deposition," *IEEE Transactions on Nanotechnology,* vol. 16, no. 1, pp. 135-139, 2017.

[53] R. T. Tung, "Electron transport at metal-semiconductor interfaces: General theory," *Physical Review B,* vol. 45, no. 23, pp. 13509-13523, 1992.

[54] H. v. Wenckstern, G. Biehne, R. A. Rahman, H. Hochmuth, M. Lorenz, and M. Grundmann, "Mean barrier height of Pd Schottky contacts on ZnO thin films," *Applied Physics Letters,* vol. 88, no. 9, p. 092102, 2006.

[55] A. Y. Polyakov, N. B. Smirnov, E. A. Kozhukhova, V. I. Vdovin, K. Ip, Y. W. Heo, D. P. Norton, and S. J. Pearton, "Electrical characteristics of Au and Ag Schottky contacts on n-ZnO," *Applied Physics Letters,* vol. 83, no. 8, pp. 1575-1577, 2003.

[56] B. J. Coppa, R. F. Davis, and R. J. Nemanich, "Gold Schottky contacts on oxygen plasma-treated, n-type ZnO(000$\bar{1}$)," *Applied Physics Letters,* vol. 82, no. 3, pp. 400-402, 2003.

[57] H. Kim, H. Kim, and D.-W. Kim, "Effect of oxygen plasma treatment on the electrical properties in Ag/bulk ZnO Schottky diodes," *Vacuum,* vol. 101, pp. 92-97, 2014.

[58] R. Schifano, E. V. Monakhov, U. Grossner, and B. G. Svensson, "Electrical characteristics of palladium Schottky contacts to hydrogen peroxide treated hydrothermally grown ZnO," *Applied Physics Letters*, vol. 91, no. 19, p. 193507, 2007.

[59] W. Mtangi, F. D. Auret, C. Nyamhere, P. J. Janse van Rensburg, and M. D. A. Chawanda, "Analysis of temperature dependent measurements on Pd/ZnO Schottky barrier diodes and the determination of the Richardson constant," *Physica B: Condensed Matter*, vol. 404, no. 8–11, pp. 1092-1096, 2009.

[60] U. Grossner, S. Gabrielsen, T. M. Børseth, J. Grillenberger, A. Y. Kuznetsov, and B. G. Svensson, "Palladium Schottky barrier contacts to hydrothermally grown n-ZnOand shallow electron states," *Applied Physics Letters*, vol. 85, no. 12, pp. 2259-2261, 2004.

[61] H. Frenzel, A. Lajn, H. von Wenckstern, G. Biehne, H. Hochmuth, and M. Grundmann, "ZnO-based metal-semiconductor field-effect transistors with Ag-, Pt-, Pd-, and Au-Schottky gates," *Thin Solid Films*, vol. 518, no. 4, pp. 1119-1123, 2009.

[62] D. Somvanshi and S. Jit, "Mean Barrier Height and Richardson Constant for Pd/ZnO Thin Film-Based Schottky Diodes Grown on n-Si Substrates by Thermal Evaporation Method," *IEEE Electron Device Letters*, vol. 34, no. 10, pp. 1238-1240, 2013.

[63] G. M. Ali, A. D. D. Dwivedi, S. Singh, and P. Chakrabarti, "Interface properties and junction behavior of Pd contact on ZnO thin film grown by vacuum deposition technique," *physica status solidi (c)*, vol. 7, no. 2, pp. 252-255, 2010.

[64] C. Weichsel, O. Pagni, and A. W. R. Leitch, "Electrical and hydrogen sensing characteristics of Pd/ZnO Schottky diodes grown on GaAs," *Semiconductor Science and Technology*, vol. 20, no. 8, p. 840, 2005.

[65] H. Sheng, S. Muthukumar, N. W. Emanetoglu, and Y. Lu, "Schottky diode with Ag on (11$\bar{2}$0) epitaxial ZnO film," *Applied Physics Letters*, vol. 80, no. 12, pp. 2132-2134, 2002.

Chapter 3

3. Experimental and measurement techniques

3.1.Introduction

The experimental and analysis techniques used throughout this thesis from device fabrication to modelling are introduced in this chapter. It is split into three main sections; firstly, the methods of deposition of the thin-films used are discussed in section 3.2; then the characterisation techniques are introduced in sections 3.3 and 3.4 for physical and electrical methods respectively.

3.2. Thin-film deposition techniques

3.2.1 Atomic layer deposition

Atomic layer deposition (ALD) is a chemical gas phase thin-film deposition technique developed in the 1960s and 70s [1, 2]. In contrast to chemical vapour deposition, the precursors for ALD are sequentially supplied to the chamber in pulses and are never present at the same time enabling self-limiting surface reactions [1, 2]. The self-limiting nature of ALD results in the reactions at the surface terminating once all the reactive sites are consumed, hence the film grows on an atomic level. Typically, two precursors are required to deposit a film and the process flow diagram for an ALD reaction is shown in Fig. 3.1. The use of the inert gas purge between each precursor enables the removal of excess un-reacted chemicals to further avoid chamber reactions. To acquire the desired thickness, the number of complete cycles as shown in Fig. 3.1 is varied which in turn produces highly uniform layers.

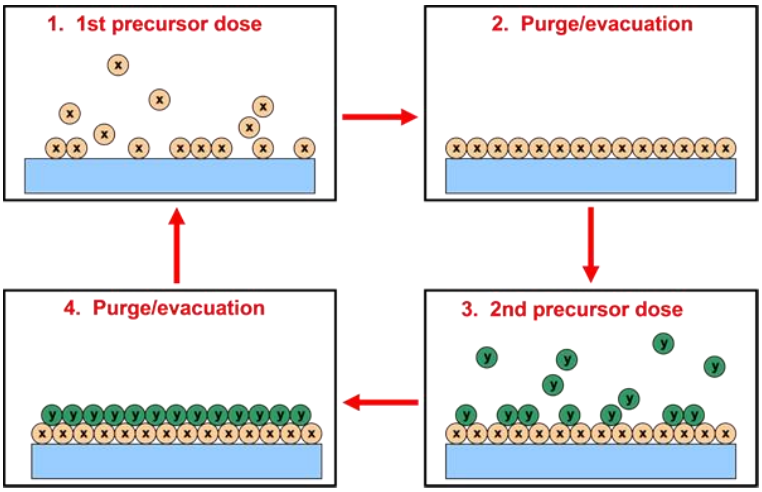

Fig. 3.1 Process flow diagram for a typical ALD reaction [3]

Organic precursors are preferred for the deposition of zinc oxide (ZnO) thin-films due to the lower deposition temperatures and higher growth per cycle rates [4]. Common organic

precursors used for zinc are dimethylzinc (DMZn) or diethylzinc (DEZn) with the oxidising reagent typically deionised water for thermal ALD or oxygen plasma for plasma enhanced (PE-) ALD. The PE-ALD process allows for the deposition temperature to be reduced as the plasma provides an additional source of energy to the process, thus providing an extra degree of control during the deposition process. An important advantage of PE-ALD is that it allows the opportunity of using plastic or glass substrate due to the lower deposition temperature. However, the technique introduces additional complexity to the process chemistry as the optimum plasma conditions need to be determined and optimised including; power, time, flow rate and atmosphere. For both techniques, the Zn and oxidising precursors are supplied to the chamber at room temperature and the substrate temperature varies typically between 80 and 250 ^{o}C. For this work, DEZn is the favoured precursor with the chemical reactions shown below for the ALD and PEALD respectively.

$$Zn(C_2H_5)_2 + H_2O \rightarrow ZnO + 2C_2H_6$$

$$Zn(C_2H_5)_2 + O_3 \rightarrow ZnO + CO_x + H_2O_2$$

The optimum ALD deposition condition is defined by a growth window; a range of substrate temperatures or precursor exposure times, when the growth rate is constant. Typically, the ALD window is given in terms of the substrate temperature. Fig. 3.2 due to Guziewicz *et al*. [4], serves to demonstrate the growth rate against substrate temperature for DEZn and water as the precursors. Although the graph illustrates the growth window for this process between 100 and 170 ^{o}C with a cycle rate of ~ 1.8 Å/s, the window is dependent on all of the processing conditions. Furthermore, the ALD process can be performed outside of the growth window, however, it is convenient to deposit within the temperature limits so that slight fluctuations in temperature have minimal effect on the growth rate and the film can remain uniform.

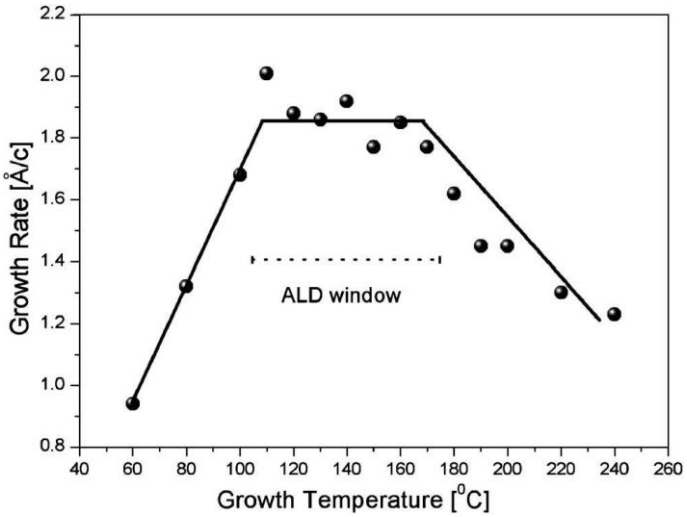

Fig. 3.2 ALD growth rate for DEZn with water against temperature [4]

3.2.2 Radio frequency sputtering

Radio frequency (RF) sputtering is one of the most well-known physical vapour deposition (PVD) techniques and was developed by Davidise and Maiseel in the 1960s [5]. The process of sputtering is achieved by the bombardment of a target material with high energy particles. This results in the atoms on the surface of the target material being dislodged and transported to the substrate. Sputtering is a favourable deposition technique for thin films due to the high controllability of the parameters, such as the thickness and the stoichiometry [6].

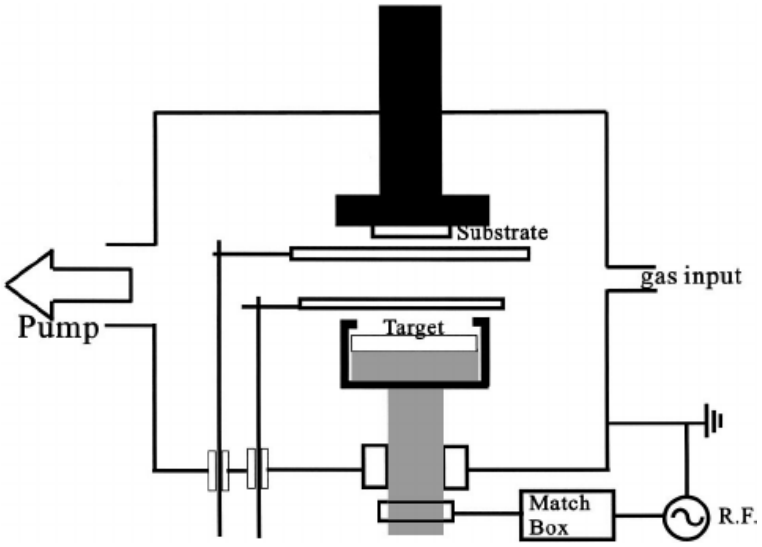

Fig. 3.3 Schematic diagram of an RF sputter system [7]

A typical schematic diagram for an RF sputter is shown in Fig. 3.3. The RF sputter used throughout this thesis has the same configuration as in Fig. 3.3 with a maximum power rating of 150 W. The RF power with a frequency of 13.75 MHz is applied between the magnetron

face (backside of the target) and outer guard ring, whilst in an inert atmosphere, typically argon (Ar). A large electric field is formed between the magnetron face and the guard ring and once the break down voltage is achieved, a glow discharge is created. As a result of interactions between excited electrons the Ar atoms are ionised and, as they relax to their neutral state, photons are emitted hence a glow discharge region is formed. During the negative cycle the target acts as a cathode which attracts the positively charged Ar^+ ions to the surface and bombards the target material. The dislodged atoms travel to the substrate and deposit the desired film. As the target becomes the anode during the positive cycle, charge build-up on the target face is avoided by repelling the accumulated charged Ar^+ atoms and attracting some electrons from the plasma. For the deposition of metals, charge build-up of Ar^+ ions on the target is not an issue due to the conductivity of the target. However, RF is required for insulating layers to overcome the charge build-up.

3.2.3 Thermal evaporation

Thermal evaporation is a PVD technique which involves heating a source material in a high vacuum chamber to the point where the material transforms into the vapour stage. For this work, the heating is achieved using resistive sources known as filaments. As the chamber is under high vacuum $<10^{-6}$ mbar, the mean free path of the vapour is approximately the size of the chamber, or greater. This ensures the material vapour cloud has minimal interaction with ions and follows a straight path to the substrate. Moreover, an added advantage of the use of a high vacuum is that it exploits the relationship between the pressure and vapour transition of the material. As the pressure reduces, so does the vapour temperature of the material, resulting in a lower required current to the thermal source and higher vapour transition materials.

3.3. Thin-film physical characterisation

3.3.1 Spectroscopic ellipsometry

Spectroscopic ellipsometry is an optical film characterisation technique developed in the 1940s by Rothen [8]. Measurements are conducted by transmitting polarised light in two planes *s*- (perpendicular) and *p*- (parallel) to the plane of incidence. The transmitted *s*- and *p*-planes are in phase, creating linearly polarised light. As the light reflects off the samples surface the *s*- and *p*- planes phase and signal intensity change, creating an elliptically polarised light beam. Fig. 3.4 shows a schematic of an ellipsometer system demonstrating the interaction of the polarised light beam from the transmitter and received by the detector, where *E* is the energy of the beam.

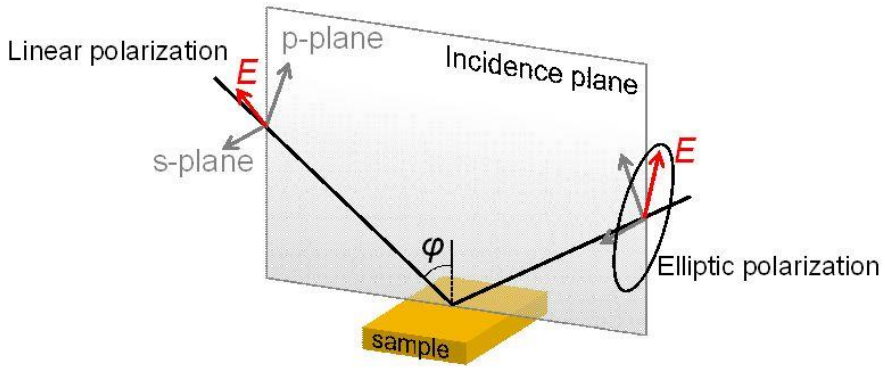

Fig. 3.4 Schematic diagram for a typical ellipsometer demonstrating the change between the transmitted and reflected polarised light [9]

The mathematical background of ellipsometry analysis originates from the Fresnel reflection and transmission equations for polarised light reflected from a single or multi-layered surface [10]. These equations are based on Maxwell's equations [11]. The experimental results obtained are presented in the form of two angles, Ψ and Δ, which are equated using

$$\tan(\Psi)e^{i\Delta} = \frac{r_p}{r_s} \tag{3.1}$$

where r_p and r_s are the Fresnel reflection coefficients associated with the *p*- and *s*- planes of the polarised light beam respectively. Ψ represents the amplitude of the ratio between r_p and r_s, where Δ is the phase quantity. For spectroscopic ellipsometry, Ψ and Δ are obtained for each measured wavelength of polarised light. Ellipsometry is a highly precise measurement technique, as the obtained constants are ratios of the detected light between the *s*- and *p*- planes, which in turn can alleviate some of the inter-measurement noise.

The obtained measurement data, Ψ and Δ, does not inform the user of the films properties such as thickness, refractive index, optical constants and physics properties. Data fitting is required using a combination of oscillators, typically based on Gaussian, Lorentz and Tauc-Lorentz transformations. The oscillators model the losses in the material, that is, the properties of the defects within the matrix. Each oscillator has a characteristic resonant frequency which is related to the position of the defect energy level in the band gap. At certain incident discrete frequencies, the defect levels will 'resonate' indicating absorption in the material. Each oscillator accounts for the peak height and broadening of the spectra (Ψ and Δ) which serves to detect the defect. To acquire the optical properties either represented as a complex dielectric ($\tilde{\varepsilon}$) or complex refractive index ($\tilde{n}$) function, the following equations are used:

$$\tilde{\varepsilon} = \varepsilon_1 + i\varepsilon_2 \tag{3.2}$$

$$\tilde{n} = n + ik \tag{3.3}$$

where ε_1 and ε_2 are the real and imaginary dielectric constants, n is the refractive index and k the extinction coefficient. The relationship between the complex dielectric constant and complex refractive index is $\tilde{\varepsilon} = \tilde{n}^2$.

In this thesis, a predefined oscillator known as Psemi (parameterised semiconductor)-M0 is used for the retrospective fitting of the complex dielectric constant. It is based on the Herzinger-Johs semiconductor oscillator [12, 13]. The oscillator was designed for fitting complex dielectric functions, whilst maintaining Kramers-Kronig (KK) consistency [14]. KK consistency is a method which allows accurate analysis of a complex function by determining the relationship between the real and imaginary regions [15]. Below the functions to determine KK consistency between the real (χ_1) and imaginary (χ_2) functions are given as:

$$\chi_1 = 1 + 2P\int_0^{+\infty} \frac{d\omega'}{\pi} \frac{\chi_2(\omega')}{\omega' - \omega} \tag{3.4}$$

$$\chi_2 = -2P\int_0^{+\infty} \frac{d\omega'}{\pi} \frac{\chi_1(\omega') - 1}{\omega' - \omega} \tag{3.5}$$

where P is the Cauchy principle number, which defines the limits when the function diverges (i.e. $\omega' = \omega$). In ellipsometry, the imaginary part of the optical constant (ε_2) is modelled using oscillators. Subsequently, KK consistency is maintained using the relationship above to calculate the real part of the optical permittivity (ε_1). Although the oscillator is useful for fitting the obtained spectrum and provides good knowledge of the physical parameters, the internal parameters of the oscillators do not have any physical relationships [14]. Moreover, the oscillator, Psemi-M0, is advantageous for the fitting of direct band gap semiconductors, hence the use of this oscillator. Absorption in the material depends on the band gap and also the presence of defects.

By using the oscillators to obtain a model which is representative of the measured data, the optical properties in Eqn. (3.2) and (3.2) are known. Tauc [16] identified a power dependency between the absorption coefficient (α) and photon energy ($h\omega$), where the absorption coefficient is defined as, $\alpha = 4\pi k/\lambda$ where λ is the wavelength and k is the extinction coefficient [17]. The power relationship defined for direct band gap materials was found to be a factor of ½ and 2 for indirect band gap materials. For direct band gap materials, $(\alpha h\omega)^2$ *vs.* $h\omega$ is plotted and the band gap is determined by extrapolating the linear region to the x-axis.

An example of a Tauc plot for a direct band gap film is demonstrated in Fig. 3.5, where the dashed line indicates the absorption edge. Alternatively, for indirect band gaps by plotting $(\alpha h\omega)^{0.5}$ *vs.* $h\omega$ and extrapolating in the same fashion. An example of a Tauc plot for a direct band gap film is demonstrated in Fig. 3.5, where the dashed line indicates the absorption edge. Alternatively, for indirect band gaps by plotting $(\alpha h\omega)^{0.5}$ vs. $h\omega$ and extrapolating in the same fashion.

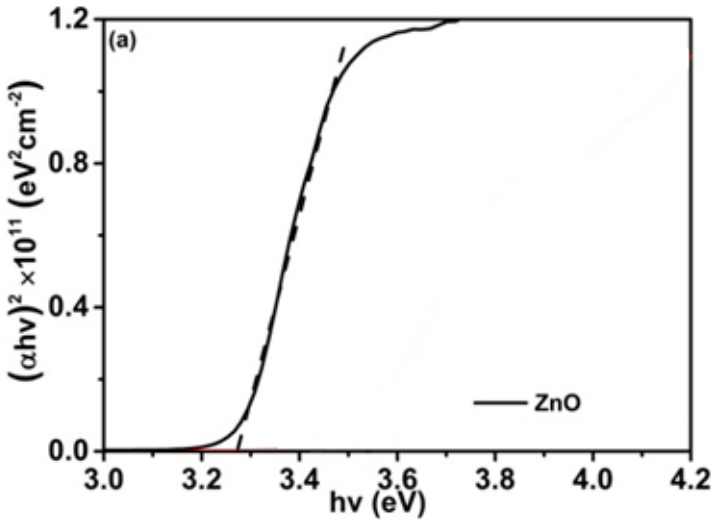

Fig. 3.5 Example Tauc plot for ZnO thin film, with the dotted line highlighting the absorption edge

Ellipsometry measurements performed in this thesis use the J. A. Woollam M2000UI variable angle spectroscopic ellipsometry kit. The light sources are a combination of deuterium and quartz tungsten halogen lamps, enabling a wavelength range of 245-1700 nm. Moreover, by varying the angle around the Brewster angle of the sample, the accuracy of ellipsometry measurements is increased [15]. However, at the Brewster angle the p- plane cannot be reflected but is instead refracted. In this work, three angles are measured to reduce the uncertainty of the measurement.

3.3.2 X-ray photoelectron spectroscopy

X-ray photoelectron spectroscopy (XPS) is a widely used surface analysis technique which was developed by Siegbahn in the 1960s [18]. Surface analysis is conducted in high vacuum, with a monoenergetic X-ray source targeting the sample. As a result of the X-ray interaction with the sample, electrons are emitted by the photoelectric effect. The energy of each electron is analysed to obtain a spectrum of the number of electrons detected against the kinetic energy. XPS allows the user to study electrons which can originate from the core level to valence levels [17, 18] resulting in unique spectra for each detected element. The kinetic energy (*KE*) of the detected electrons is determined by:

$$KE = h\upsilon - BE - \phi_s \tag{3.6}$$

where $h\upsilon$ is the energy of the X-ray source, *BE* is the binding energy of the emitted electron and ϕ_s is the work function of the spectrometer. Commonly two X-ray sources are used with photon energies of 1253.6 eV and 1486.6 eV for the Mg (Mg Kα) and Al (Al Kα) sources respectively. The binding energy is the difference in energy between the initial and final state once the photoelectron has left the atom [17].

In addition to the emission of electrons from the photoelectric effect, Auger electrons may also be emitted and detected. Auger electron emission occurs due to the relaxation of the excited electrons after photoemission. As holes in the inner orbital exist from the photoelectric effect, an electron from a higher orbital will relax into this hole. As a result, another electron from the higher energy orbital or photon with the same energy is emitted in the process. This occurs within approximately 10's of femto-second after the sample emits a photoelectron [17]. Furthermore, the Auger electron energy is equivalent to the energy difference of the initial and double charged final ion. Therefore, photo-ionisation leads to the emission of two electrons, where the energy of the emitted electrons is equal or less than the ionising photons [17].

XPS is a highly surface sensitive measurement technique, due to the probability of the emitted electron interacting with matter. Although the photons have a mean free path of a few microns, the mean free path of an electron is in the order of tens of angstroms. Therefore, if ionisation occurs at a depth of a few micrometres, there is a low probability of electrons being emitted from the sample. Hence only electrons that originate in atoms within a few angstroms are emitted without any energy loss [17]. Electrons that are emitted, which lose energy, form part of the background spectra. The analyser operates in a specified energy window, known as the pass energy, where only electrons within the specified energy will be detected. For measurements, the pass energy is fixed, and the acceptance energy of the analyser is varied over the measurement range.

The measured survey spectrum consists of a number of peak lines with different binding energies. Each detected peak is unique and dependent on the composition of the measured element and the spin orbital the electron is emitted from; s, p, d or f orbitals. For zinc spectra, the following core levels can be detected: 2s, 2p, 3s, 3p and 3d.However, for the identification of zinc, the dominant core level is 2p. In the spectra, the other core levels may be detected but are hard to identify due to the low concentrations of emitted electrons for the core levels. Orbital splitting occurs after the ionisation process where the two binding energy lines are detected with a separation unique to the element. The p, d and f orbitals have the following splits; $p_{1/2}$, $p_{3/2}$, $d_{3/2}$, $d_{5/2}$, $f_{5/2}$ and $f_{7/2}$ [17]. The Zn 2p peak has two spectra lines approximately

at 1021.6 eV and 1044.7 eV for $2p_{3/2}$ and $2p_{1/2}$ respectively [19]. The ratio between the $2p_{3/2}$ and $2p_{1/2}$ peak lines is 2:1. Analysis of the obtained core level spectra is conducted using the CasaXPS software tool. In XPS the unwanted spectra noise caused by inelastic scattering of electrons is removed by the use of an algorithm to fit the background noise. The Shirley type algorithm is widely used to determine the background intensity as a ratio of the number of detected photoelectrons for a given binding energy [20] thus:

$$S_1(E) = \kappa \int_{E}^{E_{end}} \left[I(E') - I_{end} \right] dE \tag{3.7}$$

$$S_n(E) = \kappa \int_{E}^{E_{end}} \left[I_n(E') - I_{end} - S_{n-1}(E') \right] dE' \tag{3.8}$$

where $S(E)$ is the background, $I(E)$ and I_{end} are the measured intensity between the background at a given energy and the last energy to which the Shirley type background is applied. The final term κ is calculated from the convergence of $S_n(E)$ and $S_{n-1}(E)$, providing a self-consistent method for calculating the background intensity [21]. Once the background is accounted for, the core level peaks are fitted using a combination of Gaussian-Lorentz oscillators; so, called Voigt functions.

3.3.3Inverse photoelectron spectroscopy

Inverse photoelectron spectroscopy (IPES) is a similar surface characterisation technique to XPS, but the unoccupied states in the conduction band are analysed. A sample is exposed to a high energy electron beam and the electrons combine with the unoccupied states. As the electrons decay photons are emitted, these photons are subsequently detected to form a spectrum. The obtained spectrum gives details on the position of the conduction band edge relative to the Fermi level of the sample.

3.3.4 X-ray diffraction

X-ray diffraction (XRD) is a measurement technique mainly used to probe crystal structure of a material and is based on the constructive interference of X-rays on a sample [22]. An X-ray beam is irradiated from the source and interacts with the sample material; constructive interference is produced when the conditions satisfy Bragg's law.

$$n\lambda = 2d \sin(\theta) \tag{3.9}$$

where λ is the wavelength, n is the number of wavelengths, d is the atomic spacing and θ is the angle of the X-ray beam diffraction. A schematic of XRD interactions is shown in

Fig. 3.6. The orientation of the crystals within the sample are examined by varying the angle at which the X-rays interact with the sample and satisfy Bragg's law.

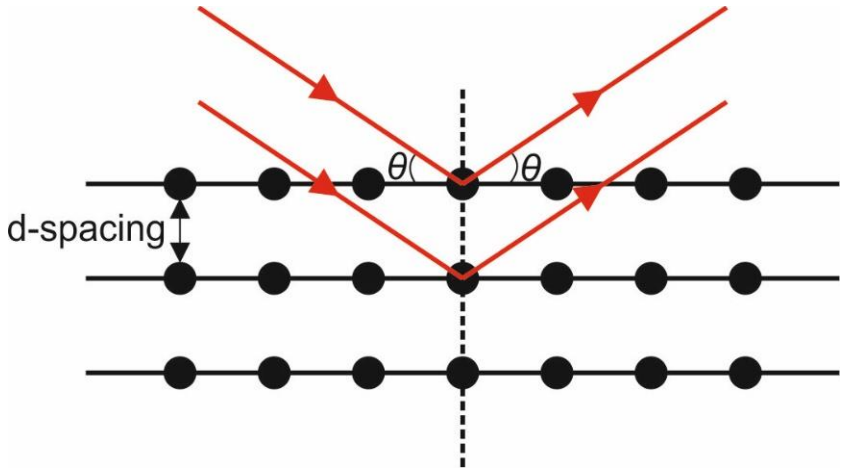

Fig. 3.6 Schematic of X-ray interaction observed in XRD measurements

The spectrum obtained by XRD is given as the intensity of electrons detected against the angle of diffraction, 2θ relative to the incidence angle. Typically, measurements are conducted between the 2θ angles 5 to 70°. An advantage of XRD is that each material is characterised by a uniquely obtained spectra, hence the identification of the sample composition can be determined. The observation of the lack of a crystal structure is indicative of an amorphous material as no XRD peaks are observed [22].

Apart from the crystal orientation, the average grain size for each orientation can be estimated by calculating the full-width half maximum (FWHM) of each XRD peak. The grain size is determined by using the Scherrer equation [23]:

$$\tau = \frac{K\lambda}{B\cos\theta} \tag{3.10}$$

where τ is the grain size, K is the shape factor, λ the wavelength, B the peak broadening (FWHM) and θ the Bragg angle.

3.3.5 Photoluminescence

Photoluminescence (PL) is a non-destructive method for probing the electronic structure of a sample. The band gap and defect energy levels can be probed with PL. Light is directed onto the sample and the process of absorption into the material results in an excess of energy being released as a photon [24]. This phenomenon is known as photo-excitation. As the light is absorbed, electrons are excited from equilibrium to an excited state. When the electron relaxes to its equilibrium state the excess energy between the two states is emitted as a photon.

The obtained spectrum is given as the number of emitted photons against wavelength and the band gap can be determined from the maximum intensity peak. Moreover, defects in the film can be detected, from smaller peaks. For ZnO, green emission peaks (500 – 550 nm) are attributed to oxygen vacancies in the film [25].

3.4. Electrical Characterisation

3.4.1 Current-voltage characteristics

Current-voltage (*I-V*) measurements were performed using an Agilent B1500 semiconductor parameter analyser. Continuous voltage sweeps were applied to the electrodes from reverse to forward and to reverse bias, in order to check for any hysteresis in the characteristics.

3.4.1.1. Thin-film transistor benchmarking

Parameter extraction is implemented using the standard MOSFET equations in order to compare the characteristics and performance of thin-film transistors (TFTs) with the literature. Using this method, the TFT parameters extracted are the *On/Off* ratio, effective threshold voltage (V_T), saturation mobility (μ_{sat}) and the effective subthreshold swing (*SS*). The parameter extraction is conducted on the transfer characteristics for large drain voltage (V_{DS}), with Fig. 3.7 showing typical characteristics.

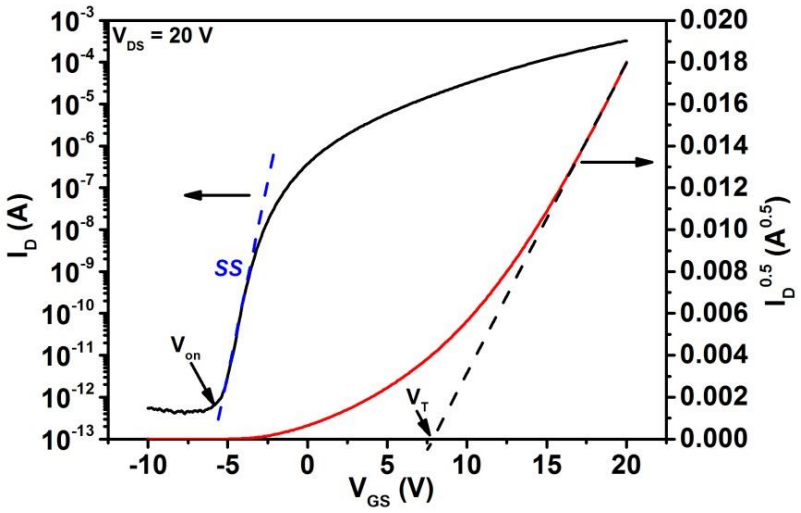

Fig. 3.7 Typical transfer characteristics for ZnO TFT highlighting the parameter extraction techniques

The *On/Off* ratio is defined as the difference between the drain current (I_D) when the channel begins to form as indicated in Fig. 3.7 with V_{on} and the maximum I_D. The on-voltage (V_{on}), is the V_{GS} at which a sharp increase in current occurs [26]. Extracting V_T and μ_{sat} is conducted when the TFT is in saturation regime, i.e. $V_{DS} \geq V_{GS} - V_T$, where V_{GS} is the gate voltage. In this region, the drain current is defined as:

$$I_D = \frac{W}{2L} C_i \mu_{sat} (V_{GS} - V_T)^2 \tag{3.11}$$

where W and L are the channel width and length respectively and C_i is the gate insulator capacitance per unit area. Plotting $\sqrt{I_D}$ against V_{GS} and extrapolating the linear region to the x-axis, gives V_T from the intercept. The gradient yields μ_{sat} as:

$$\mu_{sat} = \frac{2L(gradient)^2}{WC_i} \tag{3.12}$$

The *SS* can be extracted from the log-linear plot of the transfer characteristics by considering the inverse of maximum slope and given as:

$$SS = \left[\frac{\partial \log(I_D)}{\partial V_{GS}} \right]^{-1} \tag{3.13}$$

For an ideal MOSFET, the *SS* is 60 mV/dec at room temperature. This originates from the exponential relationship in I_D when $V_{GS} < V_T$ [$I_D \propto \exp(qV_{GS}/nkT)$], where q is the charge of an electron, k is Boltzmann's constant, T is the temperature and n accounts for any non-ideal behaviour. Therefore, by assuming n = 1 and using the relationship above, an increase in I_D by a factor of 10, yields $V_{GS} = \ln(10)kT/q \approx 60$ mV/dec. However, for the TFTs presented in this thesis it is evident that the sub-threshold behaviour is not ideal. By using the parameter extraction techniques discussed for the device shown in Fig. 3.7, it is evident that the TFT has an *On/Off* ratio > 10^8, V_T = 8.3 V, μ_{sat} = 7.1 cm^2/Vs and the *SS* = 540 mV/dec.

3.4.1.2. Physics based modelling of thin-film transistors

It is evident that the transfer characteristics in Fig. 3.7, does not strictly follow a square power dependency but rather a power law. Due to this dependency, physics-based models are adopted to obtain a deeper understanding of the TFT operation and the material properties. Several models have been proposed for ZnO based materials, focusing on the effects of the density of states (DOS) for large and small grain films [27, 28]. The model of Hossain *et al.* [27] was developed for polycrystalline ZnO with a large grain size (0.2 – 2 µm). In this model, it was assumed that the DOS originate only at the grain boundary interface. Therefore, no defects are within the ZnO grains. The power dependency of the model is therefore defined by the number of grain boundaries. A larger number of grain boundaries in the channel increases the power dependency of I_D. In comparison, the model proposed by Torricelli *et al.* [28] was developed

for ZnO with small grain sizes (~ 20 nm) typical of material grown by ALD. The analytical expression for drain current involves a direct relationship between the distribution of the DOS and the power dependency. This relationship is similar to other models developed for a-Si:H [29-31] and a-IGZO [32], although the ZnO film used in Torricelli's work is not amorphous.

The model of Torricelli *et al.* [28] is adopted for the analysis of TFT characteristics in this thesis, with the aim of understanding the underlying transport mechanism within the ZnO based films. The physics underlying the model is now discussed.

Fig. 3.8 shows a schematic of the MTR (multi-trapping-and-release) model demonstrating the movement of charge. The model assumes a large density of tail states just below the conduction band which are occupied with charge carriers. Charge carriers hop between the states by an MTR transport process. Carriers trapped in the sub-band gap states are thermally excited from occupied states and hop upwards in energy towards the conduction band where the charge carrier is instantaneously trapped in the nearest unoccupied state. This process is repeated until the charge reaches the conduction band and can be considered as free carriers. The MTR model has been used to describe the transport in other DOS based systems [29-32].

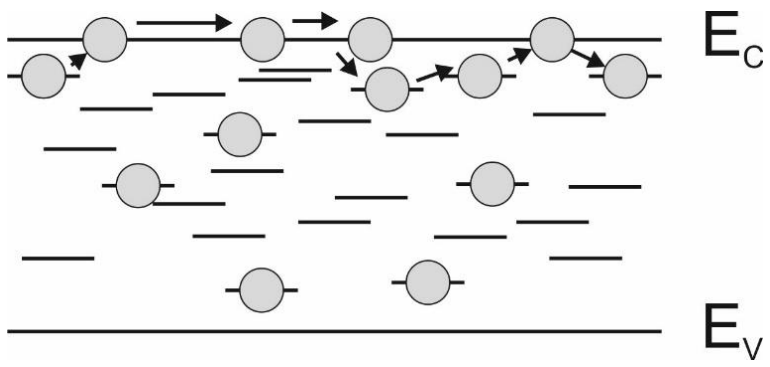

Fig. 3.8 Schematic representation of the MTR model

The *I-V* characteristics are dependent on the sub-band gap DOS which are assumed to have a Gaussian distribution in accordance with a-Si:H [29-31] and a-IGZO [32] material. Typically, the deep and tail states are represented by Gaussian distributions which are each approximated by exponential terms. The two exponential terms account for states that originate near the band edge (tail states) and away from the band edge (deep states) and the DOS (*g(E)*) is then written as:

$$g(E) = N_{tail} \exp\left(\frac{E - E_C}{kT_{tail}}\right) + N_{deep} \exp\left(\frac{E - E_C}{kT_{deep}}\right) \tag{3.14}$$

where N_{tail} and N_{deep} are the number of tail and deep states respectively, T_{tail} and T_{deep} represent the distribution of the tail and deep states respectively and is known as the characteristics temperature. E is the energy and E_C is the conduction band energy. For ZnO the defects arising from zinc interstitials (Zn_i) and oxygen vacancies (V_o) are ascribed to the tail and deep states respectively. A comparison of a Gaussian and an exponential DOS is shown in Fig. 3.9. It is evident the Gaussian distribution is predominantly fitted by the tail states. The role of the deep states is to fit the 'tail' of the distribution.

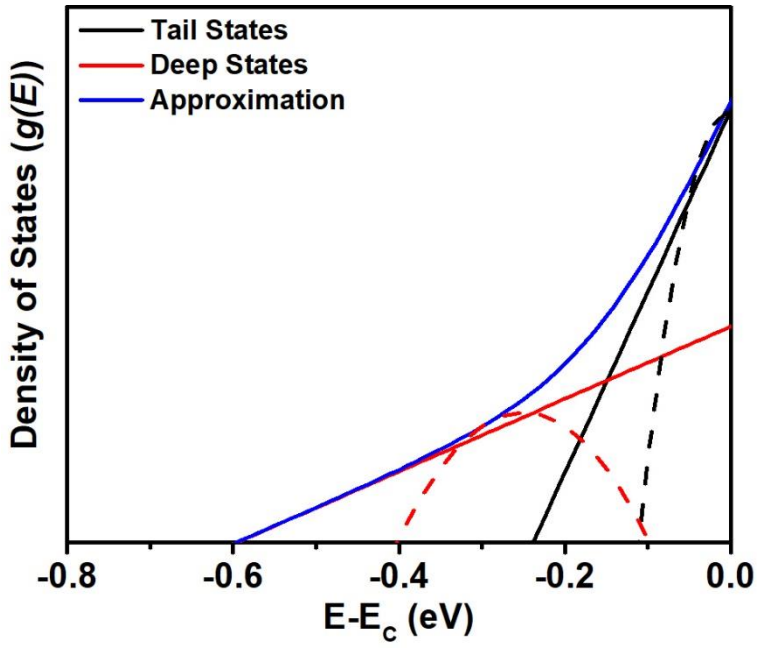

Fig. 3.9 Comparison of DOS using a two-term exponential (solid lines) expression to represent a Gaussian distribution (dashed lines). The blue line is the expression in Eqn. (3.14)

It is worth noting that the deep states influence V_{on} of the TFT and the formation of the accumulation channel. It can be shown that the tail states dominate the on characteristics of the TFT [28] and the DOS can be reduced to a single exponential expression:

$$g(E) = N_t \exp\left(\frac{E - E_C}{kT_o}\right) \tag{3.15}$$

where N_t is the total number of trapping states and T_o is the characteristic temperature of the tail states.

An analytical expression for drain current is now derived, following Torricelli *et al.* [28]. The drain current (I_D) can be expressed as:

$$I_D = \frac{W}{L}\int_0^L \frac{dV_{ch}}{dy}\int_0^{t_{zno}} \sigma(x,y)dxdy \tag{3.16}$$

where t_{zno} is the thickness of the ZnO, V_{ch} is the channel potential and σ is the film conductivity. For disordered materials that follow the MTR model, an alternative expression for σ developed by Servati *et al*. [33] is used and given as:

$$\sigma = \sigma_o \left[\frac{\frac{T_o}{T}\sin\left(\pi\frac{T}{T_o}\right)}{\pi N_t}\right]^{\frac{T_o}{T}} n_t^{\frac{T_o}{T}} \tag{3.17}$$

where n_t is the charge carrier concentration in the trapped states and σ_o is the band conductivity and defined as $\sigma_o = q\mu_b N_b$, μ_b is the mobility of carriers in the conduction band and N_b is the total number of states in the conduction band. Furthermore, it is assumed the concentration of carriers in the traps is greater than in the transport band, $n_t >> n_b$. Therefore, an approximation of the carrier concentration in the conducting channel is expressed as:

$$n_t(\varphi, V_{ch}) = n_i \exp\left[\frac{q(\varphi - V_{ch})}{kT_0}\right] \tag{3.18}$$

where n_i is the intrinsic carrier concentration and φ is the electrostatic potential. By considering the electric field dependence $F_x(x,y) = \partial\varphi(x,y)/\partial x$, Eqn. (3.16) can be modified to:

$$I_D = \frac{W}{L}\int_{V_S}^{V_D}\int_{\varphi_S}^{V_{ch}} \frac{\sigma(\varphi, V_{ch})}{-F_x} d\varphi dV_{ch} \tag{3.19}$$

where V_D and V_S are the drain and source voltages respectively, φ_s is the surface potential at the interface of the insulator and semiconductor and V_{ch} is the bulk potential. To solve Eqn. (3.19), the electric field F_x needs to be expressed as a function of V_{ch} and φ. Solving Poisson's equation to evaluate F_x, the gradual channel approximation is used which states that a small change in the x-direction. Poisson's equation is given as:

$$\nabla^2\varphi \approx -\frac{\partial F_x}{\partial x} = -\frac{qn_t}{\varepsilon_s} \tag{3.20}$$

By integrating with respect to φ in the electric field perpendicular to the channel from the semiconductor-insulator interface to the edge of the film, F_x can be represented as a function of both φ and V_{ch}:

$$F_x(\varphi, V_{ch}) = \sqrt{\frac{2n_i kT_o}{\varepsilon_s} \exp\left[\frac{q(\varphi - V_{ch})}{kT_o}\right]} \tag{3.21}$$

where an analytical drain current equation is obtained:

$$I_D = \frac{W}{L}\beta\left[(V_G - V_{FB} - \varphi_{sS})^{\gamma} - (V_G - V_{FB} - \varphi_{sD})^{\gamma}\right] \tag{3.22}$$

where φ_{sS} and φ_{sD} are the source and drain surface potentials respectively and β is given as:

$$\beta = \sigma_0 \frac{\varepsilon_s}{C_i} V_T \left(\frac{1}{\gamma - 1}\right)\left[\frac{C_i^2 \sin\left(\frac{2\pi}{\gamma}\right)}{2\pi N_t q \varepsilon_s V_T}\right]^{\frac{\gamma}{2}} \tag{3.23}$$

In the drain current expression, φ_{sS} and φ_{sD} can be evaluated for the linear and saturation operating regimes of a TFT. When the TFT is in the linear regime the φ_{sS} and φ_{sD} can be approximated to V_S and V_D respectively. For the saturation condition ($V_D \leq V_G - V_{FB}$), φ_{sS} is still V_S, however, φ_{sD} now is equal to $V_G - V_{FB}$ and hence removes the drain voltage dependency as the channel has fully saturated. Eqn. (3.22) can be further modified to account for the effect of the contact resistances of the source (R_S) and drain (R_D):

$$I_D = \frac{W}{L}\beta\left[(V_G - V_{FB} - I_D R_S)^{\gamma} - (V_G - V_{FB} - V_D - I_D R_D)^{\gamma}\right] \tag{3.24}$$

This physics-based model was implemented in MATLAB, with fitting performed using linear regression. Fits are initially obtained from the transfer characteristics and then are matched for the output characteristics with the inclusion of the contact resistances. The validity of each fit was determined by using the regression coefficient, R^2.

3.4.2 Capacitance-voltage characteristics

Capacitance-voltage (*C-V*) characteristics were performed using an Agilent LCR meter which was controlled by an in-house LabVIEW program. The parallel capacitor-resistor mode was adopted. DC Voltage sweeps were conducted from negative to positive to negative. For each DC voltage, the signal was modulated with a small a.c. signal of 5 mV.

3.4.3 References

[1] R. W. Johnson, A. Hultqvist, and S. F. Bent, "A brief review of atomic layer deposition: from fundamentals to applications," *Materials Today*, vol. 17, no. 5, pp. 236-246, 2014.

[2] S. M. George, "Atomic Layer Deposition: An Overview," *Chemical Reviews*, vol. 110, no. 1, pp. 111-131, 2010.

[3] J. R. Gaines. (2016, 2016) Challenges for Non-Ideal Atomic Layer Deposition Process and Systems. Vacuum Equipment Resource Guide. 8-17. Available: http://www.avem.org/digital/avem_2016/

[4] E. Guziewicz, M. Godlewski, L. Wachnicki, T. A. Krajewski, G. Luka, S. Gieraltowska, R. Jakiela, A. Stonert, W. Lisowski, M. Krawczyk, J. W. Sobczak, and A. Jablonski, "ALD grown zinc oxide with controllable electrical properties," *Semiconductor Science and Technology*, vol. 27, no. 7, p. 074011, 2012.

[5] P. D. Davidse and L. I. Maissel, "Dielectric Thin Films through rf Sputtering," *Journal of Applied Physics*, vol. 37, no. 2, pp. 574-579, 1966.

[6] H. Adachi, T. Hata, and K. Wasa, "5 - Basic Process of Sputtering Deposition," in *Handbook of Sputtering Technology* 2nd ed., Oxford: William Andrew Publishing, 2012, pp. 295-359.

[7] L.-Y. Chen, W.-H. Chen, J.-J. Wang, F. C.-N. Hong, and Y.-K. Su, "Hydrogen-doped high conductivity ZnO films deposited by radio-frequency magnetron sputtering," *Applied Physics Letters*, vol. 85, no. 23, pp. 5628-5630, 2004.

[8] A. Rothen, "The Ellipsometer, an Apparatus to Measure Thicknesses of Thin Surface Films," *Review of Scientific Instruments*, vol. 16, no. 2, pp. 26-30, 1945.

[9] H. Shima, H. Naganuma, and S. Okamura, "Optical Properties of Multiferroic $BiFeO_3$ Films " in *Materials Science - Advanced Topics*,Rijeka: InTech, 2013.

[10] J. A. Woollam, J. N. Hilfiker, T. E. Tiwald, C. L. Bungay, R. A. Synowicki, D. E. Meyer, C. M. Herzinger, G. L. Pfeiffer, G. T. Cooney, and S. E. Green, "Variable angle spectroscopic ellipsometry in the vacuum ultraviolet," in *International Symposium on Optical Science and Technology*, San Diego, CA, USA 2000, vol. 4099, pp. 197-205: SPIE.

[11] H. G. Thompkins and E. A. Irene, "Data Analysis for Spectroscopic Ellipsometry," in *Hanndbook of ellipsometry*1st ed. Norwich, NY: William Andrew Publishing, 2004, p. 239.

[12] C. M. Herzinger, B. Johs, W. A. McGahan, J. A. Woollam, and W. Paulson, "Ellipsometric determination of optical constants for silicon and thermally grown silicon dioxide via a multi-sample, multi-wavelength, multi-angle investigation," *Journal of Applied Physics*, vol. 83, no. 6, pp. 3323-3336, 1998.

[13] B. Johs, C. M. Herzinger, J. H. Dinan, A. Cornfeld, and J. D. Benson, "Development of a parametric optical constant model for $Hg_{1-x}Cd_xTe$ for control of composition by spectroscopic ellipsometry during MBE growth," *Thin Solid Films*, vol. 313–314, pp. 137-142, 1998.

[14] J. A. Woollam, *Gerneral Ocillator Layer*, 1st ed. (Guide to Using WVASE). 2012, pp. 32-39.

[15] H. G. Tompkins and E. A. Irene, "Polarized Light and Ellipsometry," in *Handbook of Ellipsometry* 1st ed. Norwich, NY: William Andrew, 2004, pp. 3-92.

[16] J. Tauc, "Optical properties and electronic structure of amorphous Ge and Si," *Materials Research Bulletin*, vol. 3, no. 1, pp. 37-46, 1968.

[17] J. F. Moulder, W. F. Stickle, P. E. Sobol, and K. D. Bomben, *Handbook of X-ray photoelectron spectroscopy*. Eden Prairie, MN: Physucak Electronics Inc., 1995.

[18] J. F. Watts, "X-ray photoelectron spectroscopy," *Vacuum*, vol. 45, no. 6–7, pp. 653-671, 1994.

[19] M. C. Biesinger, L. W. M. Lau, A. R. Gerson, and R. S. C. Smart, "Resolving surface chemical states in XPS analysis of first row transition metals, oxides and hydroxides: Sc, Ti, V, Cu and Zn," *Applied Surface Science*, vol. 257, no. 3, pp. 887-898, 2010.

[20] M. P. Seah, "Quantification of AES and XPS," in *Practical Surface Analysis by Auger and X-ray Photoelectron Spectroscopy* D. Briggs and M. P. Seah, Eds. Chichester, UK: John Weley & Sons, 1983, p. 204.

[21] A. Herrera-Gomez, M. Bravo-Sanchez, O. Ceballos-Sanchez, and M. O. Vazquez-Lepe, "Practical methods for background subtraction in photoemission spectra," *Surface and Interface Analysis*, vol. 46, no. 10-11, pp. 897-905, 2014.

[22] Y. Waseda, E. Matsubara, and K. Shinoda, *X-Ray diffraction crystallography*. [electronic book] : introduction, examples and solved problems (Online access with purchase: Springer). Berlin ; Springer, 2011.

[23] A. L. Patterson, "The Scherrer Formula for X-Ray Particle Size Determination," *Physical Review*, vol. 56, no. 10, pp. 978-982, 1939.

[24] K. N. Shinde, *Phosphate phosphors for solid-state lighting*. [electronic book] (Springer series in materials science: v.174). Berlin ; Springer, 2012., 2012.

[25] P. T. Hsieh, Y. C. Chen, K. S. Kao, and C. M. Wang, "Luminescence mechanism of ZnO thin film investigated by XPS measurement," *Applied Physics A*,e vol. 90, no. 2, pp. 317-321, 2008.

[26] K. L. Chopra, *Thin Film Phenomena*. New York, NY: McGraw-Hill, 1969.

[27] F. M. Hossain, J. Nishii, S. Takagi, A. Ohtomo, T. Fukumura, H. Fujioka, H. Ohno, H. Koinuma, and M. Kawasaki, "Modeling and simulation of polycrystalline ZnO thin-film transistors," *Journal of Applied Physics*, vol. 94, no. 12, pp. 7768-7777, 2003.

[28] F. Torricelli, J. R. Meijboom, E. Smits, A. K. Tripathi, M. Ferroni, S. Federici, G. H. Gelinck, L. Colalongo, Z. M. Kovacs-Vajna, D. d. Leeuw, and E. Cantatore, "Transport Physics and Device Modeling of Zinc Oxide Thin-Film Transistors Part I: Long-Channel Devices," *IEEE Transactions on Electron Devices*, vol. 58, no. 8, pp. 2610-2619, 2011.

[29] L. Colalongo, "A new analytical model for amorphous-silicon thin-film transistors including tail and deep states," *Solid-State Electronics*, vol. 45, no. 9, pp. 1525-1530, 2001.

[30] T. J. King, M. G. Hack, and I. W. Wu, "Effective density-of-states distributions for accurate modeling of polycrystalline-silicon thin-film transistors," *Journal of Applied Physics*, vol. 75, no. 2, pp. 908-913, 1994.

[31] M. Shur and M. Hack, "Physics of amorphous silicon based alloy field-effect transistors," *Journal of Applied Physics*, vol. 55, no. 10, pp. 3831-3842, 1984.

[32] C. Chen, K. Abe, H. Kumomi, and J. Kanicki, "Density of States of a-InGaZnO From Temperature-Dependent Field-Effect Studies," *IEEE Transactions on Electron Devices*, vol. 56, no. 6, pp. 1177-1183, 2009.

[33] P. Servati, A. Nathan, and G. A. J. Amaratunga, "Generalized transport-band field-effect mobility in disordered organic and inorganic semiconductors," *Physical Review B*, vol. 74, no. 24, p. 245210, 2006.

Chapter 4

4. Alloying of magnesium zinc oxide for thin-film transistors

4.1. Introduction

Atomic layer deposition (ALD) zinc oxide (ZnO) thin-films are attractive due to the controllability and uniformity of the films. However, these films are inherently highly conductive due to high carrier concentration and hence methods are required for the reduction to a level suitable for the realisation of thin-film transistors (TFTs) so that they can be turned off. A common solution to reduce the conductivity of ALD ZnO films is to lower the deposition temperature [1-3]. An alternative approach to controlling the conductivity of ZnO, is doping/alloying whereby an additional precursor replaces that of the Zn after *x* cycles. The focus of this chapter is the use of magnesium as a dopant with the aim of reducing carrier concentration but enhancing mobility to maximise the on-current. Extensive research has been conducted into the band gap engineering of magnesium zinc oxide (MgZnO) films using deposition techniques such as RF-sputtering [4-10], ALD [11, 12] and metal-organic chemical vapour deposition (MOCVD) [13-20]. Here we use the term alloying as both the Zn and Mg are divalent ions (2+), hence using doping is inappropriate. A number of benefits have been established by doping ZnO with Mg such as: a wider band gap; increasing towards that of MgO; 7.7 eV [9, 14, 15, 18, 20] and reducing the concentration of oxygen vacancies (V_o) [20] as a result of the higher oxygen affinity of magnesium. Furthermore, under annealing conditions; the MgZnO exhibits larger grain sizes, which could reduce the scattering of charge carriers and hence enhance the mobility [7, 8].

MgZnO films deposited by RF sputtering [7-10] and MOCVD [18-20] have been studied for TFT applications. It was demonstrated that by increasing the Mg content within the films, the *On/Off* ratio was increased in MOCVD films [19, 20]. Small concentrations of Mg in MOCVD films (< 10 %) showed improved mobilities [19, 20], whereas, for sputtered films, even small Mg concentrations resulted in degradation of the mobility and subthreshold swing [9]. Ku *et al.* [20] showed the improvement of thermal stability of TFTs by Mg doping due to the suppression of V_o and the introduction of strong Mg-O bonds. Tasi *et al.* [7] and Li *et al.* [8] demonstrated the influence of annealing temperatures on MgZnO TFTs. In both studies, a higher annealing temperature (> 300°C) demonstrated improvement in the stability under positive and negative gate biasing respectively. Remashan *et al.* [18] demonstrated that using MgZnO as a buffer layer between the gate oxide and ZnO film enhanced the saturation mobility and subthreshold swing.

Although deposition of MgZnO films by RF-sputtering and MOCVD has been extensively reported, preparation by ALD as a viable technique still requires investigation. ALD MgZnO films have been investigated as buffer layers in Cu(In,Ga)Se_2-based solar cells [11] with increasing Mg cycle ratios. The $Mg_xZn_{1-x}O$ films were deposited using the magnesium precursor ($MgCp_2$), at low ALD temperatures, from 105 to 180 °C.

MgZnO with cycle percentages ranging from 0 % (pure ZnO) to 33 % MgZnO for TFT application are reported in this chapter. The physical and electrical characteristics of the films are presented and discussed.

4.2. Experimental Details

4.2.1 Deposition of MgZnO alloys

The alloying of MgZnO films were deposited by ALD by the functional materials group at the University of Liverpool onto both glass (Fisher Scientific) and thermally oxidised n-type silicon substrates (Si Mat) using the precursors bis(ethylcyclopentadienyl)magnesium ($Mg(CpEt)_2$) (Strem), diethyl zinc (DEZn) (Strem) and deionised water. The bubbler temperatures of the Zn and Mg precursors entering the chamber were set to room temperature and 95 °C respectively. Initially, the substrate (deposition) temperature was set to 200 °C. The Mg was incorporated into the film by increasing the cycle fractions between the Mg and Zn precursor to form $Mg_{1-x}Zn_xO$. After successive x cycles of the DEZn, a single MgO layer was deposited by exposing the surface to $Mg(CpEt)_2$ and water vapour. The cycle percentages investigated in this chapter are given in Table 4.1 and are calculated using the cycle fractions. For example, using a cycle fraction of 7:1 (Zn:Mg), for every eight metal deposition cycles, seven will use the DEZn precursor and one the $Mg(CpEt)_2$. The equivalent cycle percentage is calculated by using; (Mg cycles/total cycles)×100 = (1/1+7) × 100 = 12.5 %. Although ALD is a layering process, the films are considered to be mixed, as during each cycle only a partial mono-layer is deposited. Moreover, as the substrate is not atomically flat, the surface topology ensures further mixing of the film. The effect of deposition temperature of the MgZnO films was investigated between 125 and 250 °C. Furthermore, TFTs were fabricated using both shadow masks and patterned by photolithography (Shipley S1813 as the photoresist and Micro Dev for the developer [DOW]) using a lift-off process, described in section 4.5. For both processes ~ 70 nm thick aluminium (Fisher scientific) source and drain contacts were deposited using thermal evaporation. The TFT structure used by both fabrication techniques is shown below in Fig. 4.1.

Table 4.1 MgZnO cycle percentages investigated in chapter 4

Cycle Fraction (Zn:Mg)	Equivalent cycle percentage (%)
1:0	0
49:1	2.0
20:1	4.7
11:1	9.1
9:1	10.0
8:1	11.1
7:1	12.5
5:1	16.7
3:1	25.0
2:1	33.3

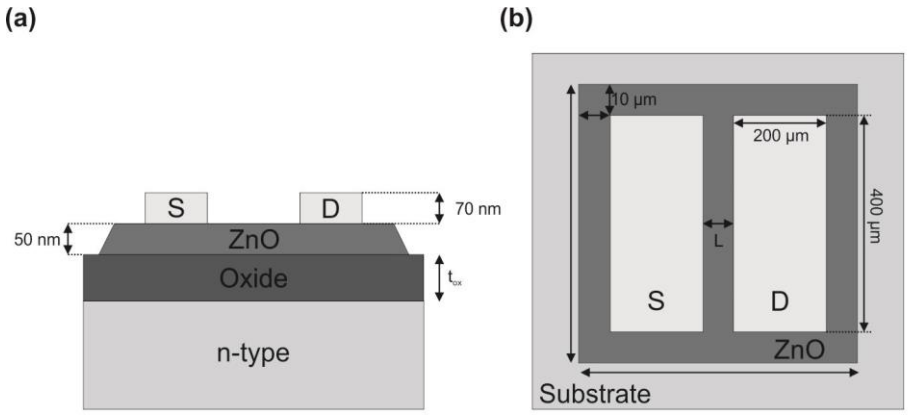

Fig. 4.1 (a) cross section and (b) top view of the MgZnO TFT structure

4.2.2 X-ray photoelectron spectroscopy (XPS) and inverse photoelectron spectroscopy (IPES)

X-ray photoelectron spectroscopy (XPS) and inverse photoelectron spectroscopy (IPES) measurements were conducted to probe the valence and conduction bands respectively of pure ZnO and 12.5 % MgZnO films. Experimental measurements of XPS and IPES were conducted in the nanomaterials characterisation lab in the Stephenson Institute for Renewable Energy at the University of Liverpool. The measurements were performed on thin interfacial (< 5 nm) and bulk (~ 20 nm) samples in a standard ultra-high vacuum chamber operating at a base pressure of less than 2×10^{-10} mbar with hydrogen as the main residual gas.

The core level structure and occupied density of states in the valence band were probed by XPS using a SPECS monochromatic Al Kα X-ray source (hν = 1486.6 eV) operating at

200 W, and a PSP Vacuum Technology electron energy analyser operating with a typical constant pass energy of 10 eV. The spectrometer was calibrated so that the Ag $3d_{5/2}$ photoelectron line had a binding energy (BE) of 368.27 eV, a full width at half maximum (FWHM) of 0.6 eV being the spectral resolution for this study and operating at a constant 10 eV pass energy. Charging of the samples was corrected by setting the C 1s peak, arising from adventitious carbon species, to 284.6 eV for all samples.

The conduction band minima (CBM) and unoccupied density of states were measured using a PSP Vacuum Technology IPES system which consisted of a BaO cathode dispenser as a low energy electron source and an isochromatic NaCl photon detector, each mounted at an incidence angle of 45° to the sample normal. The IPES detector operated at a nominal resolution of 0.7 eV and the spectra were recorded over several hours to obtain good quality statistics. The energy scale was calibrated using the Fermi energy of a clean polycrystalline silver foil. As a reference sample, bulk (20 nm) and interfacial (5 nm) ZnO films were prepared on 50 nm SiO_2/Si substrates.

4.3. Initial electrical characterisation of MgZnO thin film transistors

Initial characterisation of MgZnO TFTs were conducted on films deposited at 200 ^oC with increasing Mg cycle percentages from 0 to 33 %. All samples were subjected to post deposition annealing at 300 ^oC in air for 1 hour. The devices were fabricated using shadow masks, where the channel length (L) and width (W) for all the devices were 60 µm and 2000 µm respectively. To benchmark the TFT performance against results in the literature, standard field effect transistor parameter extraction was applied using the saturation MOSFET Eqn. (3.7). Detailed method for parameter extraction is described in section 3.4.1.1. The collated results for increasing Mg cycle percentages are shown in Table 4.2, with scatter plots in Fig. 4.2.

Table 4.2 Average TFT parameters for MgZnO with increasing cycle percentages from 0 to 33.3 %, with 5 measurements per cycle percentage

Mg Cycle percentage (%)	***On/Off* ratio**	**V_T (V)**	**μ_{sat} (cm^2/Vs)**	**Effective *SS* (V/decade)**
0	1.0×10^4	9.3	1.4	N/a
9.1	5.6×10^3	6.1	4.3	1.97
10.0	2.9×10^5	7.0	3.7	1.22
11.1	2.8×10^5	6.6	2.9	1.2
12.5	1.6×10^6	7.1	4.0	0.96
16.7	5.3×10^5	7.7	3.1	0.98
25.0	2.2×10^5	8.6	1.4	1.17
33.3	1.1×10^5	9.5	0.47	1.21

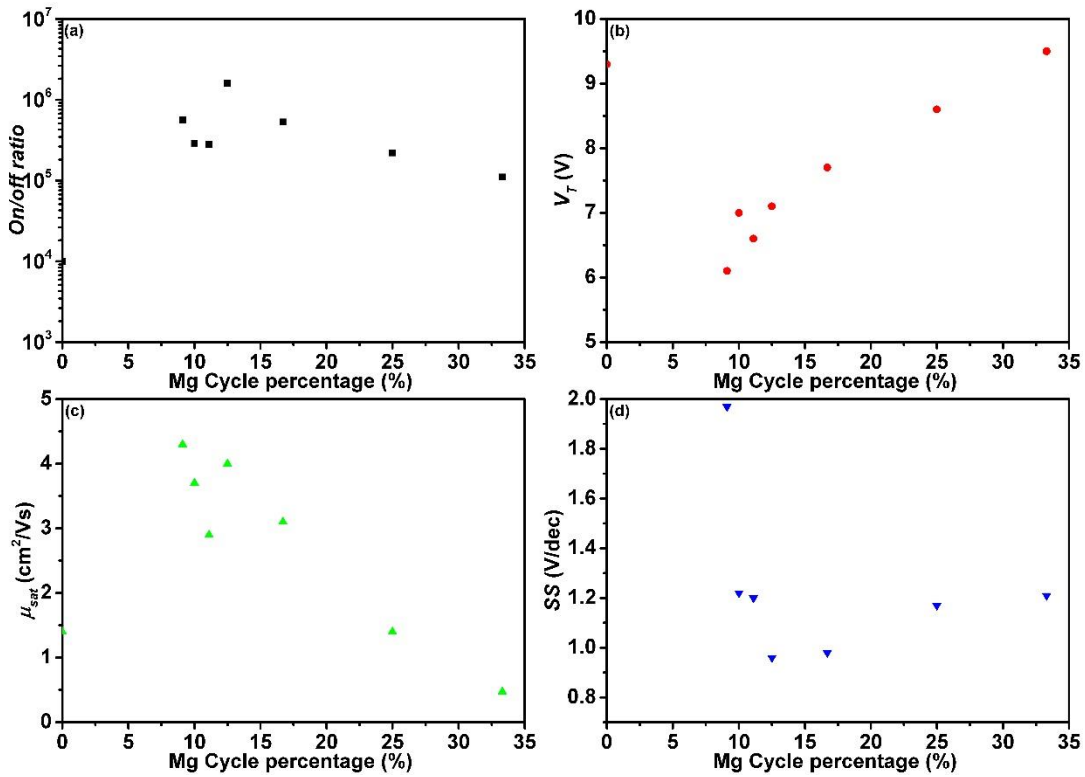

Fig. 4.2 Average scatter plots for the TFT parameters (a) *On/Off* ratio, (b) V_T, (c) μ_{sat} and (d) the effective *SS* of increasing Mg cycle percentages from 0 to 33 %.

In general, films with an Mg cycle percentage > 9.1 % achieved acceptable *On/Off* ratios for shadow mask devices, with a maximum of 1.6×10^6 obtained for 12.5 % MgZnO. The effective saturation mobility in Table 4.2 and Fig. 4.2Fig. 4.2(c) shows a tendency to decrease from 4.3 to 0.47 cm^2/Vs as the magnesium cycle percentages increase across the range from 9.1% to 33.3 %. The reduction of saturation mobility is indicative of either grain boundary or impurity scattering, which will be discussed further in the following section. The effective

threshold voltage for the devices exhibits the opposite trend increasing from 6.1 V to 9.5 V, respectively. Furthermore, as the magnesium content is increased, the effective *SS* reduces, where it is assumed that the SiO_2/MgZnO interface has improved. However, as the cycle percentages are further increased above 16.7 %, the subthreshold swing begins to degrade. This effect is similar to that reported for RF sputtered MgZnO TFTs by Ku *et al.* [20], whereby an optimum Mg concentration of 6 % (wt) enhances the TFT characteristics. A further increase of the Mg doping concentration caused the TFTs to degrade, which is associated to either increased impurity scattering or effective mass of the electrons from the alloying process [20].

From the parameters presented in Table 4.2 and Fig. 4.2 (a-d), it is apparent that the optimum TFT performance is achieved for the 12.5 % Mg ratio. Fig. 4.3 shows (a) the output and (b) the transfer characteristics for a typical MgZnO TFT fabricated using the 12.5 % cycle percentage film. The parameters obtained for the device were: *On/Off* ratio = 1.6×10^6, μ_{sat} = 4 cm^2/Vs, V_T = 7.1 V and the effective *SS* = 0.96 V/dec. Furthermore, the output characteristics in Fig. 4.3(a) demonstrate good saturation for all the applied V_{GS}. However, it is worth noting the apparent small zero-bias leakage observed in the output characteristics which is likely to be due to gate leakage and effectively shifts the characteristics by ~ 200 mV. The effect of gate leakage will be investigated later in this chapter.

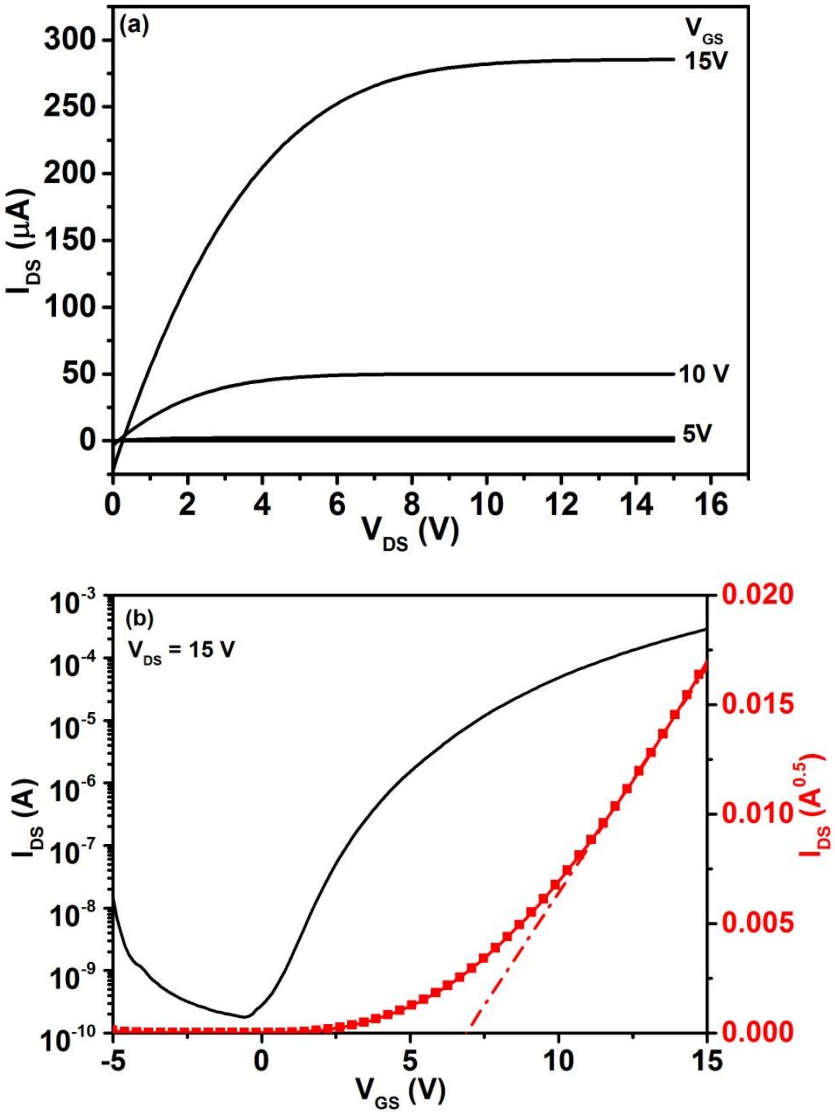

Fig. 4.3 (a) output and (b) transfer characteristics of 12.5 % MgZnO TFT deposited at 200 ^{o}C. $I_D^{0.5}$ and linear extrapolation (dashed line) are shown in (b)

4.4. Physical characterisation

The physical properties of selected films electrically characterised in the above section will be investigated.

4.4.1 X-ray diffraction

X-ray diffraction (XRD) was performed on MgZnO films deposited onto glass with the selected Mg cycle percentages: 0,2, 4.7, 10 and 12.5 % by the functional materials group at the University of Liverpool. Moreover, the films were subjected to post deposition air annealing for 1 hour at 300 ^{o}C prior to characterisation. The films were probed with a Cu Kα radiation (0.15 nm, 40 kV, and 50 mA), with the diffraction patterns shown in Fig. 4.4 demonstrating the crystalline structure of the films undergoing significant changes. As the Mg cycle percentages increased from 2 to 12.5 %, the c-axis (002) oriented growth diminishes, which is indicated by the decreasing ratio of the (002) diffraction peak with respect to the (100) and (101) peaks. Furthermore, the (002) peak shifts to a higher diffraction angle; this has been reported by Kim *et al.* [21] suggesting the Mg^{2+} ion is substituting the Zn^{2+} ions in the lattice. This shift is due to the Mg^{2+} ion having a smaller radius (0.65 Å) than the Zn^{2+} ion (0.74 Å) causing a contraction in the lattice. Notably, the full-width at half maxima (FWHM) of the diffraction peaks for all cycle percentages shown remains unchanged, indicating that the crystalline size is constant. An average grain size of 20 nm was determined using the Scherrer equation [22]; Eqn. (3.6) in section 3.3.3. The constant grain size indicates that the change in saturation mobility is associated with impurity scattering and not grain boundary scattering.

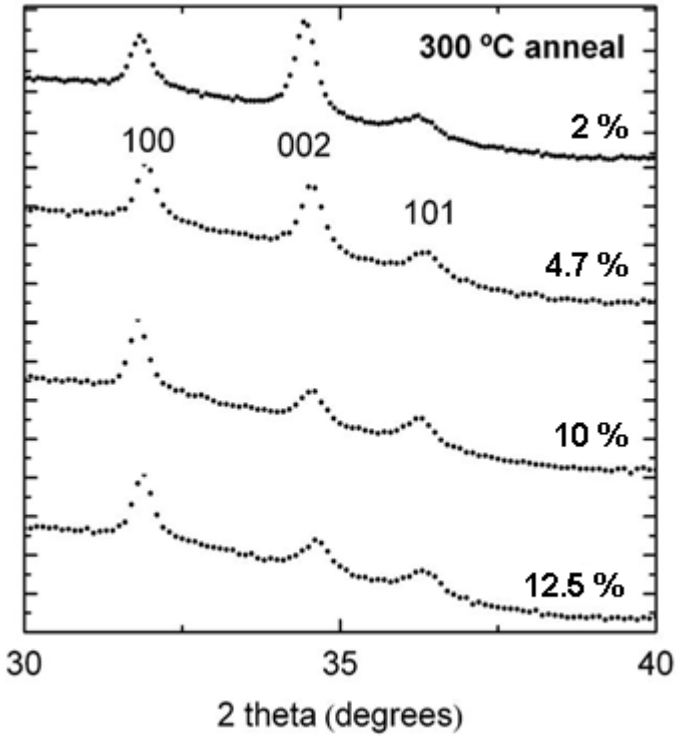

Fig. 4.4 XRD patterns for post deposition air annealed at 300 ºC for 1-hour MgZnO films with increasing cycle percentages from 2 to 12.5 %

4.4.2 Optical properties

The optical properties were measured by both spectroscopic ellipsometry (SE) and photoluminescence (PL). SE measurements were conducted at 3 angles; 65, 70 and 75º, and retrospectively fitted using a predefined model by J. A. Woollam consisting of a Psemi oscillator. Measurements were performed on pure ZnO and 12.5 % MgZnO deposited at 200 ºC as this composition proved to provide the best electrical characteristics in section 4.3. A Tauc plot comparing the absorption edge for as-deposited ZnO and 12.5 % is shown in Fig. 4.5. Fig. 4.5 demonstrates that the absorption edge shifts to higher energies for 12.5 % MgZnO. By extrapolating the non-absorbing region as described in chapter 3.3.1, the band gap (E_g) is estimated to increase from 3.24 to 3.44 eV. The increase in E_g can be explained by the Burstein-Moss effect and has been demonstrated for other MgZnO films [21, 23-25]. The Burstein-Moss effect relates to energy states just above the conduction band being occupied by Mg induced states, thus pushing the effective absorption edge to higher energies [26].

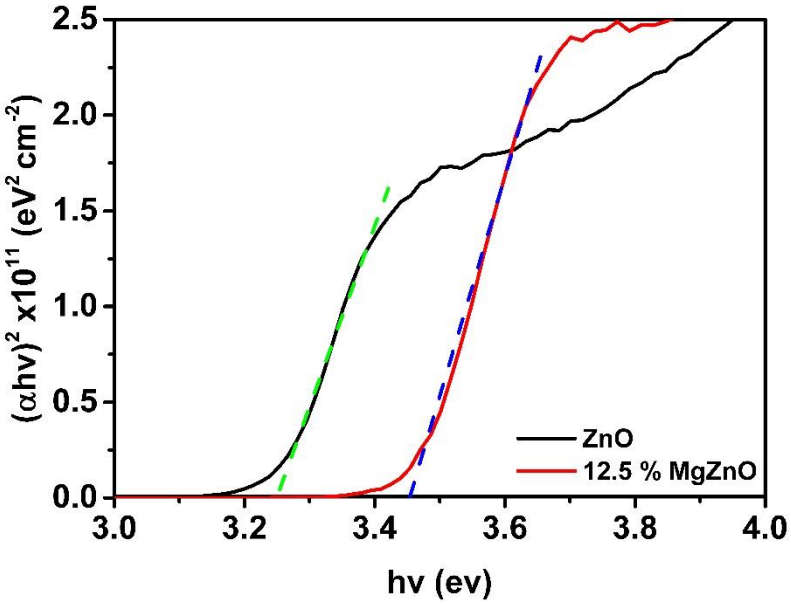

Fig. 4.5 Tauc plot of as-deposited pure and MgZnO with a cycle percentage of 12.5 %

PL measurements were conducted on as-deposited (at 200 °C) and air annealed at 300 °C for 1-hour MgZnO films on glass, with an Mg cycle percentage of 12.5 %. The measurements were performed by the functional materials group at the University of Liverpool. The films were probed using a He-Cd laser with a wavelength of 325 nm (a 3.82 eV excitation). Fig. 4.6 shows the PL spectra for the 12.5 % MgZnO as-deposited and 1-hour air annealed at 300 °C. The as-deposited spectra exhibit a blue emission peak 366 nm, relating to an E_g = 3.38 eV and is 1.7 % less than the extracted E_g obtained from SE. The variation in the obtained E_g is likely to originate from the use of different samples being measured. However, they demonstrate good agreement in E_g from different deposition occasions, implying consistent Mg concentrations. Moreover, the effect of annealing shifts the blue emission peak to 360 nm, resulting in a further increase in E_g to 3.48 eV. The blue shift after annealing can be ascribed to the increased incorporation of the Mg dopant into the crystal structure and associated activation.

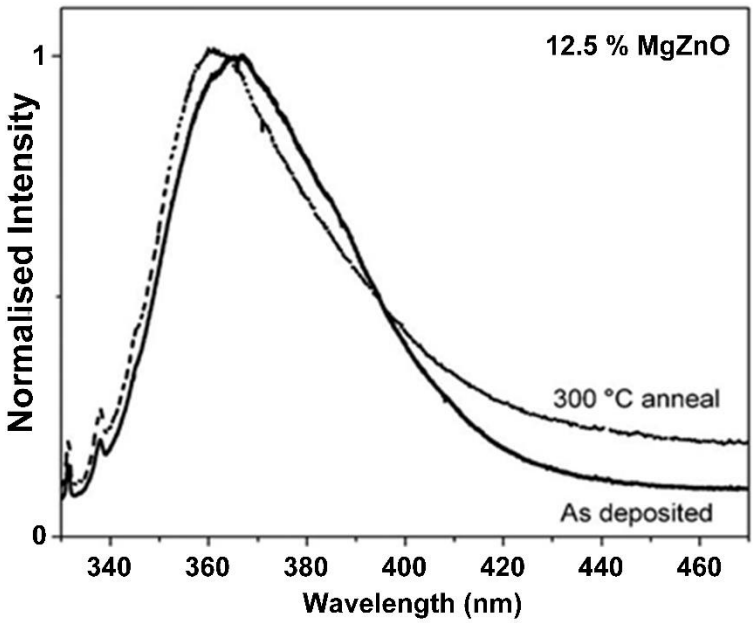

Fig. 4.6 UV photoluminescence of as deposited (solid line) and 300 °C annealed (dashed) 12.5 % MgZnO films

4.4.3 X-ray photoelectron spectroscopy and inverse photoelectron spectroscopy

The XPS spectra obtained from bulk ZnO and 12.5 % MgZnO for Mg 2p, Zn 2p and O 1s core level (CL) are shown in Fig. 4.7(a-c). A Voigt function was used to fit the CL spectra and to determine the binding energies; this technique introduces an error of ± 0.05 eV. A Voigt function is a mathematical function, widely used in spectroscopy fitting. It consists of a convolution of Gaussian and Lorentz distributions. This approach allows for the widening of a normal distribution, thus accounting for tail distributions. A Shirley-type background (explained in section 3.3.2) was applied to remove measurement noise. Fig. 4.7(a) shows the fitted envelope of the Mg 2p CL, with the corresponding sub-peaks. It is evident that two Mg species are present within the film at the binding energies of 50.3 and 49 eV corresponding to Mg-O and Mg^{2+} replacing the Zn^{2+} ions respectively [27-29]. Moreover, the ratio between species associated to Mg^{2+} and Mg-O sub peaks is 13:7. The fitted Zn 2p CL for pure (bottom) and 12.5 % MgZnO (top) in Fig. 4.7(b) have a binding energy of 1021.1 eV and 1020.9 eV respectively, which are associated with Zn-O bonds. The shift in CL to lower binding energies is due to charge transfer associated with the presence of Mg ions in the lattice and is consistent with observations reported by Su *et al.* [29] and Liang *et al.* [28]. The CL spectra for O 1s in Fig. 4.7(c) are composed of two and four sub-peaks for the pure and 12.5 % MgZnO respectively. The sub-peaks for the ZnO spectra are associated with Zn-O and oxygen atoms in the vicinity of an oxygen vacancy (labelled as O^{2-} deficiency peak) at the binding energies 529.7 and 531.2 eV respectively. The 12.5 % MgZnO sub-peaks are attributed to Zn-O and Mg-O species, O^{2-} deficiency peak and increased surface oxygen such as O-C-O or hydroxyl

groups. The Zn-O binding energy does not exhibit a shift and remains at 529.7 eV, whereas the O^{2-} deficiency peak shifts by 0.3 eV to 531.5 eV. The sub-peak with a binding energy of 530.6 eV can be associated with Mg-O [30] and is consistent with MgZnO films reported by Etaheri *et al.* [27] and Hullavarad *et al.* [31]. The final sub-peak at 532.4 eV is related to O-C-O or hydroxyl groups [32], presumably caused by residue from the Mg precursor [33]. The relative ratios associated with O^{2-} deficiencies between ZnO and 12.5 % MgZnO are 32.1 % and 17.5 % respectively, demonstrating that the act of alloying with Mg helps to reduce the oxygen vacancies within the ZnO matrix. Moreover, the Mg allows for the formation of Zn vacancies (V_{Zn}) in the lattice, which act as acceptor like defects. The effect of acceptor-like doping in MgZnO has been shown by Chein *et al.* [34] and Lishu *et al.* [35] to reduce the conductivity of the film. This in turn may explain the reduction of the perceived conductivity of the films which is associated with the TFT characteristics highlighted in Table 4.2 and Fig. 4.2 (a-d). Furthermore, the alloying process results in an increase in the band gap and hence a reduction of the intrinsic carrier concentration. Thus, as the carrier concentration increase, so does the conductivity, assuming a constant mobility.

The valence band offset (VBO) between the 12.5 % MgZnO and pure ZnO was evaluated using Kraut's method [36]. This involves examining the Si $2p_{3/2}$ and Zn $2p_{3/2}$ core levels from the bulk SiO_2 and its interface with the ZnO layer. The VBO is defined in the Kraut method as the difference between the core level and VBM of two bulk materials and the difference of the core levels of the two materials at the interface, with the equation given below:

$$VBO = \delta_{SUB} + \delta_{INT} - \delta_{OXIDE} \tag{4.1}$$

where δ_{SUB}, and δ_{OXIDE} are the energy differences between the chosen reference core-levels in the substrate and bulk oxide samples and their respective valence band maxima (VBM), while δ_{INT} refers to the BE difference for the former two core-levels for the interfacial sample [36]. The corresponding core level spectra for MgZnO on SiO_2 are shown in Appendix A. Kraut's method alleviates the presence of interface states with the use of δ_{INT}, which considers the presence of defects at the SiO_2/ZnO interface [36]. However, it must be noted that it is assumed that the interface state density is identical between the interfacial and bulk ZnO samples. A measurement error ± 0.15 eV is achieved when estimating the VBO, due to the determination of the CL (± 0.1 eV) and VBM through the linear extrapolation (± 0.05 eV) of the band edge shown in Fig. 4.8. Obtained VBO for both ZnO and MgZnO deposited on SiO_2 are shown in Table 4.3. The VBO for the MgZnO/SiO_2 interface is 1.9 ± 0.15 eV, whereas for the ZnO/SiO_2 the VBO = 2.0 ± 0.15 eV. This corresponds to a change in VBO of 0.1 eV between the ZnO/SiO_2 and MgZnO/SiO_2 interfaces, which is within the error of the Kraut method, hence no significant change can be deduced.

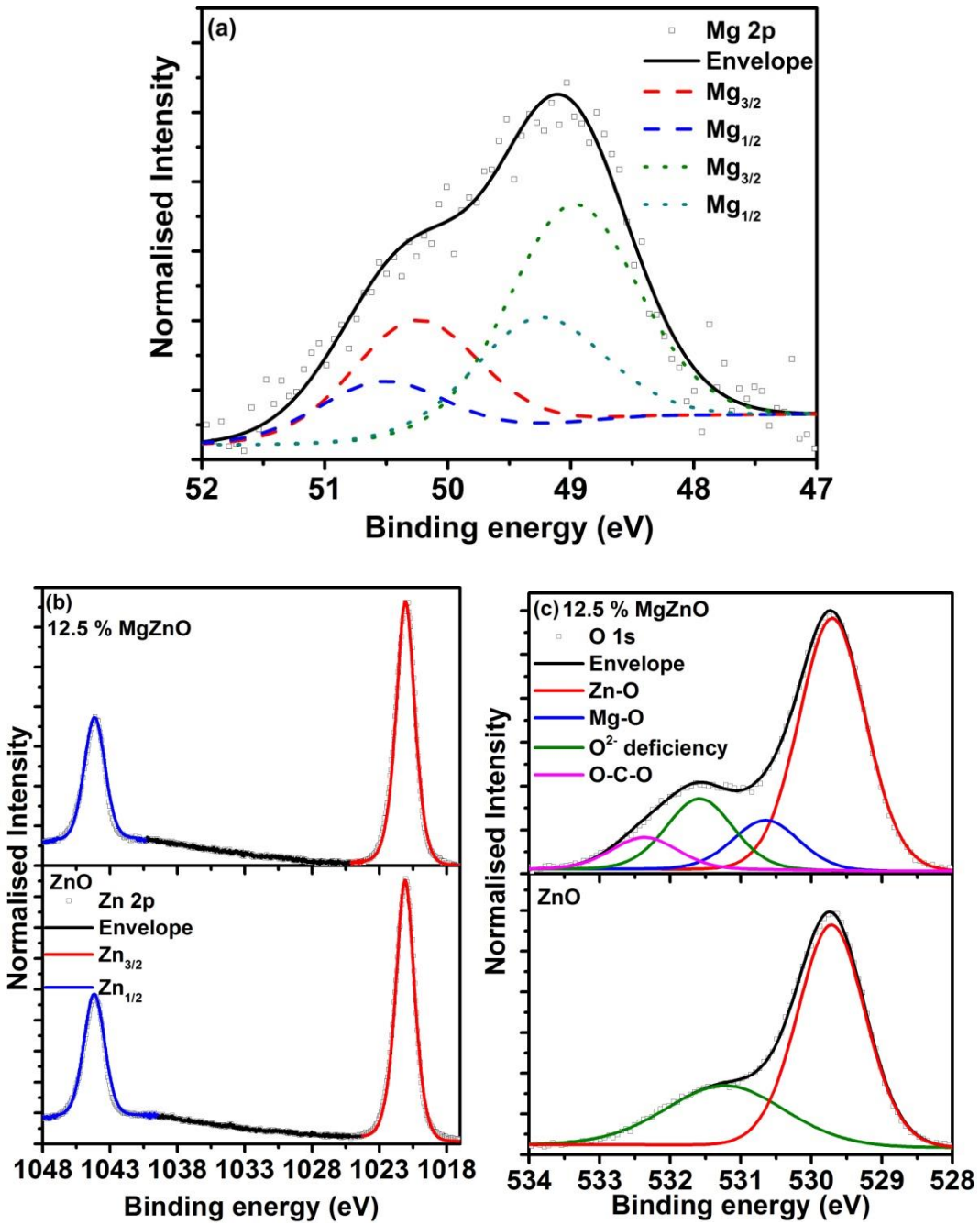

Fig. 4.7 (a) Mg 2p core level for 12.5 % MgZnO, associated with Mg-O (long dashes) and Mg-Mg (short dashes) (b) Zn 2p core level for bulk ZnO and 12.5 % MgZnO and (c) O 1s core level for bulk ZnO and 12.5 % MgZnO

Table 4.3 Determination of the valence band offset (VBO) for ZnO and MgZnO on SiO_2 using Kraut method [36]

Sample		Binding Energy (eV)			δ_{SUB}	δ_{OXIDE}	δ_{INT}	VBO
		Zn $2p_{3/2}$	Si $2p_{3/2}$	VBM	(eV)	(eV)	(eV)	(eV)
SiO_2	Bulk	--	103.09	4.94	--	98.15	--	--
ZnO	Interface	1021.19	102.47	--	--	--	918.72	2.00
	Bulk	1021.07	--	2.29	1018.87	--	--	
MgZnO	Interface	1021.40	102.67	--	--	--	918.73	1.90
	Bulk	1021.04	--	2.37	1018.75	--	--	

IPES was used to probe the effect that Mg doping of ZnO has on the conduction band minima (CBM), which is determined by linear extrapolation of the leading edges to the baseline in Fig. 4.8. The low binding energy represents the VBM and the high binding energy represents the CBM and is referenced to the Fermi level (E_f) of the system. The CBM positions for ZnO and MgZnO were found to be 0.83 ± 0.14 eV and 1.20 ± 0.14 eV respectively. This supports the suggestion that the Burstein-Moss effect is responsible for the conduction band shift to higher energies with increasing Mg doping of ZnO. The surface band gap (E_g) can be extracted through the difference of the determined CBM and VBM positions and is shown in Fig. 4.8. The E_g obtained is 3.02 and 3.49 eV for ZnO and 12.5 % MgZnO respectively. The discrepancy between the extracted E_g values between the PL/SE measurements and the surface band gap is likely to be due to the surface sensitive nature of the XPS/IPES measurement, whereas PL and SE measurements determine the bulk band gap.

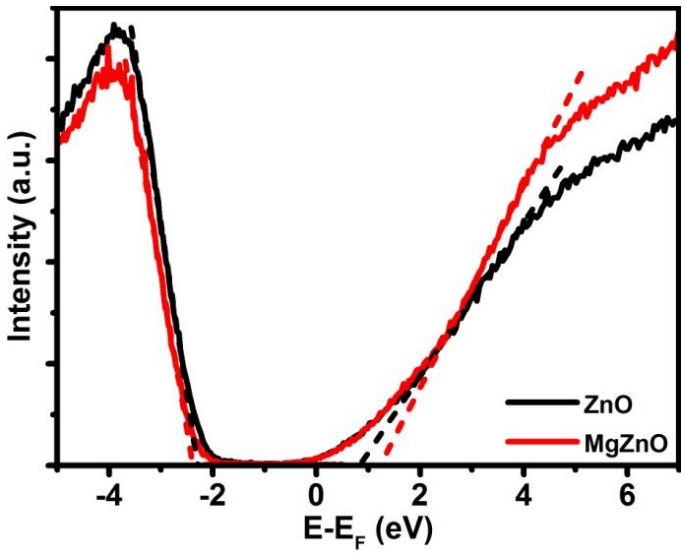

Fig. 4.8 Valence and conduction band edge obtained from XPS and IPES respectively for the ZnO and MgZnO films where the Fermi level is at 0 eV

A comparison of the energy band diagram under the flat band condition of ZnO and MgZnO on Si/SiO2 are shown in Fig. 4.8(a) and (b) respectively. The band diagrams are constructed by combining the VBO determined from Kraut's method and the Fermi-level position from the relative valence band edge in Fig. 4.7. Both values are given for the band edge due to the differences in the extracted values between XPS/IPES and SE/PL measurements. In Fig. 4.8, the values given in italics correspond to the band gap extracted from SE/PL. The vacuum level was determined from the conduction band edge of the SiO_2 layer [37]. The discrepancy between the derived electron affinities (χ) is a result of the different band gaps obtained from the two measurement techniques. The band diagrams support the fact that the Burstein-Moss effect is the dominant factor for band-gap widening as the conduction band shifts to higher energies, due to the formation of MgO species in the ZnO matrix.

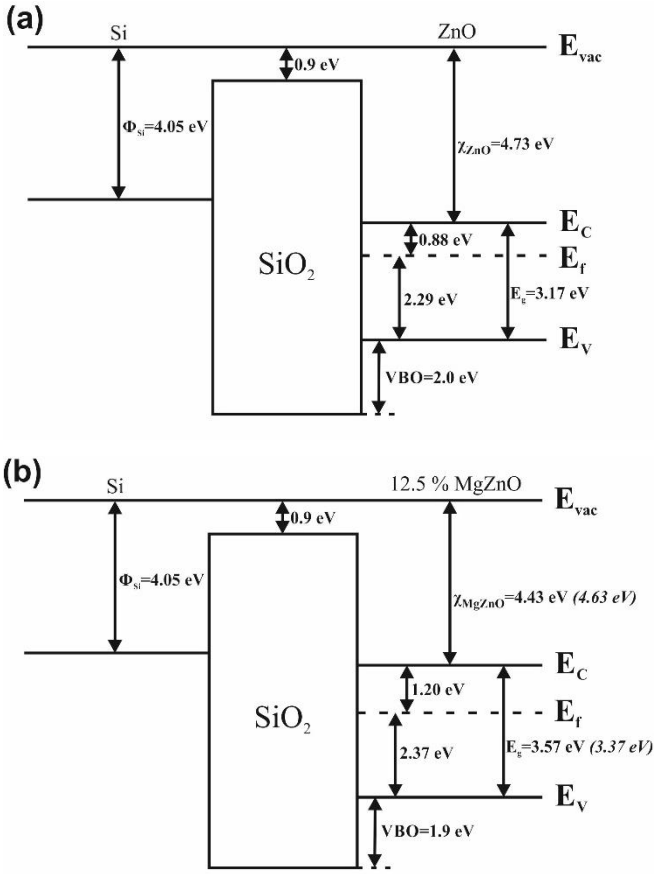

Fig. 4.9 Flat band energy band diagram for (a) ZnO on Si/SiO_2 and (b) 12.5 % MgZnO on Si/SiO_2 with the different E_g values derived from XPS and SE (italics)

4.5. Improved electrical characteristics

In section 4.3, it was evident that the 12.5 % MgZnO provided the best electrical characteristics overall. The optimal deposition temperature was therefore investigated using this MgZnO film composition between the temperatures of 125 and 250 °C. The extracted TFT parameters are shown in Table 4.4 with the respective scatter graphs shown in Fig. 4.10. As the deposition temperature increases, so does μ_{sat} and the electron concentration due to the higher conductivity of the MgZnO film. However, for deposition temperatures above 200 °C, μ_{sat} begins to degrade, presumably due to a reduction in the grain size, although this would require confirmation with XRD measurements. For deposition temperatures greater than 200 °C, the influence of low cycle percentage MgZnO films is reduced and hence a decrease in the *On/Off* ratio and μ_{sat} is observed. Furthermore, the increasing V_T is due to a positive lateral shift in the transfer characteristic, probably as a result of increased activation of the magnesium precursor, resulting in a reduced electron concentration.

Table 4.4 Average TFT parameters for 12.5 % MgZnO TFTs with increasing deposition temperature from 125 to 250 °C, with 5 measurements per temperature

Deposition Temperature (°C)	***On/off* ratio**	**V_T (V)**	**μ_{sat} (cm^2/Vs)**	**Effective *SS* (V/decade)**
125	9.4×10^4	5.1	2.8	1.5
150	1.1×10^5	7.2	3.1	1.6
175	3.3×10^5	7.5	4.3	1.4
200	5.8×10^5	7.1	4.0	1.0
225	2.7×10^4	7.9	3.9	1.6
250	8.1×10^4	8.3	2.7	3.1

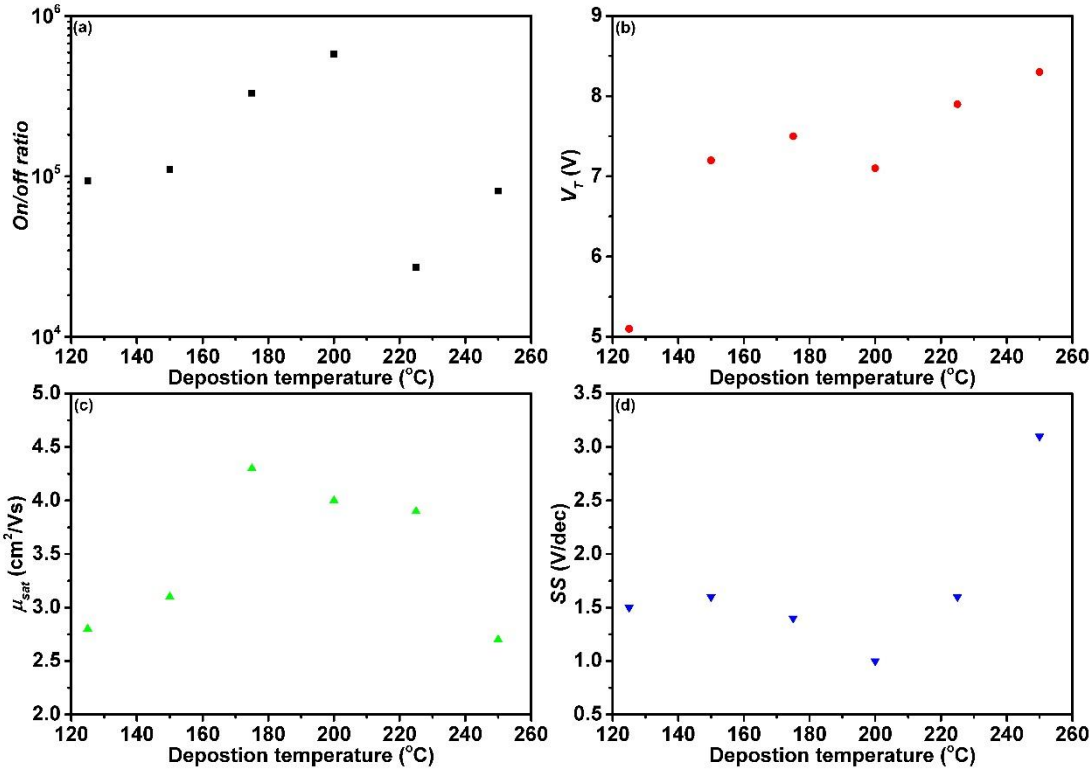

Fig. 4.10 Scatter graphs for the TFT characteristics (a) *On/Off* ratio, (b) V_T, (c) μ_{sat} and (d) the effective *SS* against deposition temperature.

Above, Fig. 4.10 shows that the optimal deposition temperatures for 12.5 % MgZnO TFTs is between 175 and 200 °C. Where the 200 °C deposited film produces a higher *On/Off* ratio and lower V_T and effective *SS*. The effect of isolating each TFT on the electrical characteristics was investigated on 200 °C 12.5 % MgZnO films, which were fabricated using photolithography. The source and drain contacts with an L = 40 µm and W = 400 µm were patterned using a positive resist (Shipley S1813) and developer (DOW Microdev). Aluminium contacts were subsequently evaporated, and unnecessary Al was lifted-off using glacial acetone (Fisher Scientific). The process was repeated to achieve a mesa around each device by wet etching in 1 % acetic acid solution (Fisher Scientific) for 40 s. Fig. 4.11(a) and (b) show the output and transfer characteristics respectively of the patterned MgZnO TFT.

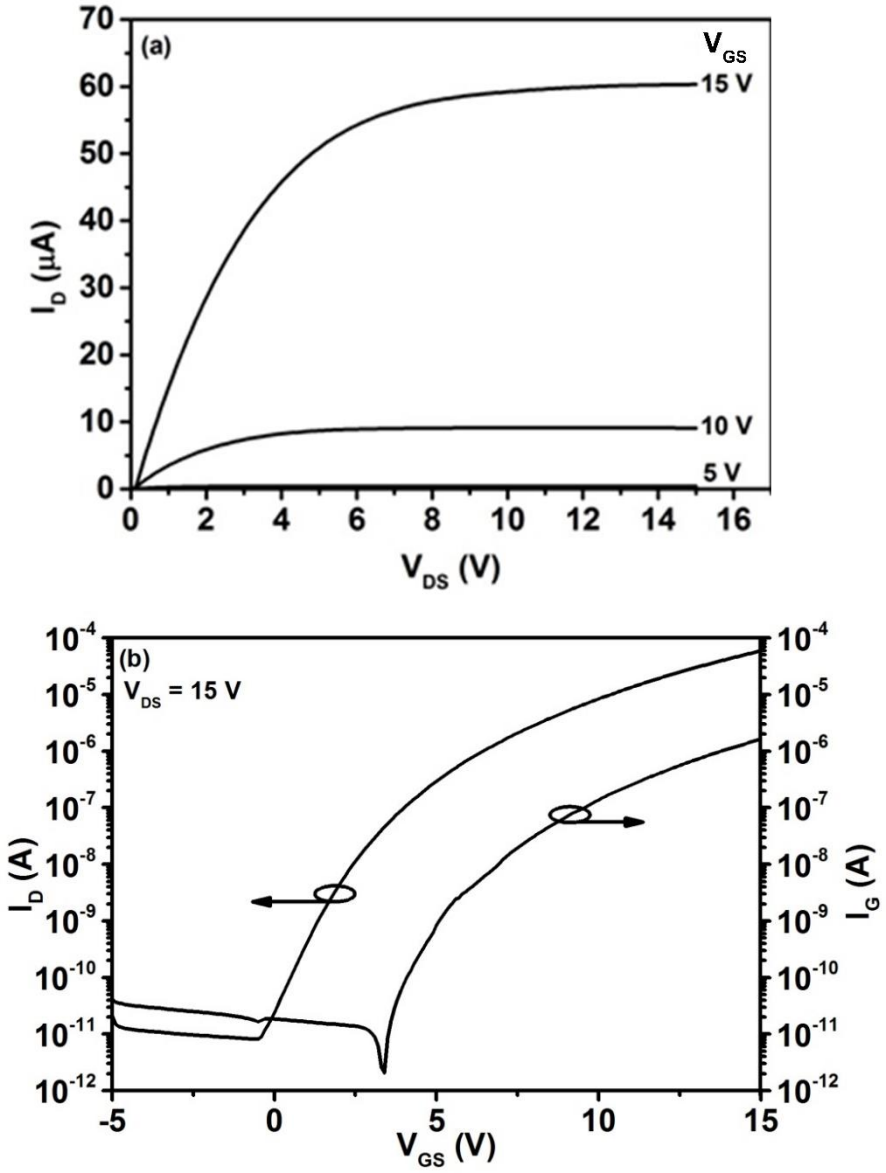

Fig. 4.11 (a) output and (b) transfer characteristics with gate leakage shown of 12.5 % MgZnO TFT deposited at 200 °C

The extracted parameters from the characteristics in Fig. 4.11 are: *On/Off* ratio 7×10^6, V_T = 8.1 V, μ_{sat} = 4 cm^2/Vs and the effective *SS* = 0.8 V/dec. By comparing the TFT characteristics of shadow masks and photolithography TFTs (Fig. 4.3 and Fig. 4.11 respectively), it is evident that the TFT parameters are comparable. However, an improvement was observed in the *On/Off* ratio due to the lower off-state current, by an order of magnitude. However, the shadow masked TFTs have a high on current, which is accounted for by a larger aspect ratio. The improvement observed in the effective *SS* for photolithography TFT, may arise from advances in the MgZnO film deposition technique or additional substrate cleaning. However, the additional processing of photolithography should not improve the effective *SS* as the MgZnO is deposited prior to this step. Comparing the output characteristics in Fig. 4.3 (a) and Fig. 4.11 (a), it is evident the effect of the mesa process serves to effectively

isolate the devices. Thus, eliminating the zero-bias leakage observed in the output characteristics of the shadow mask, non-mesa-ed samples. As discussed above, the transfer characteristics in Fig. 4.11(b) demonstrates a reduction in the reverse current bias by 1 order of magnitude at V_{GS} = – 0.2 V (the V_{on} point) and 3 orders of magnitude at V_{GS} = – 5 V is observed. However, there a large gate leakage remains and is shown in Fig. 4.11(b) which is investigated next.

It was shown by Kim *et al*. [38] and Yang *et al*. [39] that Al_2O_3 capping layers on top of SiO_2 can improve the electrical characteristics of ZnO TFTs, due the increased grain size. A study into the influence of the gate oxide was investigated by depositing an interfacial layer of Al_2O_3 using ALD, prior to the MgZnO film. The Al_2O_3 was deposited at 200 ^oC with increasing thicknesses of 5, 10 and 20 nm, confirmed by ellipsometry. Without breaking the chamber vacuum, the MgZnO was deposited at 200 ^oC with an Mg cycle percentage of 12.5 %. TFT characteristics for the increasing Al_2O_3 thickness are shown in Fig. 4.12 and the average of 6 devices is shown with the respective variance for each parameter. In addition to the TFT characteristics, the effect of hysteresis on the threshold voltage (ΔV_T) for increasing Al_2O_3 thickness is examined, from low-high potential and high-low potential. The best output and transfer characteristics for each Al_2O_3 are shown in Fig. 4.12(a) and (b) respectively.

Table 4.5 The effect of Al_2O_3 thickness on the TFT characteristics (V_T, μ_{sat}, the effective *SS* and ΔV_T) on 12.5 % MgZnO layers deposited at 200 ^oC. With the average of 5 devices per Al_2O_3 thickness and 1 standard deviation given as the error.

Al_2O_3 Thickness (nm)	***On/off* ratio**	**V_T (V)**	**μ_{sat} (cm^2/Vs)**	**Effective *SS* (V/decade)**	**ΔV_T (mV)**
5	$5.4 \times 10^8 \pm 3$	13.7 ± 0.26	7.3 ± 0.46	1.3 ± 0.07	134 ± 5
10	$8.6 \times 10^8 \pm 2.9$	13.9 ± 0.19	8.5 ± 0.25	1.1 ± 0.08	61 ± 16
20	$1.6 \times 10^9 \pm 0.3$	14.7 ± 0.19	8.8 ± 0.18	0.9 ± 0.07	72 ± 2.8

It is evident that in Fig. 4.11 and Fig. 4.12(b), a thicker Al_2O_3 interfacial layer improves the *On/Off* ratio by reducing the off-current by an order of magnitude, although for thicknesses greater than 10 nm there is a negligible effect on the *On/Off* ratio. Similarly, the average μ_{sat} improves with increasing Al_2O_3 thickness as a result of increased on-current, with a maximum of 9.1 cm^2/Vs. However, an undesired increase in V_T is observed due to the lateral shift in the transfer characteristics in the positive direction; this can be observed by comparing Fig. 4.11(b) and Fig. 4.12(b). A small degradation in the effective *SS* is observed for the 5 nm Al_2O_3, however for thicker Al_2O_3 layers there is a slight improvement in the effective *SS*. The associated improvement in the TFT characteristics with an Al_2O_3 capping layer has been associated to the improved crystal orientation in the (002) direction [39]. However, further

XRD measurements on these films, with the gate oxide below, is required to confirm this phenomenon. Furthermore, the Al_2O_3 serves to dramatically reduce the gate leakage in these TFTs as shown by the inset in Fig. 4.12(b). With the addition of Al_2O_3 the maximum gate leakage current $I_G \approx 10^{-10}$ A, four orders of magnitude lower than bare SiO_2.It is believed that the Zn adversely interacts with the SiO_2, introducing defects which greatly increase the oxide leakage current. However, further characterisation of the MgZnO/SiO_2 interface i s required to determine if the diffusion of Zn in to the oxide is observed.

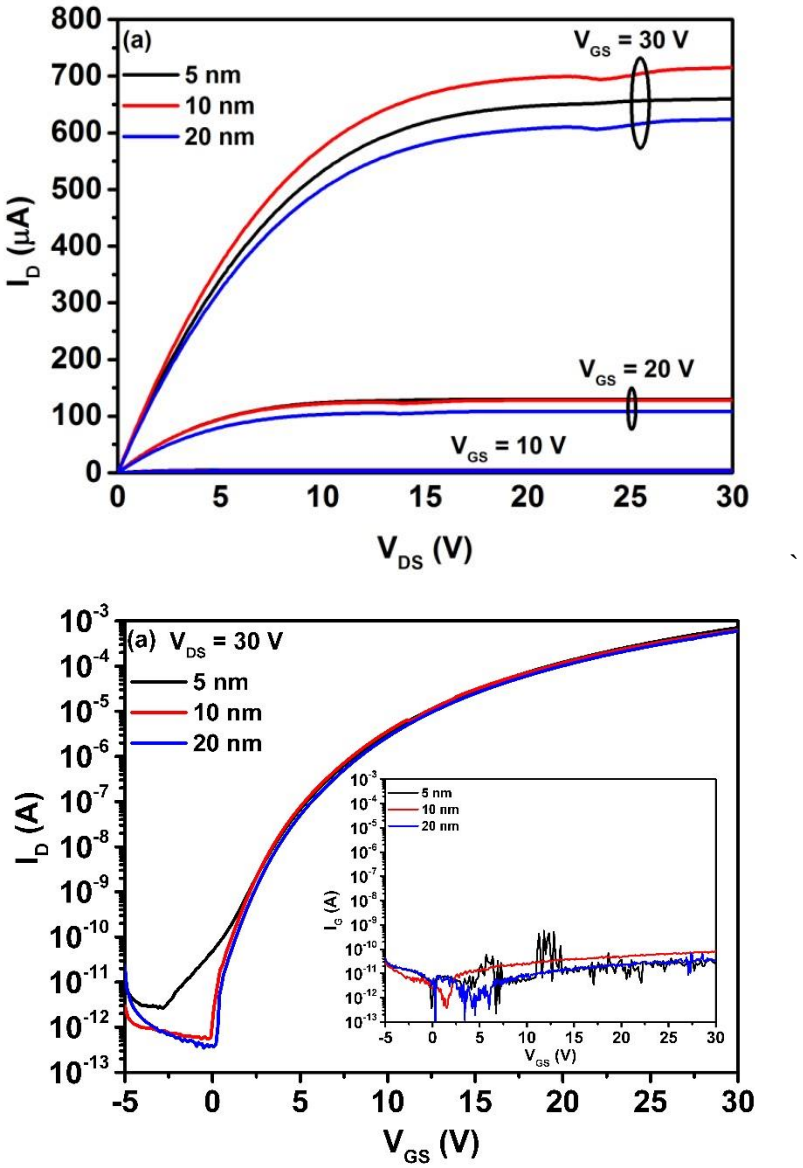

Fig. 4.12 Effect of the thickness of Al_2O_3 capping layer for 12.5 % MgZnO (a) output and (b) transfer characteristics (inset) showing the gate leakage (I_G) with for increasing Al_2O_3 thickness. The I_G for the TFT without Al_2O_3 as shown in Fig. 4.11 for comparison

As shown in Table 4.5, ΔV_T is 61 and 72 mV for the 10 and 20 nm capping layer devices with a standard deviation of 16 and 2.8 mV respectively. By comparison, TFTs without the Al_2O_3 capping layer, ΔV_T = 67 mV with a standard deviation of 16 mV. Hence no degradation to the

hysteresis is observed in the transfer characteristics for TFTs with Al_2O_3 capping layers of 10 and 20 nm. Furthermore, C-V measurements performed on the substrate structure (10 nm $Al_2O_3/SiO_2/Si$) with Al ohmic contacts thermally deposited (structure shown in Fig. 4.13 inset), exhibited no measurable hysteresis as shown in Fig. 4.13 over a frequency range of 0.1 – 100 kHz.

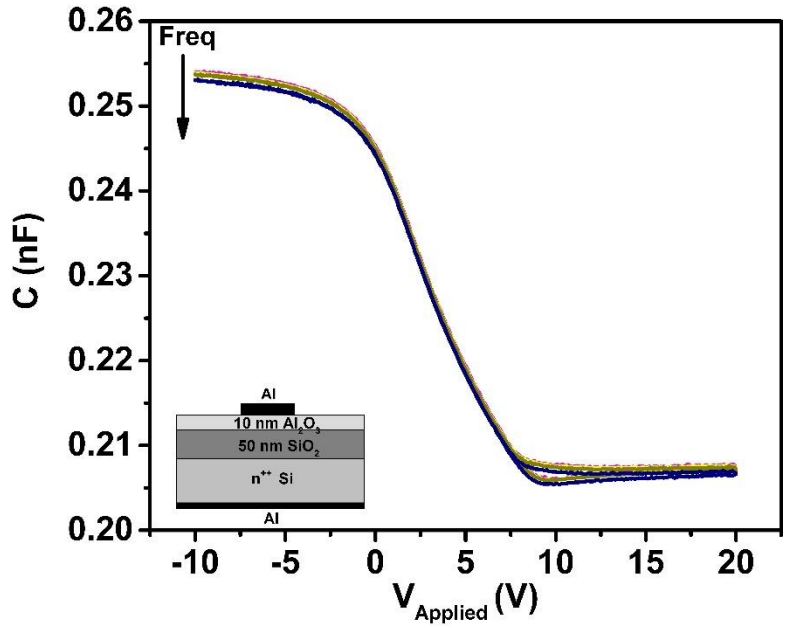

Fig. 4.13 Lack of hysteresis for the substrate-film capacitance for 10 nm Al_2O_3 at the following frequencies: 1 kHz, 10 kHz and 100 kHz

4.6. Fitting of MgZnO TFT characteristics with the multi-trapping and release model

It is apparent in the transfer characteristics shown in Fig. 4.11 and Fig. 4.12, that there is no distinct sub-threshold and above threshold regions. Instead the characteristics are subject to a power law dependency across the full range of gate voltage. Hence, more appropriate physics based *I-V* models are considered to further understand the conduction mechanisms within the TFTs. A number of models are compared in section 3.4.1.2 where the adopted method is by Torricelli *et al.*[40] which focuses on the effect of the multi-trapping-and-release of carriers within the DOS. It is assumed that ZnO DOS can be described by two Gaussian distributions for so-called deep and tail states as identified in Fig. 3.7. Furthermore, it is demonstrated in [40] that the Gaussian distributions can be approximated to a two-term exponential term for the range of energies most populated by carriers as shown by Eqn. (3.11).

The *I-V* characteristics for the MTR model is described in Eqns. (3.22) and (3.23). Fitting of the transfer and output characteristics were performed by linear regression using an in-house MATLAB program and the degree of fitness was established from the regression coefficient,

R^2. Fittings performed on 12.5 % MgZnO TFTs deposited at 200 °C shown in Fig. 4.11 and the best fit is given in Fig. 4.14. Regression coefficients of 0.99 and 0.98 were obtained for the transfer and output characteristics respectively. The extracted fitting parameters for the MTR model given in Eqn. (3.18) are V_{FB} = − 1.0 V, γ = 5.05, β = 1.55 × 10^{-12} A/V$^{\gamma}$ and R_{DS} = 160 Ω. Moreover, V_{FB} is with good agreement with the surface V_{FB} calculated from XPS/IPES measurements in Fig. 4.9 and V_{on}.

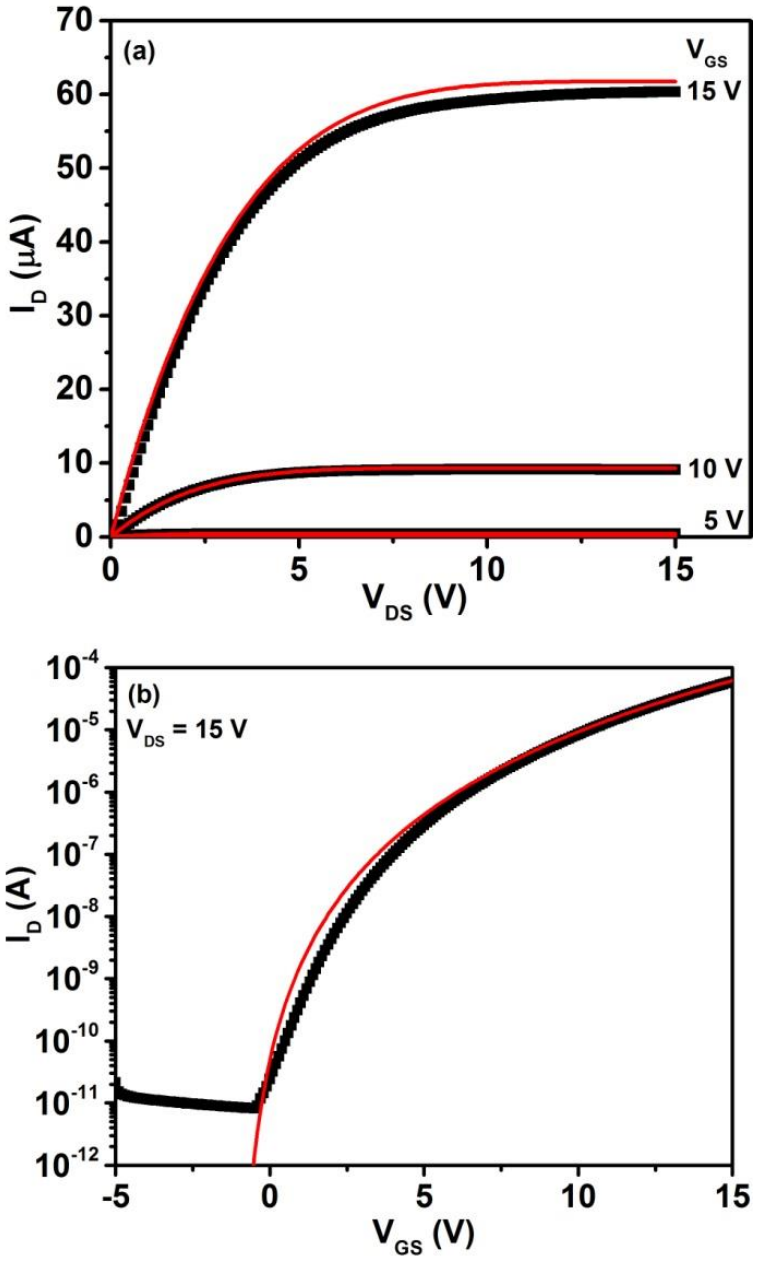

Fig. 4.14 (a) Output and (b) transfer characteristics of 12.5 % MgZnO TFT shown in Fig. 4.11 with fittings of the MTR model in Eqn.(3.18) shown as solid lines and the symbols is the measured data

By comparison with the extracted parameters from Torricelli *et al*. [40], which used sol-gel deposited ZnO, T_o = 710 K and N_t = 2 × 10^{19} cm^{-3} are obtained. However, the fitted MgZnO

TFT in Fig. 4.14 gives T_o = 758 K and N_t = 5.4 × 10^{19} cm^{-3} indicating a slightly higher density of traps. Although the fitted MgZnO TFT suffers from a higher T_o, this parameter is a combination of the interface and the tail states although it should be noted that the accumulation of the interface implies that the interface states will be full and thus screened. In order to extract the full DOS distribution (tail and deep states), capacitance voltage measurements are required, which are outlined in chapter 5. Unfortunately, it proved impossible to obtain good CV plots on MgZnO material. Fittings were also applied to the MgZnO TFT with a 20 nm Al_2O_3 capping layer and are shown in Fig. 4.12, where T_o = 670 K and N_t = 2 × 10^{19} cm^{-3}. The lower T_o correlates with the improved effective *SS* achieved by the Al_2O_3 capping layer. Moreover, variation between N_t for the TFT with and without the Al_2O_3 capping layer can be accounted for by slight differences in deposition conditions.

4.7. Conclusion

The effect of magnesium doping of ZnO films on the electrical and physical properties of ZnO material and TFTs has been investigated. The alloying process was controlled by increasing the deposition cycle percentages for the Mg precursor. Analysis of the structural properties from XRD measurements determined that the grain size remains constant (~ 20 nm) for different Mg cycle percentages. However, growth in the c-axis (002) diminishes for increasing Mg content. From ellipsometry and PL measurements, Mg doping increases the band gap which can be explained by the Burstein-Moss effect. PL measurements indicated that annealing the MgZnO film in air at 300 ^oC caused a further blue shift in the near band emission which is ascribed to activation of the magnesium dopant. From XPS measurements for as-deposited 12.5 % MgZnO, the Mg 2p CL spectra revealed species which are associated with Mg-O bonding. Furthermore, in the O 1s CL spectra, the relative area for the sub-peak associated with oxygen atoms in the vicinity of an oxygen vacancy reduces from 32 to 13 % for the 12.5 % MgZnO film. A combination of effects give rise to a reduction in the conductivity due to Mg alloying. The group II elements Mg and Cd form solid solutions with Zn, that is, they replace the Zn within the lattice. This gives rise to a potential range of bandgaps from about 2 eV to 8 eV. The energy-gap of $Mg_xZn_{1-x}O$ is given by [35]:

$$E_g(x) = (1 - x)\, E_{ZnO} + xE_{MgO} - bx\,(1 - x),$$

where b is the bowing parameter, E_{MgO} and E_{ZnO} are the bandgaps of MgO and ZnO, respectively. The bowing parameter, b, depends on the difference in ability of ZnO and MgO to attract electrons; that is, it is related to the electronegativities of the end binary species. The incorporation of Mg into ZnO has been proposed to facilitate the formation of the acceptor-like vacancy defects such as V_{Zn},[35]. The reduced conductivity is predominantly

attributed to the increased concentration of V_{Zn}, leading to the reduced free electron concentration. The formation of intrinsic V_{Zn} defects has been reported to decrease as Mg content (x) increases [34], causing the compensation ratio to increase from 0.23 (at $x = 0$) to 0.47 at ($x = 0.29$), which is similar to the $Mg_xZn_{1-x}O$ compositions examined in this work.

Electrical measurements of TFTs with small Mg cycle percentages showed characteristics significantly improving in terms of *On/Off* ratio, μ_{sat} and the effective *SS*. However, for cycle percentages above 12.5 %, the performance metrics begin to degrade. Moreover, increasing the Mg content serves to increase the effective threshold voltage, although as the characteristics do not follow a square power law the definition of the threshold voltage is somewhat ambiguous. Optimum deposition temperature for 12.5 % MgZnO was established between 175 and 200 ^oC. The effect of an Al_2O_3 capping layer with different thicknesses was also investigated. The *On/Off* ratio was increased > 10^8 and average $\mu_{sat} \approx 8$ cm^2/Vs for Al_2O_3 thicknesses of 10 and 20 nm. Finally fitting of the drain current using a physics-based model based on the multi-trapping and release of carriers in the sub-band gap DOS was carried out. It was determined that good fits to experimental characteristics could be obtained with power dependencies for the transfer characteristics of 5 and 4.5 with and without an Al_2O_3 capping layer respectively. This highlights that the use of standard parameter extraction with the MOSFET equation is not valid at least for these samples, although it provides for easy comparison of technologies and is widely adopted in the literature. The power dependency is directly related to the distribution of the sub-band gap traps and interface properties (*SS* and interface states). The reduction in the power index for Al_2O_3 capped samples is attributed to the improved interface properties namely *SS*.

4.8. References

[1] K. Semyung, B. Seokhwan, L. Seungjun, J. Sunyeol, J. Wooho, K. Hyungchul, G. Su Cheol, C. Ho Jung, P. Hyung-ho, and J. Hyeongtag, "Characteristics of the ZnO thin film transistor by atomic layer deposition at various temperatures," *Semiconductor Science and Technology*, vol. 24, no. 3, p. 035015, 2009.

[2] S. J. Lim, S. J. Kwon, H. Kim, and J. S. Park, "High performance thin film transistor with low temperature atomic layer deposition nitrogen-doped ZnO," *Applied Physics Letters*, vol. 91, no. 18, p. 183517, 2007.

[3] E. Guziewicz, I. A. Kowalik, M. Godlewski, K. Kopalko, V. Osinniy, A. Wójcik, S. Yatsunenko, E. Łusakowska, W. Paszkowicz, and M. Guziewicz, "Extremely low temperature growth of ZnO by atomic layer deposition," *Journal of Applied Physics*, vol. 103, no. 3, p. 033515, 2008.

[4] J. Z. Chen, C. H. Li, and I. C. Cheng, "Phase transitions of room temperature RF-sputtered ZnO/Mg0.4Zn0.6O multilayer thin films after thermal annealing," *Thin Solid Films*, vol. 520, no. 6, pp. 1918-1923, 2012.

[5] H. A. Chin, I. C. Cheng, C. I. Huang, Y. R. Wu, W. S. Lu, W. L. Lee, J. Z. Chen, K. C. Chiu, and T. S. Lin, "Two dimensional electron gases in polycrystalline MgZnO/ZnO heterostructures grown by rf-sputtering process," *Journal of Applied Physics*, vol. 108, no. 5, p. 054503, 2010.

[6] Y. Y. Kim, C. H. An, H. K. Cho, J. H. Kim, H. S. Lee, E. S. Jung, and H. S. Kim, "High-temperature growth and in-situ annealing of MgZnO thin films by RF sputtering," *Thin Solid Films*, vol. 516, no. 16, pp. 5602-5606, 2008.

[7] Y. S. Tsai and J. Z. Chen, "Positive Gate-Bias Temperature Stability of RF-Sputtered $Mg_{0.05}Zn_{0.95}O$ Active-Layer Thin-Film Transistors," *IEEE Transactions on Electron Devices*, vol. 59, no. 1, pp. 151-158, 2012.

[8] C. H. Li, Y. S. Tsai, and J. Z. Chen, "Negative bias temperature instability of Rf-sputtered $Mg_{0.05}Zn_{0.95}O$ thin film transistors with MgO gate dielectrics," *Semiconductor Science and Technology*, vol. 26, no. 10, p. 105007, 2011.

[9] J. H. Lee, C. H. Kim, H. S. Kim, N. W. Jang, Y. Yun, L. M. Do, and K. H. Baek, "Effects of Mg incorporation by co-sputtering into the ZnO channel layer of thin-film transistors," *Journal of the Korean Physical Society*, vol. 62, no. 6, pp. 937-941, 2013.

[10] C. H. Tsai, Y. S. Li, I. C. Cheng, and J. Z. Chen, "O_2/HMDSO-Plasma-Deposited Organic–Inorganic Hybrid Film for Gate Dielectric of MgZnO Thin-Film Transistor," *Plasma Processes and Polymers*, vol. 11, no. 1, pp. 89-95, 2014.

[11] T. Törndahl, C. Platzer-Björkman, J. Kessler, and M. Edoff, "Atomic layer deposition of $Zn_{1-x}Mg_xO$ buffer layers for Cu(In,Ga)Se_2 solar cells," *Progress in Photovoltaics: Research and Applications*, vol. 15, no. 3, pp. 225-235, 2007.

[12] H. Y. Lee, Y. C. Lin, M. J. Lee, W. Y. Uen, and K. Sreenivas, "Enhanced Performance of $Mg_{0.1}Zn_{0.9}O$ UV Photodetectors Using Photoelectrochemical Treatment and Silica Nanospheres," *Journal of Nanomaterials*, vol. 2014, p. 6, 2014, Art. no. 972869.

[13] L. K. Wang, Z. G. Ju, C. X. Shan, J. Zheng, B. H. Li, Z. Z. Zhang, B. Yao, D. X. Zhao, D. Z. Shen, and J. Y. Zhang, "Epitaxial growth of high quality cubic MgZnO films on MgO substrate," *Journal of Crystal Growth*, vol. 312, no. 7, pp. 875-877, 2010.

[14] C. Y. Zhao, X. H. Wang, J. Y. Zhang, Z. G. Ju, C. X. Shan, B. Yao, D. X. Zhao, D. Z. Shen, and X. W. Fan, "Ultraviolet photodetector fabricated from metal-organic chemical vapor deposited MgZnO," *Thin Solid Films*, vol. 519, no. 6, pp. 1976-1979, 2011.

[15] S. Ito, M. Sumiya, M. Mieno, and H. Koinuma, "Growth of $Mg_xZn_{1-x}O$ film by MOCVD equipped laser heating system," *Materials Science and Engineering*: *B*, vol. 173, pp. 11-13, 2010.

[16] H. Asahara, D. Takamizu, A. Inokuchi, M. Hirayama, A. Teramoto, S. Saito, M. Takahashi, and T. Ohmi, "Characterization of MgZnO films grown by plasma enhanced metal-organic chemical vapor deposition," *Thin Solid Films*, vol. 518, no. 11, pp. 2953-2956, 2010.

[17] D. C. Kim, B. H. Kong, C. H. Ahn, and H. K. Cho, "Characteristics improvement of metalorganic chemical vapor deposition grown MgZnO films by MgO buffer layers," *Thin Solid Films*, vol. 518, no. 4, pp. 1185-1189, 2009.

[18] K. Remashan, Y. S. Choi, S. J. Park, and J. H. Jang, "High Performance MOCVD-Grown ZnO Thin-Film Transistor with a Thin MgZnO Layer at Channel/Gate Insulator Interface," *Journal of The Electrochemical Society*, vol. 157, no. 12, pp. H1121-H1126, 2010.

[19] C. J. Ku, P. Reyes, Z. Duan, W. C. Hong, R. Li, and Y. Lu, "MgxZn1−xO Thin-Film Transistor-Based UV Photodetectorwith Enhanced Photoresponse," *Journal of Electronic Materials*, journal article vol. 44, no. 10, pp. 3471-3476, 2015.

[20] C. J. Ku, Z. Duan, P. I. Reyes, Y. Lu, Y. Xu, C. L. Hsueh, and E. Garfunkel, "Effects of Mg on the electrical characteristics and thermal stability of $Mg_xZn_{1-x}O$ thin film transistors," *Applied Physics Letters*, vol. 98, no. 12, p. 123511, 2011.

[21] T. H. Kim, J. J. Park, S. H. Nam, H. S. Park, N. R. Cheong, J. K. Song, and S. M. Park, "Fabrication of Mg-doped ZnO thin films by laser ablation of Zn:Mg target," *Applied Surface Science*, vol. 255, no. 10, pp. 5264-5266, 2009.

[22] A. L. Patterson, "The Scherrer Formula for X-Ray Particle Size Determination," *Physical Review*, vol. 56, no. 10, pp. 978-982, 1939.

[23] Z. H. Li, E. S. Cho, and S. J. Kwon, "Mg-doped ZnO thin films deposited by the atomic layer chemical vapor deposition for the buffer layer of CIGS solar cell," *Applied Surface Science*, vol. 314, pp. 97-103, 2014.

[24] L. Gao and J. M. Zhang, "Photoluminescence of diluted Mg doped ZnO thin films and band-gap change mechanisms," *Wuli Xuebao/Acta Physica Sinica*, vol. 59, no. 2, pp. 1263-1267, 2010.

[25] C. Y. Liu, H. Y. Xu, L. Wang, X. H. Li, and Y. C. Liu, "Pulsed laser deposition of high Mg-content MgZnO films: Effects of substrate temperature and oxygen pressure," *Journal of Applied Physics*, vol. 106, no. 7, p. 073518, 2009.

[26] M. Grundmann, "Optical Properties," in *The Physics of Semiconductors*: An Introduction Including Nanophysics and Applications 1st ed. Heidelberger, Berlin: Springer Berlin Heidelberger, 2010, pp. 265-307.

[27] V. Etacheri, R. Roshan, and V. Kumar, "Mg-Doped ZnO Nanoparticles for Efficient Sunlight-Driven Photocatalysis," *ACS Applied Materials & Interfaces*, vol. 4, no. 5, pp. 2717-2725, 2012.

[28] J. Liang, H. Z. Wu, Y. F. Lao, N. B. Chen, P. Yu, and T. N. Xu, "Characterization of cubic phase MgZnO/Si(100) interfaces," *Applied Surface Science*, vol. 252, no. 4, pp. 1147-1152, 2005.

[29] L. Su, Z. Yuan, Z. Quanlin, C. Mingming, J. Xu, W. Tianzhun, G. Xuchun, P. Bicai, X. Rong, and T. Zikang, "Solar-blind wurtzite MgZnO alloy films stabilized by Be doping," *Journal of Physics D: Applied Physics*, vol. 46, no. 24, p. 245103, 2013.

[30] V. I. Nefedov, M. N. Firsov, and I. S. Shaplygin, "Electronic structures of $MRhO_2$, MRh_2O_4, $RhMO_4$ and Rh_2MO_6 on the basis of X-ray spectroscopy and ESCA data," *Journal of Electron Spectroscopy and Related Phenomena*, vol. 26, no. 1, pp. 65-78, 1982.

[31] S. S. Hullavarad, N. V. Hullavarad, D. E. Pugel, S. Dhar, T. Venkatesan, and R. D. Vispute, "Structural and chemical analysis of pulsed laser deposited $Mg_xZn_{1-x}O$ hexagonal (x = 0.15, 0.28) and cubic (x = 0.85) thin films," *Optical Materials*, vol. 30, no. 6, pp. 993-1000, 2008.

[32] M. K. Bahl, "ESCA studies of some niobium compounds," *Journal of Physics and Chemistry of Solids*, vol. 36, no. 6, pp. 485-491, 1975.

[33] J. G. Song, J. Park, J. Yoon, H. Woo, K. Ko, T. Lee, S. H. Hwang, J. M. Myoung, K. Kim, Y. Jang, K. Kim, and H. Kim, "Plasma enhanced atomic layer deposition of magnesium oxide as a passivation layer for enhanced photoluminescence of ZnO nanowires," *Journal of Luminescence*, vol. 145, pp. 307-311, 2014.

[34] J.-F. Chien, H.-Y. Shih, H.-Y. Liao, R.-M. Lin, J.-J. Shyue, and M.-J. Chen, "P-type Conductivity of MgZnO:(N:Ga) Thin Films Prepared by Remote Plasma In-Situ Atomic Layer Doping," *ECS Journal of Solid State Science and Technology*, vol. 2, no. 11, pp. R249-R253, 2013.

[35] L. Lishu, M. Zengxia, T. Aihua, L. Huili, and D. Xiaolong, "Self-compensation induced high-resistivity in MgZnO," *Journal of Physics D: Applied Physics*, vol. 50, no. 6, p. 065102, 2017.

[36] E. A. Kraut, R. W. Grant, J. R. Waldrop, and S. P. Kowalczyk, "Semiconductor core-level to valence-band maximum binding-energy differences: Precise determination by x-ray photoelectron spectroscopy," *Physical Review B*, vol. 28, no. 4, pp. 1965-1977, 1983.

[37] J. Robertson, "Band offsets of wide-band-gap oxides and implications for future electronic devices," *Journal of Vacuum Science & Technology B: Microelectronics and Nanometer Structures Processing, Measurement, and Phenomena*, vol. 18, no. 3, pp. 1785-1791, 2000.

[38] S.-H. Kim, J. Kwang. Seok, Y. Ho. Jin, Y. Seung. Dong, K. Yu. Mi, K. Jin. Seop, K. Young. Uk, A. Jin. Un, L. Hi. Deok, and L. Ga. Won, "Channel engineering of ZnO-based thin film transistors using Al2O3 interlayer grown by atomic layer deposition," *Japanese Journal of Applied Physics*, vol. 53, no. 9, p. 091101, 2014.

[39] J. Yang, J. K. Park, S. Kim, W. Choi, S. Lee, and H. Kim, "Atomic-layer-deposited ZnO thin-film transistors with various gate dielectrics," *physica status solidi (a)*, vol. 209, no. 10, pp. 2087-2090, 2012.

[40] F. Torricelli, J. R. Meijboom, E. Smits, A. K. Tripathi, M. Ferroni, S. Federici, G. H. Gelinck, L. Colalongo, Z. M. Kovacs-Vajna, D. d. Leeuw, and E. Cantatore, "Transport Physics and Device Modeling of Zinc Oxide Thin-Film Transistors Part I: Long-Channel Devices," *IEEE Transactions on Electron Devices*, vol. 58, no. 8, pp. 2610-2619, 2011.

Chapter 5

5. Niobium doped zinc oxide thin-film transistors

5.1. Introduction

Research into zinc oxide (ZnO) based materials for the active layers in thin-film transistors (TFTs) in flat panel displays, has extensively focused on indium-gallium-zinc oxide (IGZO). Namely for superior saturation electron mobility (μ_{sat}) and electrical stability due to the indium and gallium dopants respectively [1-6]. Sputtered IGZO TFTs commonly achieve μ_{sat} > 15 cm^2/Vs [1, 4-7], enabling the potential for ultra-high definition pixel displays with driver circuitry integrated onto the panel. However, long term implementation of indium-based films can hinder low cost production, due to the potential volatility in the cost of indium ore [8]; hence the motivation for non-indium based ZnO. Alternative doped ZnO films have been proposed with varying degrees of success such as magnesium (Mg) [9], as considered in Chapter 4, gallium (Ga) [10] and silicon (Si) [11]. Typically, Si and Ga doped ZnO films suffer from low mobility, μ_{sat} ~1 cm^2/Vs whilst achieving low off-currents [10, 11], resulting in the need for research into alternative dopants. Mg doped ZnO films have the potential to achieve higher mobilities, however as demonstrated here, suffer from high subthreshold swing due to the nature of the disorder within the film.

Niobium offers the prospect of effectively reducing the disorder within the films, namely the oxygen vacancies (V_o). ZnO inherently suffers from two defects V_o and Zn interstitials (Zn_i). The use of substitutional dopants such as Mg, Ga and Si, help to reduce the effect of Zn_i because of the lower concentration of Zn ions in the structure. Although the oxidation states of Si^{4+} and Ga^{3+} are higher than that of Zn^{2+} and provide the possibility of reducing the number of V_o, niobium exists in the higher oxidation state of Nb^{5+}, potentially further suppressing V_o.

To date, Nb doped ZnO studies have focused on the optical, structural and conductivity properties. Thin films have been deposited by pulse layer deposition (PLD) [12, 13], RF sputtering [14] and spray pyrolysis [15, 16]. It has been shown that by increasing the Nb content within the ZnO matrix, the band gap shifts to higher energies, but the films move from a small grain polycrystalline state towards the amorphous state [12, 13, 16]. Shao *et al.* [13] demonstrated that the resistivity of ZnO decreased for low Nb concentrations, however, at higher concentrations the films became more resistive. This can be associated with the increased distortion in the polycrystalline structure. Lin *et al.* [12] showed that the Hall mobility can be enhanced by increasing the deposition temperature up to 300 ^oC. However, in the literature to date, no studies have focused on Nb doped ZnO TFTs; the only niobium doped metal oxide films being titanium oxide (TiO_x) [17]. For that system, the effect of Nb doping

improved the on-current without degradation of the off-current; hence improving the μ_{sat} to a value of 0.16 cm^2/Vs, which is still too low for the intended application.

In this chapter, atomic layer deposition (ALD) is used to deposit the Nb doped ZnO (NbZnO) film for TFT applications. Both Nb concentration and deposition temperature was studied in order to establish the optimum TFT characteristics. The best layers are found to be 3.8 % NbZnO with μ_{sat} = 8 cm^2/Vs. Moreover, the effect of Nb on the ZnO optical, structural and compositional properties is presented.

5.2. Experimental details

The following NbZnO films were deposited by the functional materials group at the University of Liverpool. NbZnO films were deposited by ALD using a Cambridge reactor, onto highly doped n-type Si substrates with 50 nm thermally oxidised SiO_2 (Si Mat). Prior to deposition of the NbZnO film, a thin (10 nm) aluminium oxide (Al_2O_3) capping layer was deposited at 200 ^oC to improve the interface between the gate oxide and active layer [18, 19]. The NbZnO film was then deposited using the precursors diethlyzinc (DEZn) (Strem) and niobium pentaethoxide ($Nb(OEt)_5$) (Strem); where the bubbler temperatures of the precursors entering the chamber were at ambient and 140 ^oC respectively. The deposition temperature and cycle fraction were varied to optimise the films. The deposition temperature varied between 175 ^oC and 225 ^oC due to the activation temperature of the Nb precursor [20] and the cycle fraction of Nb from 1% to 12.5%. The NbZnO films were made by first depositing *x*-cycles of ZnO by successive steps of DEZn and then H_2O vapour on the surface. After the *x*-cycles of ZnO, a single Nb_2O_5 cycle is deposited by successive steps of $Nb(OEt)_5$ and H_2O. The process is repeated until the desired film thickness is reached. For example, a film with a Nb cycle percentage of 2% would be achieved by 49 cycles of DEZn and H_2O (x = 49) followed by 1 cycle of $Nb(OEt)_5$ and H_2O. This equates to a cycle fraction of 0.02 and cycle percentage of 2%, (6 / (294 + 6) × 100 %= 2 %).

As shown in Chapter 4, the use of lithography has been seen to provide greatly improved TFT characteristics particularly in terms of leakage currents, hence only devices produced using this process are considered in this chapter. TFTs were patterned using a two-stage lithography process, using the positive photo-resist Shipley 1813 (Dow). In the first stage source and drain regions were patterned and Al (Kurt J. Lesker) was deposited by thermal evaporation to a thickness approximately 70 nm. The unwanted Al was lifted off using acetone (Fisher Scientific), to leave the source and drain contacts with a width (W) of 400 µm and length (L) of 40 µm. The second stage required mesa etching of the TFTs active area by: defining the area the area using lithography and wet etching of the NbZnO in 1 % acetic acid at room temperature. The etch time varied from 30 to 45 s depending on the Nb cycle fraction, with

all the cycle fractions and corresponding cycle percentages listed in Table 5.1. Cross-section and top views of the TFT device structure are shown in Fig. 5.1.

Table 5.1 Cycle fraction and corresponding cycle percentages investigated in this chapter

Niobium Cycle Fraction (Zn:Nb)	Niobium Cycle Percentage (%)
1:0	0
99:1	1.0
49:1	2.0
33:1	3.0
25:1	3.8
20:1	4.8
14:1	6.7
10:1	9.1
7:1	12.5

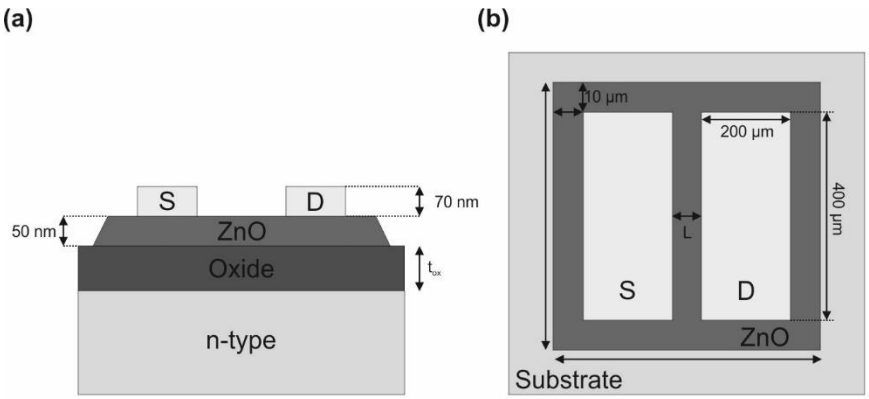

Fig. 5.1 (a) cross-section and (b) top view of the TFT

5.3. Initial electrical characterisation of Nb doped ZnO TFTs

Initial electrical characterisation was conducted using back-gated TFT structures on NbZnO films deposited at 200 °C with cycle percentages between 0 and 3 %. The TFTs were subjected to 1-hour post deposition air anneal at 300 °C. Conventional MOSFET analysis was performed to allow easy comparison of TFTs with those in the literature. Exact parameter extraction details are given in section 3.4.1.1. The *On/Off* ratio, threshold voltage (V_T) and the saturation mobility (μ_{sat}) are given in Table 5.2.

Table 5.2 Initial TFT parameters for 1-hour air annealed at 300 °C NbZnO films were the gate oxide is SiO_2

Cycle Percentage (%)	I_{off} **(A)**	I_{on} **(A)**	***On/Off* ratio**	V_T **(V)**	μ_{sat} **(cm^2/Vs)**
0	9.1×10^{-7}	9.1×10^{-4}	1.0×10^{4}	9.3	1.4
1	2.1×10^{-7}	2.1×10^{-3}	1.0×10^{4}	12.6	6.6
2	3.8×10^{-8}	3.0×10^{-3}	7.9×10^{4}	11.7	6.4
3	3.0×10^{-8}	1.0×10^{-3}	3.3×10^{4}	11.5	3.4

Table 5.2 demonstrates that small cycle percentages serve to increase both the μ_{sat} and the *On/Off* ratio. The increased μ_{sat} can be attributed to higher on current (I_{on}) where 1 % NbZnO achieves the best μ_{sat} = 6.6 cm^2/Vs. As the Nb cycle percentage is further increased, μ_{sat} begins to reduce. The exact cause for the reduction in μ_{sat} will be discussed in section 5.4.2, but is likely to be due to the change in the properties of the material matrix and the presence of percolation current. Furthermore, as the Nb cycle percentage increases, the off-current (I_{off}) reduces. The combination of increasing I_{on} and decreasing I_{off} results in an improved *On/Off* ratio as indicated in Table 5.2,therefore, demonstrating the potential of Nb as a substitutional dopant to enhance TFT performance.

As outlined in section 4.5, it was decided that a 10 nmAl_2O_3 capping layer can substantially improve the electrical characteristics of the NbZnO TFTs. An investigation into the capping layer thickness concluded that an optimal thickness of 10 nm capping layer of Al_2O_3 prior to NbZnO deposition gave the best electrical results. The same deposition conditions used for the 10 nm Al_2O_3 capping layer in chapter 4 are employed in this chapter. The Nb cycle percentages were varied between 3 and 12.5 % and characterised, with the extracted parameters given in Table 5.3 with the corresponding scatter graphs for each parameter in Fig. 5.2.

Table 5.3 Extracted TFT parameters with increasing Nb cycle percentages deposited at 200 °C with a 10 nm Al_2O_3 gate oxide capping layer. The average of 5 devices is given with 1 standard deviation as the error.

Cycle Percentage (%)	*On/Off* ratio (10^8)	V_T (V)	μ_{sat} (cm^2/Vs)	Effective *SS* (V/dec)
3	0.9 ± 0.14	8.9 ± 0.016	8.0 ± 0.67	1.02 ± 0.02
3.8	7.9 ± 0.8	8.2 ± 0.09	7.1 ± 0.07	0.52 ± 0.02
4.8	4.3 ± 1.0	7.7 ± 0.21	4.6 ± 0.05	0.31 ± 0.04
6.7	3.9 ± 0.14	6.7 ± 0.51	1.9 ± 0.01	0.17 ± 0.02
9.1	2.5 ± 0.32	5.3 ± 0.31	0.9 ± 0.009	0.15 ± 0.03
12.5	0.22 ± 0.08	5.4 ± 0.27	0.2 ±0.009	1.35 ± 0.24

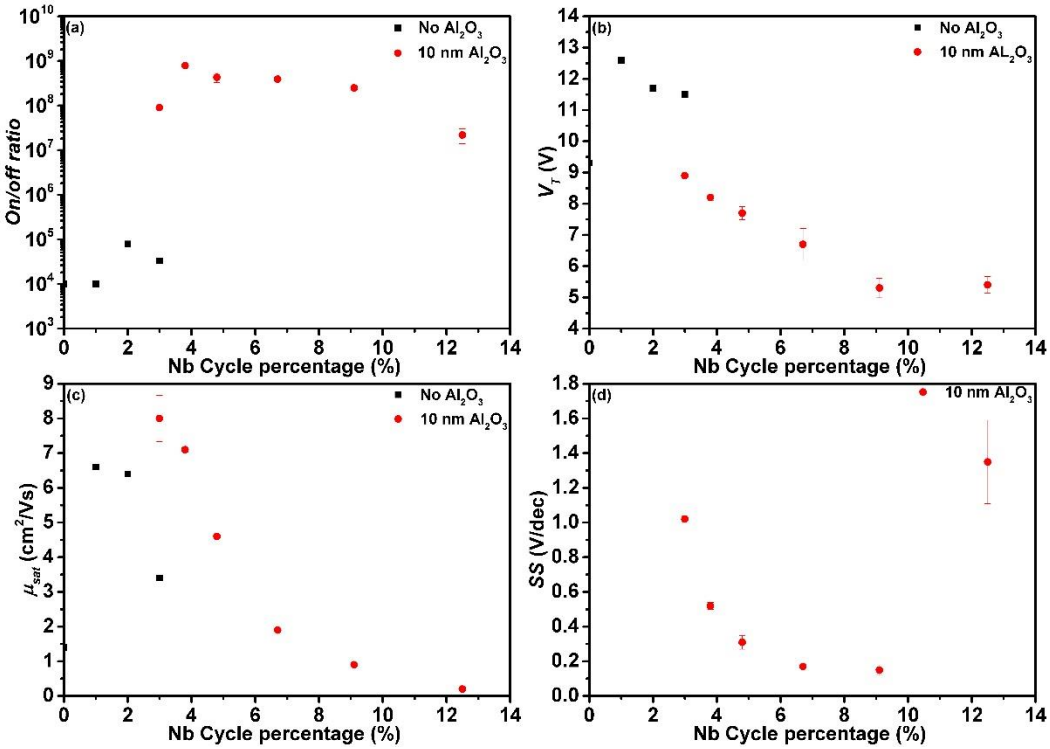

Fig. 5.2 Average scatter plots for the TFT parameters (a) *On/Off ratio*, (b) V_T, (c) μ_{sat} and (d) the effective *SS* for increasing Nb cycle percentages with the 10 nm Al_2O_3 capping layer. Comparison for TFTs without the Al_2O_3 is given in (a) – (c)

By comparison of the 3 % NbZnO in Table 5.2, Fig. 5.2 and Table 5.3, the effect of the Al_2O_3 capping layer is evident from the significant improvement in the TFT parameters, namely the *On/Off* ratio and μ_{sat}. High On/Off ratios are achieved for all cycle percentages, with tight distributions, as shown in Fig. 5.2(a). As the Nb cycle percentages increase, it is evident that μ_{sat} reduces significantly from 8 to 0.2 cm^2/Vs as indicated in both Table 5.3 and Fig. 5.2(c). It is believed that the initial increase in μ_{sat} is associated with the high valency of niobium. As niobium can exist in a 5+ oxidation state, the associated high valent electrons have a lower probability of being scattered, resulting in an increase in μ_{sat}. Therefore, under a sufficiently high V_{GS}, percolation current is known to exist. The same effect is seen in IGZO TFTs and is caused by the presence of indium within the structure [1, 21-23]. The determination of the

onset of percolation current will be discussed in section 5.5.3. As the Nb cycle percentage is further increased, μ_{sat} decreases, and this can be explained by increased grain boundary scattering and will be discussed in section 5.4.2. The V_T remains high for all TFTs in Table 5.3 and Fig. 5.2(b), but this parameter is somewhat ambiguous as these TFTs do not strictly follow a square power dependency. Moreover, the effective *SS* initially improves as indicated by Fig. 5.2(d) until the Nb cycle percentages exceed 9.1 %. The improvement in effective *SS* is indicative of fewer interface states. However, the situation may be more complex as the effect of the sub-band gap DOS on effective SS should not be ignored, as discussed in chapter 4.

From Table 5.3 it is evident that 3.8 % NbZnO provides the best TFT characteristics across all the parameters, with a high *On/Off* ratio, μ_{sat} and relatively low effective *SS*. Moreover, 3.8 % NbZnO demonstrates tight distributions for all parameters. Typical output and transfer characteristics for the 3.8 % NbZnO are shown in Fig. 5.3. Fig. 5.3(a) demonstrates that the output characteristics are fully saturated for all gate voltages, V_{GS}.

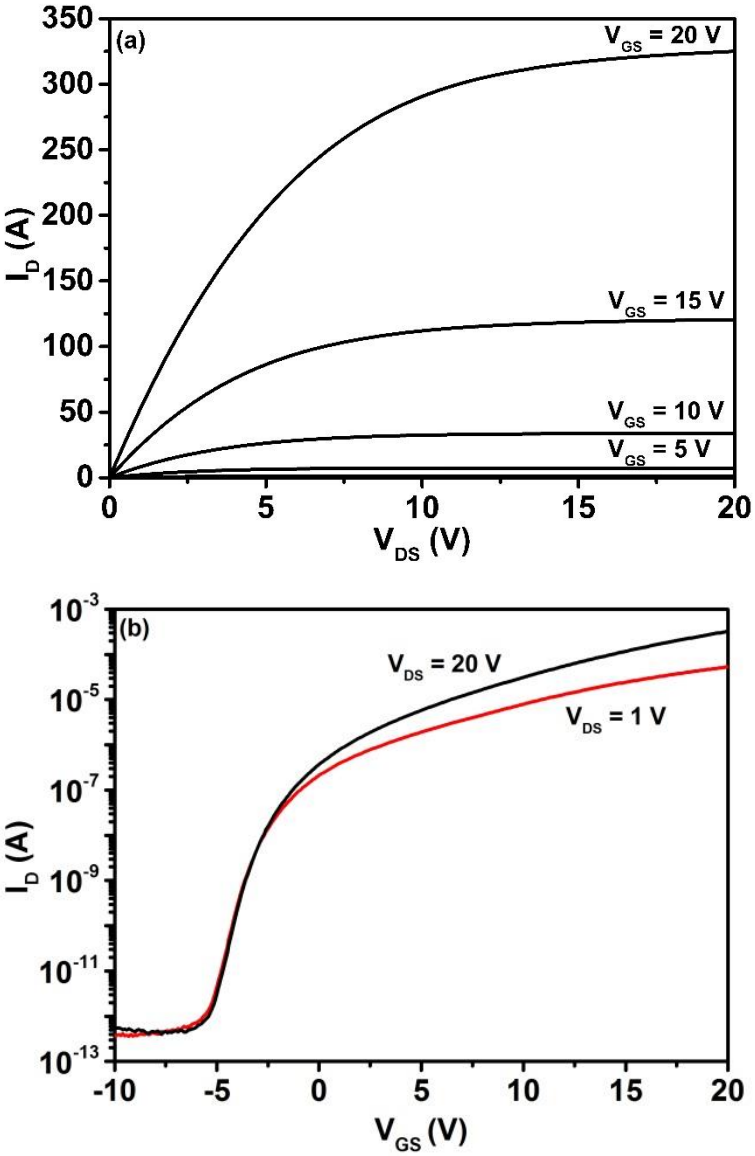

Fig. 5.3 (a) Output and (b) transfer characteristics for 3.8 % NbZnO TFT with a 10 nm Al_2O_3 capping layer

5.4. Physical properties of NbZnO thin films

The physical properties of the NbZnO films were studied to determine the effects of Nb doping. The techniques used were: spectroscopic ellipsometry (SE), photoluminescence (PL), X-ray diffraction (XRD) and X-ray photoelectron spectroscopy (XPS).

5.4.1 Optical properties

The effect of Nb doping on the band gap (E_g) of ZnO was determined using both SE and PL measurements with cycle percentages between 0 to 12.5 %. SE measurements were performed at three angles: 65, 70 and 75°. Fig. 5.4(a) shows the Tauc plot for the 0 and 12.5 % NbZnO film. As ZnO has a direct band gap, the Tauc plot $(\alpha h\omega)^2$ vs. $h\omega$ is plotted in Fig. 5.4 and it is evident that E_g widens from 3.27 to 3.54 eV by shifting the conduction band edge to higher energies. Fig. 5.4(b) demonstrates the effect of the E_g increase with Nb cycle percentages. A small cycle percentage causes E_g to have a linear increase; however, this increase becomes sub-linear with larger Nb cycle percentages, as the E_g tends towards that of niobium oxide [24, 25] (not measured). The increase in band gap is indicative of the Burstein-Moss effect, whereby the carriers arising from the niobium atoms fill the states above the conduction band which, in turn, shifts to higher energies [26]. Furthermore, the Burstein-Moss effect has been confirmed to explain the increase of E_g not only for NbZnO films [13, 15, 16], but also other doped ZnO films such as Mg [27, 28], Ga [10] and Si [11]. The extracted band gap values are shown in Table 5.4.

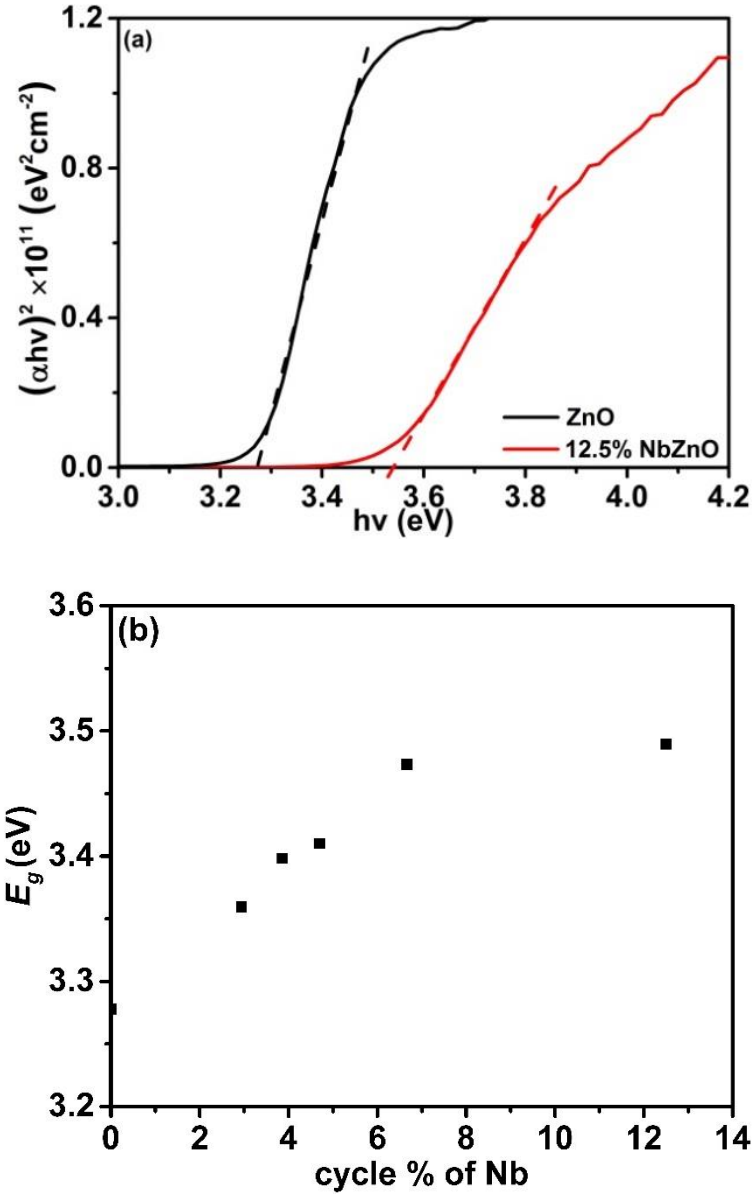

Fig. 5.4 (a) Tauc plot for pure ZnO and 12.5 % NbZnO demonstrating the increase in absorption coefficient and (b) relationship between Nb cycle percentage and the band gap, with a superimposed polynomial fit

Absorption PL measurements were conducted on as-deposited NbZnO films with cycle fractions between 0 and 12.5 % and the intensity peaks are shown in Fig. 5.5. Fig. 5.5 shows that there are two main peak intensities: a UV peak near band-emission around 380 to 340 nm and a green emission peak around 530 nm. Emission in the UV region is associated with the intrinsic transition of excitons from the conduction to the valence band. The UV peak near-band-emission shifts to lower wavelengths with Nb cycle percentage. This confirms that E_g increases with Nb cycle percentage. Extracted band gap values from Fig. 5.5 are shown in Table 5.4 for a comparison with the E_g values obtained from the Tauc plots. It is evident from

Table 5.4 that both measurements reveal similar increases in E_g. The difference between E_g from the two measurement techniques arises from intrinsic measurement error, creation of the SE model and the fact that the samples were fabricated in separate runs. Furthermore, the green emission peak is only observable for Nb cycle percentages above 4.8 %, around 530 nm. This emission is related to the V_o within the ZnO lattice [29]**,** indicating an increase in V_o for large cycle percentages. Although there is an observed increase in V_o for higher Nb cycle percentages, this is observed in as-deposited samples. It is believed that the act of annealing, similar to that used for the TFTs in section 5.3, reduces the V_o peaks shown in Fig. 5.5. This will be addressed in the section 5.4.3, through the XPS analysis.

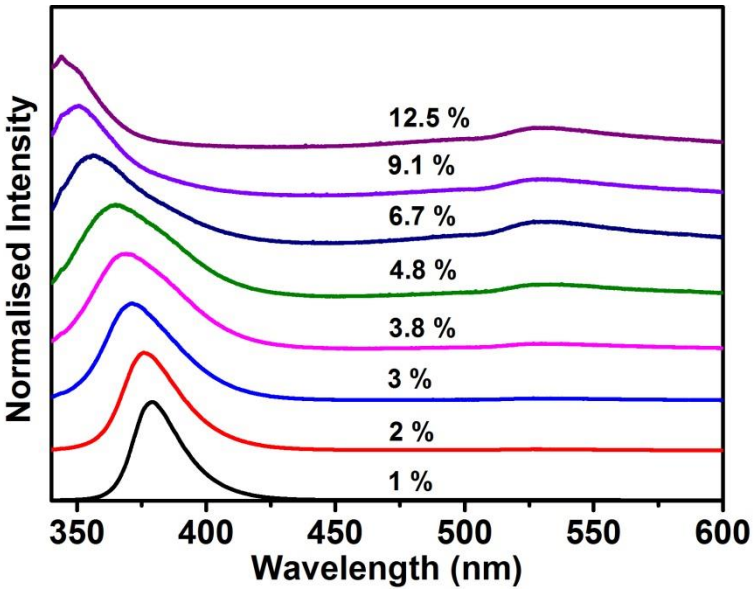

Fig. 5.5 PL measurements of NbZnO with cycle fractions 0 to 12.5 %

Table 5.4 Comparison of band gap values for increased Nb cycle percentages extracted from ellipsometry and PL measurements

Cycle Percentage (%)	E_g **(eV)**	
	Tauc Plot	**PL**
0	3.27	N/a
1.0	N/a	3.26
2.0	3.32	3.30
3.0	3.35	3.33
3.8	3.39	3.35
4.8	3.43	3.40
6.7	3.46	3.47
9.1	3.50	3.52
12.5	3.54	3.56

5.4.2 XRD of NbZnO films

Initial XRD measurements were performed on 200 ºC NbZnO films with cycle percentages between 1 and 9.1 % which had been annealed in air for 1-hour. The crystalline phases were identified by XRD using Cu Kα radiation (0.154 nm, 40 kV, and 50 mA), and the diffraction patterns are shown in Fig. 5.4. The films are polycrystalline with NbZnO with cycle percentages below 9.1 % films, with three observable peaks corresponding to the crystal directions of (100), (002) and (101).

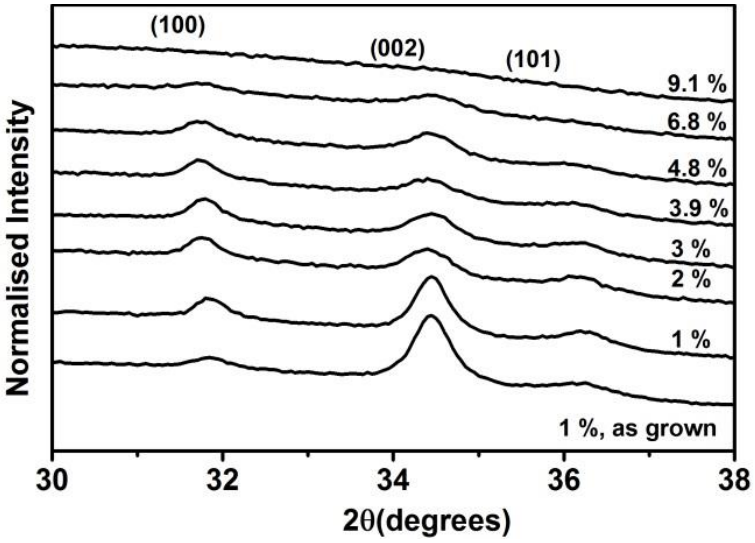

Fig. 5.6 XRD patterns for as-grown and 300 ºC air annealed for 1-hour 200 ºC 1 % to 9.1 % NbZnO

It can be seen in Fig. 5.6 that there is a small increase in the (100) and (101) directionality for 1 % NbZnO when annealed in air at 300 ºC for 1-hour. As the Nb cycle percentage is increased, the intensity of the XRD peaks reduces and above 9.1 % the films are amorphous. Moreover, by calculating the full half-width maximum (FWHM), average grain sizes can be estimated using the Scherrer equation [30], Eqn. (3.6).

The average grain size is shown in Table 5.5 where a reduction from 20.3 nm to 13.4 nm with increased Nb cycle percentages from 1 to 6.8 % is seen. Niobium oxide is inherently amorphous for ALD deposition below 400 ºC [20], which may account for the reduced grain size as the Nb content is increased. Furthermore, the increased V_o shown in Fig. 5.5 can be associated with higher concentrations of dangling bonds arising from the presence in the Nb within the crystal structure. This reduction in grain size is known to occur in films grown by PLD with increasing Nb content [13]. The variation of grain size for 200 ºC deposited NbZnO for different Nb cycle percentages can be compared with the TFT characteristics shown in Table 5.2 and Table 5.3. It is evident that grain boundary scattering is the probable cause for the reduction observed in the saturation mobility, through good agreement on reducing grain

size and μ_{sat} for larger Nb cycle percentages. However, this does not explain the improved mobility observed for initial cycle percentages up to 3 %. It is believed due to the high valency electrons of Nb, the electrons freely move at energies above the lattice so that the effect of grain boundary scattering greatly reduced. However, as the Nb cycle percentage increases grain boundary scattering becomes the limiting effect, restricting the saturation mobility.

Table 5.5 Comparison of FWHM and grain size for NbZnO films deposited at various with cycle percentages between 1 and 9.1 %

Cycle Percentage (%)	**Deposition Temperature (T)**	**FWHM**			**Average Grain Size (nm)**
		(101)	**(002)**	**(101)**	
1 (as-deposited)		0.43	0.49	0.41	18.9
1	200	0.37	0.45	0.42	20.2
2		0.4	0.49	0.45	18.7
3		0.41	0.54	0.42	18.5
	150	0.36	0.77	0.43	16.8
3.8	200	0.33	0.56	0.5	18.5
	225	0.56	0.64	0.6	14.3
4.8		0.46	0.56	0.51	16.4
6.8	200	0.42	0.62	N/a	15.6
9.1		N/a	N/a	N/a	N/a

As 3.8 % NbZnO demonstrated favourable TFT characteristics shown in Table 5.3, XRD measurements were further investigated at two further deposition temperatures: 150 and 225 ^{o}C. The XRD patterns are compared with the 200 ^{o}C deposited NbZnO shown in Fig. 5.6. It is evident from the XRD patterns shown in Fig. 5.7 that higher deposition temperatures produce films with larger grain size. Furthermore, the FWHM and grain sizes for the films are given in Table 5.5, where the deposition temperature has a significant effect on the grain size, as lower temperatures produce films with smaller grain sizes.

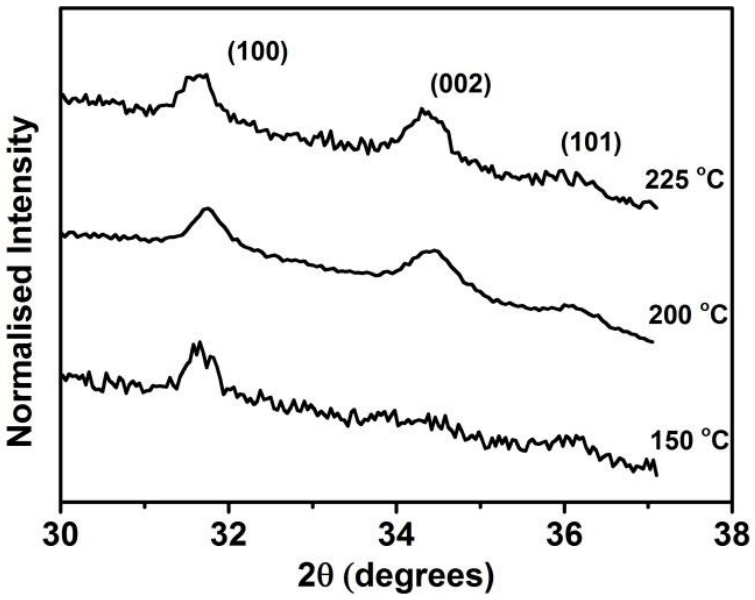

Fig. 5.7 XRD patterns for 3.8 % NbZnO annealed at 300 ºC in air for 1-hour deposited at 150, 200 and 225 ºC

5.4.3 XPS of NbZnO films

XPS was conducted on pure, 3.8 and 12.5 % NbZnO films; the core level (CL) structure and the experimental set up is as described in section 4.2.2**.** The measurements were performed on 10 nm films, which correspond to the nominal surface sensitivity of the technique. The CL spectra for the Nb $3d_{5/2}$, Zn $2p_{3/2}$, O 1s for bulk ZnO, Nb_2O_5, 3.8% and 12.5% NbZnO grown at 200 ºC are shown in Fig. 5.8. Fig. 5.8(a) shows that the Nb $3d_{5/2}$ peak, for bulk Nb_2O_5 has a binding energy (BE) of 207.1 eV indicating the presence of Nb^{5+} [31]. For 3.8% and 12.5% NbZnO, the Nb $3d_{5/2}$ peak shifts to a lower BE of 206.8 eV. Conversely, Fig. 5.8(b) indicates an increase in the BE for the Zn $2p_{3/2}$ peak, from 1020.1 eV for bulk ZnO to 1021.2 eV and 1021.3 eV for 3.8% and 12.5% NbZnO respectively. This implies that Nb^{5+} species are present in the film and act as a substitutional dopant due to the nature of the charge transfer as the Nb replaces the Zn within the structure. Fig. 5.8(c) indicates that for bulk ZnO, the O 1s CL shows 3 sub-peaks relating to (i) the oxygen atoms bonded with nearest neighbour metal ion species (Zn-O); (ii) the oxygen atoms in the vicinity of an oxygen vacancy (labelled as O^{2-} deficiency peak); and (iii) surface oxygen such as O-C-O or hydroxyl groups [31]. Furthermore, 3.8 and 12.5% NbZnO have these sub-peaks with the addition of a sub-peak with a BE of 530.5 eV which is assigned to the presence of an Nb-O environment confirmed by the O 1s Nb_2O_5 peak at the bottom of Fig. 5.8(c). It is evident that the O 1s CL shifts to higher binding energies with the addition of Nb from 529.5 eV to 529.9 eV as a consequence of Nb^{5+} species present within the film. Furthermore, it is evident that there is an increase of O^{2-} deficiencies with increasing Nb^{5+}, shown by the increased sub-peak at 531.4 eV [29, 32]. Moreover, from the XRD spectra in Fig. 5.6, increasing Nb doping concentration serves to reduce the film

crystallinity, potentially creating more dangling bonds as shown in Fig. 5.5; hence, the higher ratio of O^{2-} deficiency sub-peak for 12.5% NbZnO.

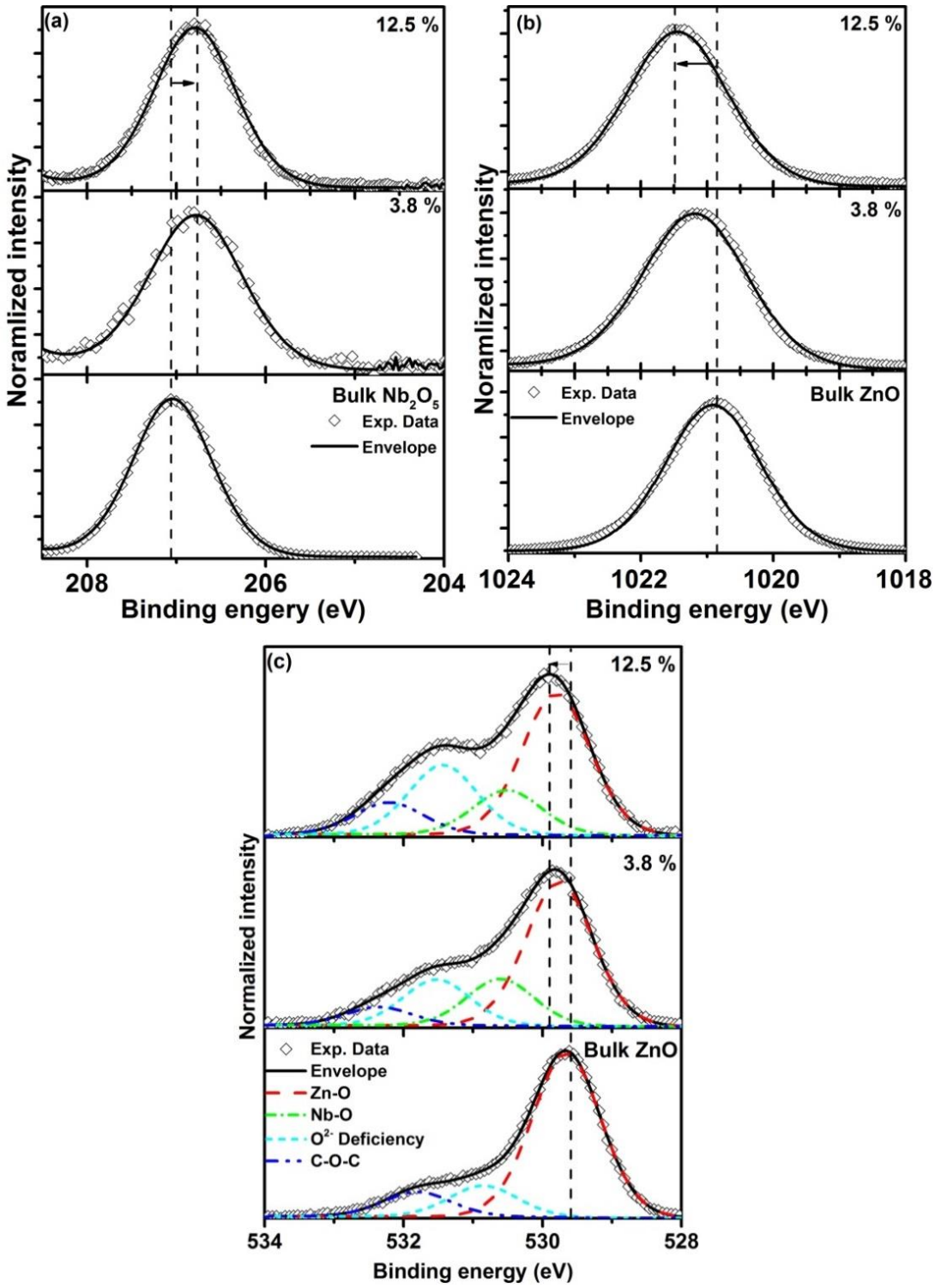

Fig. 5.8 XPS fittings of (a) Nb $3d_{5/2}$ core level for bulk Nb_2O_5, 3.8% NbZnO and 12.5% NbZnO (b) Zn $2p_{3/2}$ core level for bulk ZnO, 3.8% NbZnO and 12.5% NbZnO and (c) O 1s core level for bulk ZnO, 3.8% NbZnO and 12.5% NbZnO

Subsequently, the oxygen vacancies can be reduced by annealing in an oxygen rich environment as shown in Fig. 5.9. Finally, the high binding energy sub-peak is likely to be due to O-C-O and experiences a slight increase with Nb content, presumably related to carbon residue from the ALD process. Furthermore, the ratio between the sub-peaks associated to the Zn and Nb in Fig. 5.8(c) is 25:1 (4 %) and 7:1 (14 %) for the 3.8% and 12.5% NbZnO respectively. This demonstrates that with a growth temperature of 200 ^{o}C, Nb doping does not hinder the growth of the ZnO as the Nb ions replace the Zn sites.

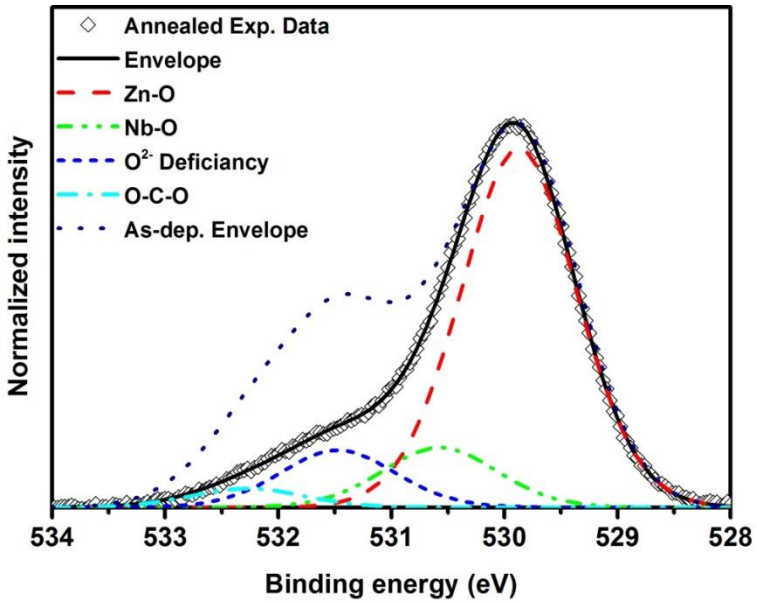

Fig. 5.9 effect of annealing on the O 1s XPS spectra

5.5. Further characterisation of NbZnO films for TFT applications

5.5.1 Current-voltage measurements

Optimisation of the deposition temperature for 3.8 % NbZnO TFTs was conducted between 150 and 250 ºC. TFT parameters for different deposition temperature are given in Table 5.6 with the respective scatter plots in Fig. 5.10 (a) – (d).

Table 5.6 TFT characteristics for the 3.8 % NbZnO growth temperature study showing the average of 5 devices and 1 standard deviation indicated as the error

Temperature (ºC)	**On/Off ratio (10^7)**	**V_T (V)**	**μ_{sat} (cm^2/Vs)**	**Effective *SS* (V/dec)**
150	19 ± 11.7	7.9 ± 0.2	4.8 ± 0.03	0.22 ± 0.04
175	33 ± 21	8.5 ± 0.04	7.9 ± 0.09	0.34 ± 0.04
200	2.9 ± 2.1	9.3 ± 0.04	7.9 ± 0.04	0.47 ± 0.02
225	1.9 ±1.6	9.8 ± 0.07	7.0 ± 0.07	0.87 ± 0.02
250	0.1 ± 0.4	8.7 ± 0.1	4.0 ± 0.1	1.7

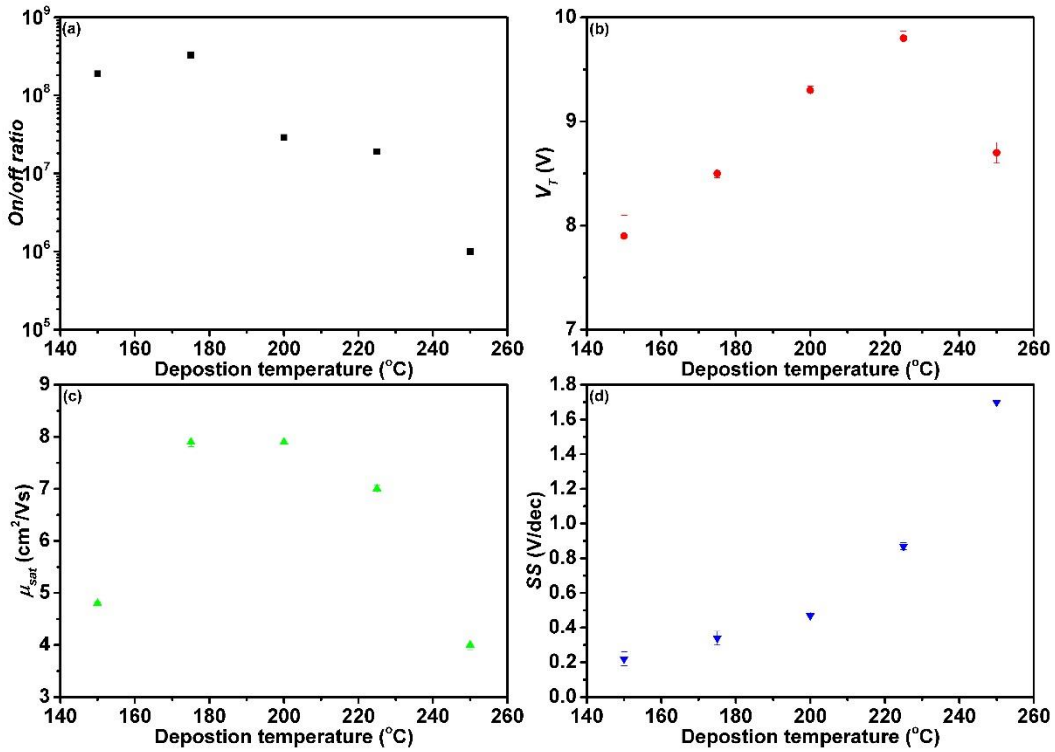

Fig. 5.10 Average scatter plots for the TFT parameters of increasing deposition temperature for 3.8 % NbZnO on 10 nm Al_2O_3 with 1 standard deviation indicated as the error bar. (a) *On/Off ratio*, (b) V_T, (c) μ_{sat} and (d) the effective *SS*.

It is evident that for temperatures below 250 °C, good *On/Off* ratios are achieved. However, the *On/Off* ratio peaks at 175 °C before reducing for higher deposition temperatures. This is indicative of high temperature deposition of ALD ZnO films, whereby the higher the deposition temperatures, the more conductive are the films [33, 34]. The relative large standard deviation for all of the deposition conditions arise from the low current region (10^{-11} A) being affected by the surrounding noise. It is evident in Fig. 5.10(b) as the deposition temperature increases so does the effective V_T until 250 °C, where it reduces. The increase in V_T with temperature can be linked to a lateral shift in the transfer characteristics. This is caused by a degradation at the NbZnO and Al_2O_3 interface as the effective *SS* increases with temperature, as shown in Fig. 5.10(d) and potential charge storage in the Al_2O_3. Moreover, μ_{sat} is roughly constant for temperatures between 175 °C and 225 °C as shown in Fig. 5.10(c). Although 200 °C has a larger grain size than 150 °C (as indicated in Table 5.5) implying grain boundary scattering is not the only factor that affects the saturation mobility. But the niobium concentration plays an integral role on the mobility. However, further physical characterisation would be required on the various deposition temperature NbZnO films to determine the exact Nb:Zn ratio. The lower mobility obtained for 150 °C NbZnO can be attributed to the reduced grain size apparent from Fig. 5.7. It is evident from Table 5.6 and Fig. 5.10 that the 175 and 200 °C NbZnO TFT has the best characteristics, where the 175 °C deposited 3.8 % NbZnO has a high *On/Off* ratio and lower effective V_T. The TFT characteristics of the 175 °C deposited 3.8 % NbZnO are; *On/Off* ratio = 3.3×10^8, μ_{sat} = 7.9 cm^2/Vs and *SS* = 0.34 V/dec, with small standard deviations for $\mu_{sat,}$ effective V_T and effective *SS*. Below in Fig. 5.11(a) and (b) the TFT characteristics are given for a typical 175 °C deposited 3.8 % NbZnO TFT. It is evident in Fig. 5.11(a) that good saturation is achieved in the output characteristics. Fig. 5.11(b) demonstrates that the TFT has good transfer characteristics with a high *On/Off* ratio, a large effective *SS* region over 4 decades and low gate leakage. The low gate leakage is attributed to the Al_2O_3, as discussed in chapter 4. Although promising TFT characteristics, in Fig. 5.11(c) a plot of the $I_D^{0.5}$ against V_{GS} demonstrates that this TFT does not strictly follow a square dependency. The power dependency of the TFT characteristics originate from the sub-band gap density of states within the NbZnO film. More appropriate analysis using a power dependency analytical TFT model will be employed to analyse the sub-band gap density of states in the following section.

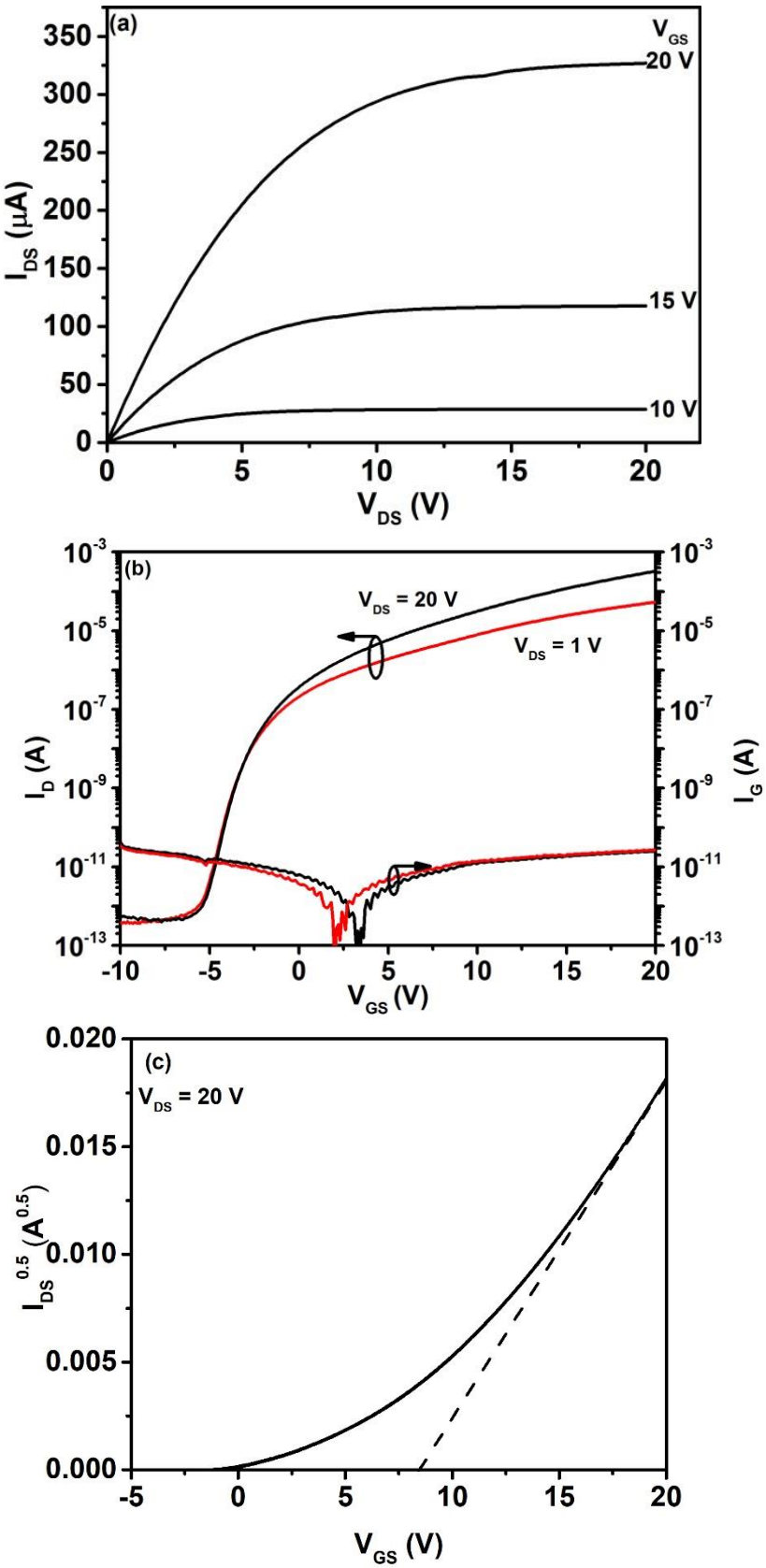

Fig. 5.11 (a) Output characteristics, (b) transfer characteristics for V_{DS} = 1 V and V_{DS} = 20 V of 175 °C grown 3.8% NbZnO TFTs and (c) $I_{DS}^{0.5}$ vs V_{GS} plot showing the power dependency of the *I-V* characteristics

5.5.2 Fitting of NbZnO TFT characteristics using the multiple-trapping and release model

In Fig. 5.3(b) and Fig. 5.11(b), it is evident that the transfer characteristics do not strictly follow a square dependency, but instead follow a power law; hence, the implementation of a physics-based model, which accounts for the density of states (DOS) being adopted. The model implemented is proposed by Torricelli *et al.* [35] and the underlying physics is described in section 3.4.12, using equations (3.22) and (3.23) for the fitting.

By implementing linear regression and utilising the regression coefficient, R^2, the fitted output and transfer characteristics for 3.8 % NbZnO are given in Fig. 5.12.

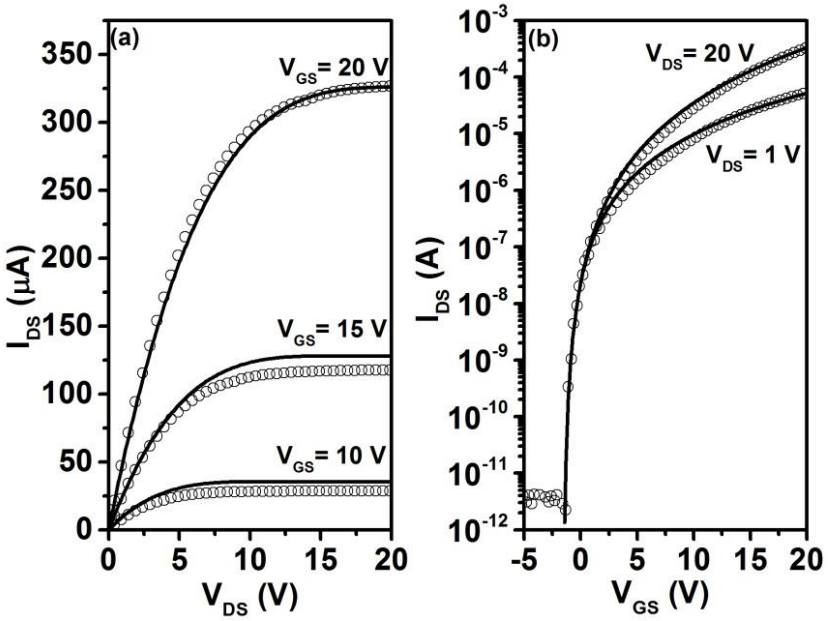

Fig. 5.12 Fitted (a) output characteristics and (b) transfer characteristics for V_{DS} = 1 V and V_{DS} = 20 V of 175 ºC grown 3.8% NbZnO TFTs. The solid line shows the fitted theory of equation (3.22)

It is shown in Fig. 5.12 that both the output and transfer characteristics can be fitted well, with an R^2 of 0.99 and 0.94 respectively. The four fitting parameters: V_{FB}, γ, β and R_D/R_S for the deposition temperatures studied are summarised in Table 5.7. The extracted V_{FB} = − 1.75 V for the 175 ºC TFT correlates directly to the turn-on voltage (V_{on}) in the transfer characteristics shown in Fig. 5.12, which is the voltage required to start to form an accumulation layer. Comparing the *SS* in Table 5.6 and γ in Table 5.7, it is evident that both *SS* and γ improve with deposition temperature, implying that *SS* is dependent on both the interface properties and the disorder within the film. Although variation in deposition temperature produces an insignificant change in N_t, there is a correlation in the increase of the distribution of N_t as indicated by γ.

Table 5.7 Model fitting parameters for 3.8 % NbZnO with different deposition temperatures where OC is the output characteristics and TC is transfer characteristic

Temperature (°C)	V_{FB} (V)	γ	β (A/V$^{\gamma}$)	$R_{D/S}$ (Ω)	R^2	
					OC	TC
150	-4.1	3.6	2.6×10^{-10}	60	0.92	0.99
175	-1.5	3.6	5.3×10^{-10}	20	0.94	0.99
200	-0.5	3.8	2.6×10^{-10}	0	0.96	0.99
225	-1.0	4.1	8.1×10^{-11}	50	0.97	0.99
250	N/a	N/a	N/a	N/a	N/a	N/a

5.5.3 Determination of percolation current

The MTR fitting shown in Fig. 5.12 demonstrates the effect of the sub-band gap tail states on the TFT characteristics. Fig. 5.13 depicts the energy band diagrams for flat band, small V_{GS} and large V_{GS}. For large V_{GS} ($> 2\phi_F$), E_C will sufficiently bend so that the Fermi level, (E_f) enters the conduction band and the carrier concentration becomes degenerate. The conduction band of materials such as ZnO and a-IGZO consists of metal s- and oxide p-orbitals with interaction predominantly between metal–metal neighbours. However, unlike amorphous silicon which has a rigid Si-Si bond length, the distance between the metal-metal ions differ. This spacing between metal neighbours introduces disorder in the conduction band [36] and dictates the power dependency for large V_{GS}. The transition between MTR to percolation current has been demonstrated for IGZO based TFTs [21, 22]. Whereby the power dependency of the transfer characteristics changes under high electric fields.

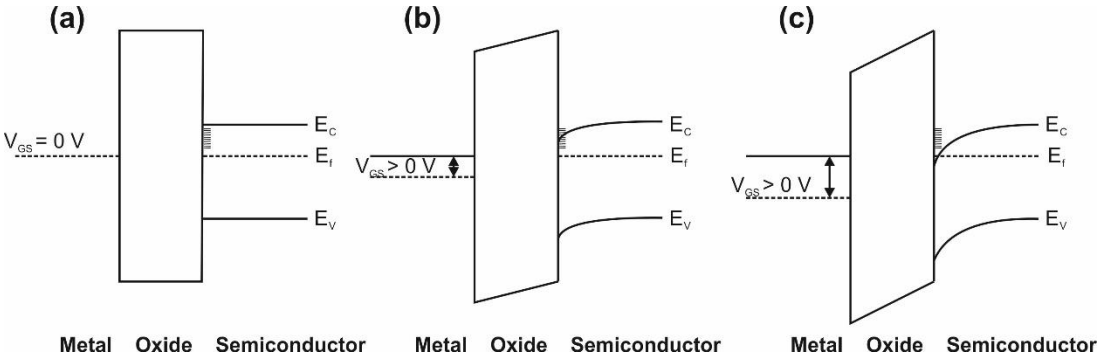

Fig. 5.13 Energy band diagrams for (a) flat band, (b) small V_{GS} and (c) large V_{GS}, where the sub-band gap traps are depicted at the oxide-semiconductor interface.

For Fig. 5.13(a) and (b), it is evident that the majority of carriers will be trapped in the sub-band gap states; hence MTR dominates the conduction mechanism and the field effect mobility (μ_{FE}) is dominated by the ratio between the free and trapped carriers. However, as E_C

further bends due to the applied voltage, the sub-band gap traps are filled. Therefore, E_C at the oxide-semiconductor interface is below E_f as shown in Fig. 5.13(c). Within this region the μ_{FE} is determined by the percolation effect, whereby the carriers move through the path of least resistance. Furthermore, percolation current occurs with large V_{GS} and small V_{DS}, hence this analysis is conducted for V_{DS} = 1 V.

The μ_{FE} was extracted using the gradient of the transfer characteristic, $(\partial I_D/\partial V_g)/(C_i W/L)$ for 175 °C 3.8 % NbZnO TFT with a V_{DS} = 1 V and is shown in Fig. 5.14 as a function of V_{GS}. The symbols in Fig. 5.14 indicate the measured μ_{FE} with a maximum V_{GS} = 35 V. Percolation analysis was conducted, following the method outlined by Lee *et al*. [21], whereby the two power law functions are applied to the extracted μ_{FE} for the trap and percolation dominant regions and are given as:

$$\mu_{FE} = K_{1,2}(V_{GS} - V_{tr,p})^{\gamma_{1,2}} \tag{5.1}$$

where $K_{1,2}$ are constants determined by the percolation modulation of the band mobility in both the trap and percolation regions, $\gamma_{1,2}$ is the power function in the trap and percolation regions respectively, and $V_{tr,p}$ are the transition regions for the trap and percolation dominant regions respectively. The power functions are defined as $\gamma_1 = 2(T_o/T - 1)$ and $\gamma_2 = (D - W_b/D)$ where D is the distance between energy barriers in the conduction band and W_b is the width of the energy barriers. From the MTR model analysis, it was determined that T_o = 540 K, hence γ_1 = 1.6 and $V_{tr} = V_{FB} = -1.5$ V. It can be seen in Fig. 5.14 that the trap limited current region occurs for V_{GS} < 14 V, with an extracted K_1 = 0.06. When V_{GS} > 14 V, percolation current begins to dominate where V_p = 14 V, γ_2 = 0.28 and K_2 = 6.5. By comparison with IGZO [21], the NbZnO film distribution of the states in the conduction band exhibits a larger energy W_b:D ratio. This implies that NbZnO suffers from greater separation between the energy barriers in the conduction band than IGZO.

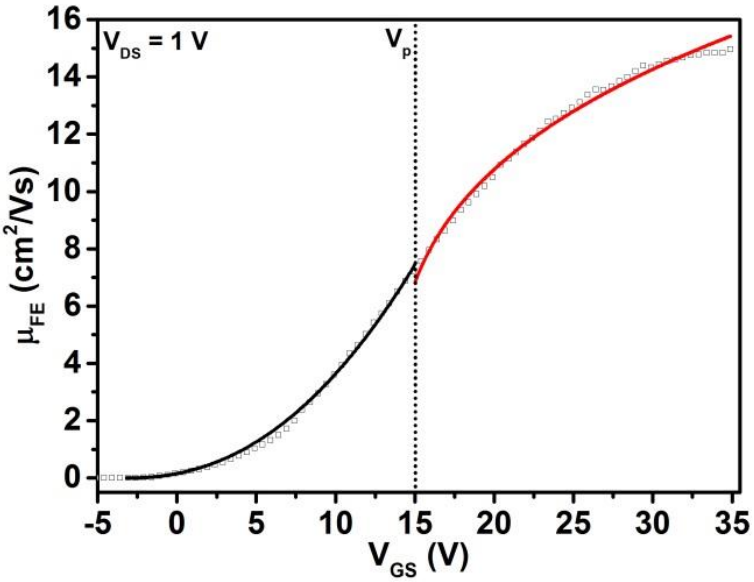

Fig. 5.14 field effect mobility (μ_{FE}) for 175 ºC NbZnO TFT with fitted trap limited and percolation current regions with a V_{DS} = 1 V

5.5.4 Capacitance-voltage measurements

Capacitance-voltage (*C-V*) measurements were conducted on the 175 ºC 3.8 % NbZnO TFTs. The source and drain contacts were grounded and the DC bias with a superimposed small signal was applied to the gate contact (substrate) for frequencies between 100 and 100k Hz. The parallel capacitor and resistor mode was used on the measuring bridge. Fig. 5.15 shows the substrate capacitance (C_{gate}) and the full TFT structure *C-V* characteristics. The substrate capacitance refers to a measurement taken with a metal electrode directly on the gate oxide, to the underlying n^+ Si. For a negative bias, an accumulation layer is induced at the oxide-Si interface and the NbZnO is depleted; the opposite occurs for a positive bias. Large frequency dispersion is evident for accumulation in the NbZnO film (V > 0) and this is attributed to capture-emission events occurring in the bulk of the disordered NbZnO film [37]. The bulk response is represented by effective localized (Q_{loc}) and free carrier (Q_{free}) states associated with the ZnO film which is considered to dominate the response.

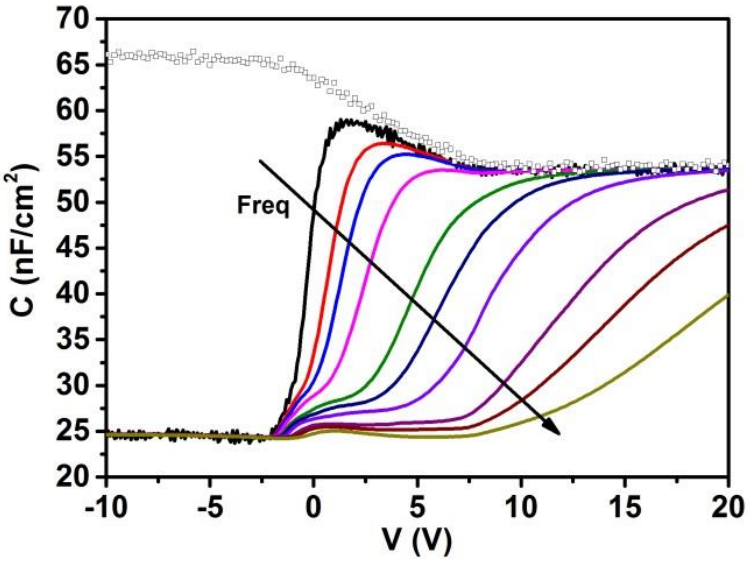

Fig. 5.15 Capacitance-voltage measurements for the substrate (symbols) and 175 ºC 3.5 % NbZnO TFT (lines) for frequencies between 100 Hz and 100 kHz

The donor density, N_d for the substrate can be estimated in the conventional method by iteration of the transcendental equation:

$$N_d = 4\frac{kT}{q^2}\frac{1}{\varepsilon_s}\left[\frac{1}{C_{\min}} - \frac{1}{C_{\max}}\right]^{-2} \ln\left(\frac{N_d}{n_i}\right) \tag{5.2}$$

where C_{min} is the minimum measured capacitance, C_{max} is the maximum measured capacitance and n_i is the intrinsic carrier concentration, 1.5×10^{10} cm^{-3} for Si. It was determined that $N_d = 2.5 \times 10^{18}$ cm^{-3} for the Si substrate, which is consistent with the as-received substrate resistivity of 0.025 – 0.5 Ωcm. The substrate *C*-*V* plot was found to be independent of frequency with a low density of interface states at the thermally grown SiO_2/Si substrate interface. For clarity, a parameter C_{gate} is used below to represent the effective gate oxide capacitance for the response of the ZnO film; that is, $C_{gate}(V) = C_{sub}(V)$.

The analysis for the DOS based *I*-*V* models focuses on the tail region of the trap distribution; however, to obtain an understanding of the deep states, *C*-*V* based analysis is employed. There are three main methods that have been implemented, namely multi-frequency [38, 39], photo-induced *C*-*V* characteristics [40, 41] and a conduction method [39]. The multi-frequency method is adopted here, and the equivalent circuit is given in Fig. 5.16 (a-i).

The total impedance, Z_1 for the equivalent circuit in Fig. 5.16(a-i) is given as:

$$Z_1 = \frac{R_m}{1+(\omega C_m R_m)^2} - j\frac{\omega C_m R_m^2}{1+(\omega C_m R_m)^2} \tag{5.3}$$

where $\omega = 2\pi f$, C_m and R_m are the measured capacitance and resistance respectively. The two-component impedance model can be represented by the four-component model shown in Fig. 5.16(a-ii). It should be noted that the gate oxide leakage current is < 30 pA over the voltage range and the series/contact resistances for the source and drain, R_s are assumed to be frequency independent. The parameter R_s is thus extracted and is shown in Fig. 5.16(b). The inset in Fig. 5.16(b) demonstrates that R_s is determined by the high frequency impedance for each applied voltage.

The four-component impedance model (Z_4) is represented as:

$$Z_2 = R_s + \frac{R_{ch}}{1+(\omega C_{ch} R_{ch})^2} - j\left(\frac{\omega C_{ch} R_{ch}}{1+(\omega C_{ch} R_{ch})^2} + \frac{1}{\omega C_{gate}}\right) \tag{5.4}$$

where C_{ch} and R_{ch} are the channel capacitance and resistances respectively. By assuming $Z_1 = Z_2$, C_{ch} and R_{ch} are obtained using

$$C_{ch} = \frac{bC_{gate}^2 - b^2 C_{gate}}{\left[(ab\omega)^2 + 1\right]C_{gate}^2 - 2bC_{gate} + b^2} \tag{5.5}$$

$$a = \frac{D_m}{\omega C_m (1+D_m^2)} - R_s,\ b = C_m\left(1+D_m^2\right) \text{ and } D_m = \frac{1}{\omega C_m R_m}$$

$$R_{ch} = \sqrt{\frac{C_m\left(1+D_m^2\right) - C_{gate}}{\omega^2 C_{ch}^2 C_{gate} - \omega^2 C_{ch} C_m\left(1+D_m^2\right)\left(C_{ch}+C_{gate}\right)}} \tag{5.6}$$

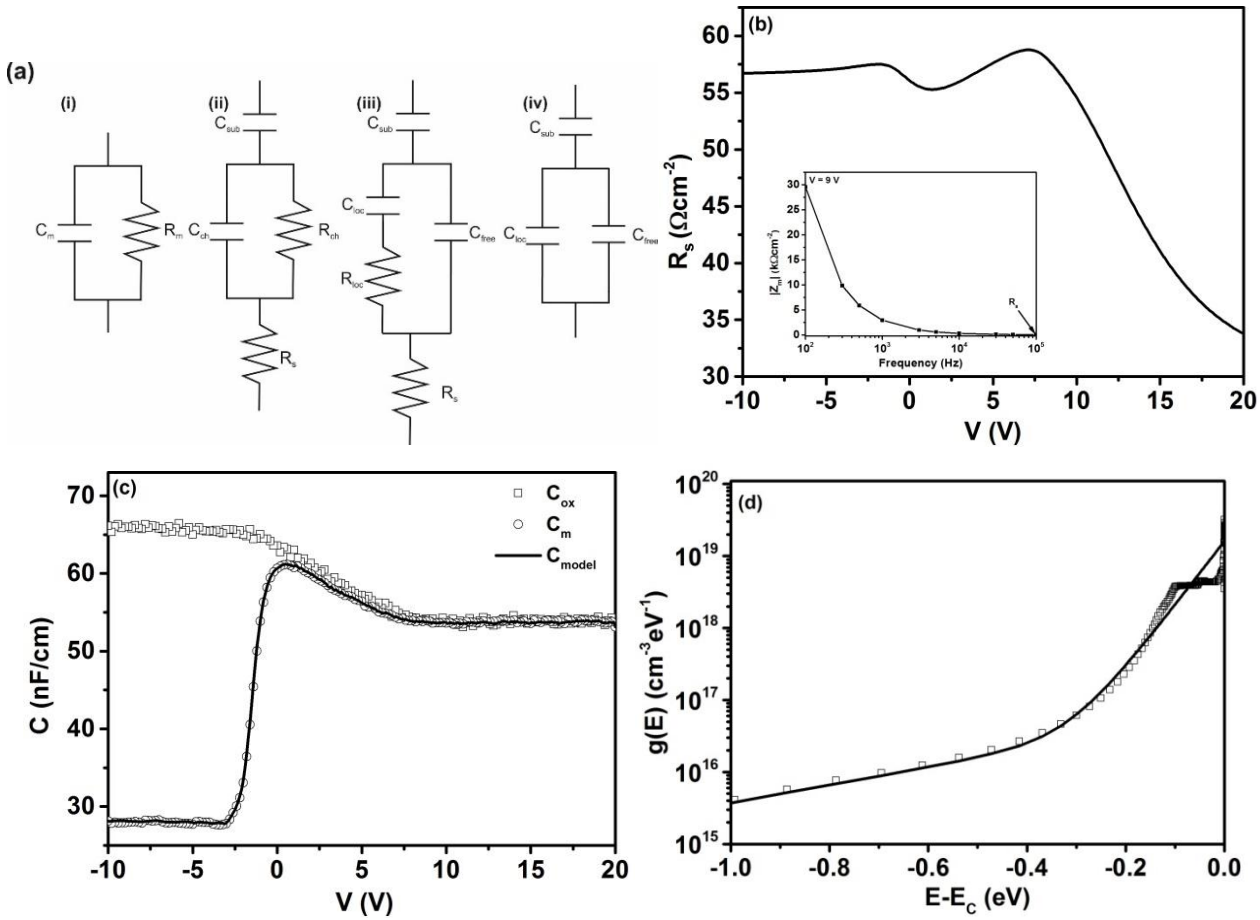

Fig. 5.16(a) i. two-component capacitance model for parallel mode measurement, ii. four-component capacitance model for extraction of R_s and the channel impedance, iii. physics based capacitance model for extracting the C_{loc}, $R_{loc,}$ and C_{free} and iv. frequency independent capacitance model (b) extracted voltage dependent R_s (inset) extraction technique, (c) frequency independent *C-V* characteristics extracted from three frequencies ($f_{1\text{-}3}$=100,10 k and 100 kHz) and (d) the sub-band gap DOS

The channel impedance represents the, frequency dependence of the free and trapped states, where the total Z_{ch} is given by:

$$Z_{ch} = \frac{R_{ch}}{1+(\omega C_{ch} R_{ch})^2} - j\frac{\omega C_{ch} R_{ch}^2}{1+(\omega C_{ch} R_{ch})^2} \tag{5.7}$$

The four-component capacitance model is transformed to the physics-based model, where the channel is dependent on the localised sub-band gap (Q_{loc}) and free electron (Q_{free}) charges. The physics-based model in Fig. 5.16(a-iii) shows that C_{loc} is the capacitance dependent on the voltage dependent Q_{loc} and R_{loc} is the equivalent resistance, and C_{free} is the capacitance due to the voltage dependent Q_{free}. The impedance for the physics-based model (Z_{phys}) is:

$$Z_{phys} = \frac{C_{loc}^2 R_{loc}}{\omega^2 C_{loc}^2 R_{loc}^2 + (C_{loc} + C_{free})^2} - j\frac{\omega^2 C_{loc}^2 C_{free} R_{loc}^2 + (C_{loc} + C_{free})}{\omega^3 C_{loc}^2 C_{free}^2 R_{loc}^2 + \omega(C_{loc} + C_{free})^2} \tag{5.8}$$

where it is assumed that R_{loc} and C_{loc} are frequency independent, the product therefore, determines the frequency dependence (time constant) of Q_{loc}. By using the relationship $Z_{ch} = Z_{phys}$, Eqn. (5.9) can be solved and equating R_{loc} for three measured frequencies. The resultant parameters C_{loc}, C_{free}, and R_{loc} obtained are frequency independent. The corresponding frequency independent model is shown Fig. 5.16(a-iv), where the *C-V* characteristics are shown in Fig. 5.16(c). The model is seen to overlap the measured characteristics indicating excellent agreement. The frequencies used to obtain Fig. 5.16 are: 100 Hz, 10 kHz and 100 kHz; a relatively wide range:

$$R_{loc} = \sqrt{\frac{\omega^2 C_{ch} R_{ch}^2 (C_{loc} + C_{free})(C_{loc} + C_{free} - C_{ch}) - (C_{loc} + C_{free})}{\omega^2 C_{loc}^2 C_{free}[1 + \omega^2 C_{ch} R_{ch}^2 (C_{ch} - C_{free})]}} \tag{5.9}$$

This procedure through Eqns. (5.3) - (5.9), has involved the conversion of the frequency dependent *C-V* characteristics in Fig. 5.15, to frequency independent *C-V* characteristics by employing the equivalent circuit in Fig. 5.16(a-iv). The resultant *C-V* characteristics are shown in Fig. 5.16(c), where it is evident that the model shows excellent agreement with the measured data. As C_{loc} represents the voltage dependence of Q_{loc}, the DOS, $g(E)$ with units $eV^{-1}\ cm^{-3}$, is obtained using:

$$C'_{loc} = \frac{[C_{loc}(V_1) - C_{loc}(V_2)]}{WL} \tag{5.10}$$

$$g(E) = \frac{C'_{loc}}{q^2} \tag{5.11}$$

Finally, a relationship between the applied voltage at the gate and the surface potential (ϕ_s) is required to obtain the effect of the conduction band bending (E_c - E). The ϕ_s is obtained by integrating the frequency independent *C-V* characteristics between V_{FB} and V shown by:

$$\phi_s = \int_{V_{FB}}^{V} \left(1 - \frac{C}{C_{ox}} + Con \right) dV \tag{5.12}$$

where V_{FB} was determined from the fitting of *I-V* measurements using the MTR model and V is associated with the effective V_T ($\sim 2\phi_F$). *Con* is the constant of integration which is used to determine the correct limits of integration by an iteration method. This is a widely known problem in MOS as defined by Berglund [42]. The integral limits V_{FB} *and* V were slightly adjusted (< 5%) to achieve a fit with the DOS derived from a TFT measurement taken on the same material, which is described next.

The extracted DOS using the three frequencies (100, 10k and 100k Hz) is shown in Fig. 5.16 where the two-term exponential approximation given in equation (3.10) is superimposed and indicated by the line. The model parameters are N_{tail} =1.6 × 10^{19} $cm^{-3}eV^{-1}$, T_{tail} =540 K (0.049 eV), N_{deep} = 6.5 × 10^{16} $cm^{-3}eV^{-1}$ and T_{deep} = 4058 K (0.35 eV). By comparison with the MTR model in section 5.4.2, there is good agreement with the number of trapping states near the conduction band ($N_t \sim N_{tail}$) and the characteristic temperatures ($T_o \sim T_{tail}$), demonstrating the dominance of the tail states on the conduction mechanism.

It should be noted that it is not apparent from the experimental *C-V* plots of Fig. 5.15 that the response has become independent of frequency and this implies there may be an associated error in the energy scale for the extracted DOS. The associated error arises from uncertainty in determining the constant of integration in the Berglund integral, given the poorly defined limits. The DOS extracted is therefore representative of those states probed in the measurement. The self-consistency between the DOS extracted from *C-V* and *I-V* techniques provides some confidence that the results can be used in the construction of a compact device model, as described in [35], which is the ultimate motivation for the work.

5.6. Conclusions

Physical and electrical properties of ALD Nb doped ZnO films have been investigated. The process of using Nb as a substitutional dopant increases the E_g of the ZnO towards the E_g of niobium oxide. Moreover, an increased Nb cycle serves to reduce the crystallinity where cycle percentages above 6.9 % produce amorphous films. Both PL and XPS measurements indicate that increasing cycle percentages serve to increase the oxygen deficiency within the film. However, XPS demonstrated annealing in air serves to remove the deficiency. TFTs were fabricated with cycle percentages ranging from 1 to 12.5 % and deposited between 150 and 250 ^{o}C. The TFT characteristics indicate that increasing the Nb cycle percentage and reducing the deposition temperature reduces the conductivity of the NbZnO. A film composition of 3.8 % NbZnO deposited at 175 ^{o}C provides the best TFT performance in relation to highest μ_{sat}, *SS* and *On/Off* ratio. It was demonstrated for the I-V characteristics of NbZnO TFT that the MTR model represents the conduction mechanism and thus allows extraction of the exponential tail state distribution. Moreover, when the conduction band is sufficiently bent to the Fermi level, percolation current becomes the dominant transport mechanism. *C-V* measurements demonstrate a large frequency dispersion for the 3.8 % NbZnO film due to capture-emission events occurring in the bulk and frequency sensitive localised states. The DOS of the deep and tail states was extracted from the *C-V* measurements. Furthermore, the *C-V* derived DOS showed excellent agreement with that derived from the *I-V* measurements, modelled by the MTR theory. There is good agreement found between the two extraction techniques with the qualification that it was necessary to adjust the *C-V* flat band voltage by < 5% to realise the fit.

5.7. References

[1] H. Hosono, "Ionic amorphous oxide semiconductors: Material design, carrier transport, and device application," *Journal of Non-Crystalline Solids*, vol. 352, no. 9–20, pp. 851-858, 2006.

[2] H. Yabuta, M. Sano, K. Abe, T. Aiba, T. Den, H. Kumomi, K. Nomura, T. Kamiya, and H. Hosono, "High-mobility thin-film transistor with amorphous $InGaZnO_4$ channel fabricated by room temperature rf-magnetron sputtering," *Applied Physics Letters*, vol. 89, no. 11, p. 112123, 2006.

[3] K. Nomura, T. Akihiro, K. Toshio, O. Hiromichi, H. Masahiro, and H. Hideo, "Amorphous Oxide Semiconductors for High-Performance Flexible Thin-Film Transistors," *Japanese Journal of Applied Physics*, vol. 45, no. 5S, p. 4303, 2006.

[4] M. Kim, J. H. Jeong, H. J. Lee, T. K. Ahn, H. S. Shin, J.-S. Park, J. K. Jeong, Y.-G. Mo, and H. D. Kim, "High mobility bottom gate InGaZnO thin film transistors with SiO_x etch stopper," *Applied Physics Letters*, vol. 90, no. 21, p. 212114, 2007.

[5] J. K. Jeong, J. H. Jeong, H. W. Yang, J.-S. Park, Y.-G. Mo, and H. D. Kim, "High performance thin film transistors with cosputtered amorphous indium gallium zinc oxide channel," *Applied Physics Letters*, vol. 91, no. 11, p. 113505, 2007.

[6] J. S. Lee, S. Chang, S. M. Koo, and S. Y. Lee, "High-Performance a-IGZO TFT With ZrO_2 Gate Dielectric Fabricated at Room Temperature," *IEEE Electron Device Letters*, vol. 31, no. 3, pp. 225-227, 2010.

[7] D. H. Kang, I. Kang, S. H. Ryu, and J. Jang, "Self-Aligned Coplanar a-IGZO TFTs and Application to High-Speed Circuits," *IEEE Electron Device Letters*, vol. 32, no. 10, pp. 1385-1387, 2011.

[8] ECORYS, "Mapping resource prices: the pas and the future," ECORYS2012.

[9] C. J. Ku, W. C. Hong, T. Mohsin, R. Li, Z. Duan, and Y. Lu, "Improvement of Negative Bias Stress Stability in Mg0.03Zn0.97O Thin-Film Transistors," *IEEE Electron Device Letters*, vol. 36, no. 9, pp. 914-916, 2015.

[10] T. Prasada Rao and M. C. Santhosh Kumar, "Physical properties of Ga-doped ZnO thin films by spray pyrolysis," *Journal of Alloys and Compounds*, vol. 506, no. 2, pp. 788-793, 2010.

[11] S.-H. Lee, K.-W. Cha, and J.-S. Park, "Effects of furnace annealing and hot pressing on the properties of SZO thin films and on the characteristics of SZO-TFTs," *Thin Solid Films*, vol. 596, pp. 72-76, 2015.

[12] J. M. Lin, Y. Z. Zhang, Z. Z. Ye, X. Q. Gu, X. H. Pan, Y. F. Yang, J. G. Lu, H. P. He, and B. H. Zhao, "Nb-doped ZnO transparent conducting films fabricated by pulsed laser deposition," *Applied Surface Science*, vol. 255, no. 13–14, pp. 6460-6463, 2009.

[13] J. Shao, W. Dong, D. Li, R. Tao, Z. Deng, T. Wang, G. Meng, S. Zhou, and X. Fang, "Metal-semiconductor transition in Nb-doped ZnO thin films prepared by pulsed laser deposition," *Thin Solid Films*, vol. 518, no. 18, pp. 5288-5291, 2010.

[14] F. Cao, Y.-D. Wang, D.-L. Liu, J.-Z. Yin, B.-J. Guo, L. Li, and Y.-P. An, "Preparation and Characterization of Transparent Conductive Nb-Doped ZnO Films by Radio-Frequency Sputtering," *Chinese Physics Letters*, vol. 26, no. 3, p. 034210, 2009.

[15] V. Gokulakrishnan, S. Parthiban, K. Jeganathan, and K. Ramamurthi, "Structural, Optical, and Electrical Properties of Nb-Doped ZnO Thin Films Prepared by Spray Pyrolysis Method," *Journal of Electronic Materials*, vol. 40, no. 12, p. 2382, 2011.

[16] H. Yoon, B. N. Joshi, S.-H. Na, J.-Y. Choi, and S. S. Yoon, "Photodegradation of methylene blue of niobium-doped zinc oxide thin films produced by electrostatic spray deposition," *Ceramics International*, vol. 40, no. 5, pp. 7567-7571, 2014.

[17] K.-C. Ok, J. Park, J. H. Lee, B. D. Ahn, J. H. Lee, K.-B. Chung, and J.-S. Park, "Semiconducting behavior of niobium-doped titanium oxide in the amorphous state," *Applied Physics Letters*, vol. 100, no. 14, p. 142103, 2012.

[18] S.-H. Kim, J. Kwang-Seok, Y. Ho-Jin, Y. Seung-Dong, K. Yu-Mi, K. Jin-Seop, K. Young-Uk, A. Jin-Un, L. Hi-Deok, and L. Ga-Won, "Channel engineering of ZnO-based thin film transistors using Al2O3 interlayer grown by atomic layer deposition," *Japanese Journal of Applied Physics*, vol. 53, no. 9, p. 091101, 2014.

[19] J. Yang, J. K. Park, S. Kim, W. Choi, S. Lee, and H. Kim, "Atomic-layer-deposited ZnO thin-film transistors with various gate dielectrics," *physica status solidi (a)*, vol. 209, no. 10, pp. 2087-2090, 2012.

[20] T. Blanquart, J. Niinistö, M. Heikkilä, T. Sajavaara, K. Kukli, E. Puukilainen, C. Xu, W. Hunks, M. Ritala, and M. Leskelä, "Evaluation and Comparison of Novel Precursors for Atomic Layer Deposition of Nb_2O_5 Thin Films," *Chemistry of Materials*, vol. 24, no. 6, pp. 975-980, 2012.

[21] S. Lee, K. Ghaffarzadeh, A. Nathan, J. Robertson, S. Jeon, C. Kim, I.-H. Song, and U.-I. Chung, "Trap-limited and percolation conduction mechanisms in amorphous oxide semiconductor thin film transistors," *Applied Physics Letters*, vol. 98, no. 20, p. 203508, 2011.

[22] M. Ghittorelli, F. Torricelli, and Z. M. Kovács-Vajna, "Analytical Physical-Based Drain-Current Model of Amorphous InGaZnO TFTs Accounting for Both Non-Degenerate and Degenerate Conduction," *IEEE Electron Device Letters*, vol. 36, no. 12, pp. 1340-1343, 2015.

[23] M. Ghittorelli, F. Torricelli, and Z. M. Kovács-Vajna, "Physical Modeling of Amorphous InGaZnO Thin-Film Transistors: The Role of Degenerate Conduction," *IEEE Transactions on Electron Devices*, vol. 63, no. 6, pp. 2417-2423, 2016.

[24] A. D. Weerakkody, N. Sedghi, I. Z. Mitrovic, H. van Zalinge, I. Nemr Noureddine, S. Hall, J. S. Wrench, P. R. Chalker, L. J. Phillips, R. Treharne, and K. Durose, "Enhanced low voltage nonlinearity in resonant tunneling metal–insulator–insulator–metal nanostructures," *Microelectronic Engineering*, vol. 147, pp. 298-301, 2015.

[25] Z. Weibin, W. Weidong, W. Xueming, C. Xinlu, Y. Dawei, S. Changle, P. Liping, W. Yuying, and B. Li, "The investigation of NbO_2 and Nb_2O_5 electronic structure by XPS, UPS and first principles methods," *Surface and Interface Analysis*, vol. 45, no. 8, pp. 1206-1210, 2013.

[26] M. Grundmann, "Optical Properties," in *The Physics of Semiconductors*: An Introduction Including Nanophysics and Applications, Berlin, Heidelberger: Springer Berlin Heidelberger, 2010, pp. 265-307.

[27] T. Törndahl, C. Platzer-Björkman, J. Kessler, and M. Edoff, "Atomic layer deposition of $Zn_{1-x}Mg_xO$ buffer layers for $Cu(In,Ga)Se_2$ solar cells," *Progress in Photovoltaics: Research and Applications*, vol. 15, no. 3, pp. 225-235, 2007.

[28] C. Y. Liu, H. Y. Xu, L. Wang, X. H. Li, and Y. C. Liu, "Pulsed laser deposition of high Mg-content MgZnO films: Effects of substrate temperature and oxygen pressure," *Journal of Applied Physics*, vol. 106, no. 7, p. 073518, 2009.

[29] P.-T. Hsieh, Y.-C. Chen, K.-S. Kao, and C.-M. Wang, "Luminescence mechanism of ZnO thin film investigated by XPS measurement," *Applied Physics A*, vol. 90, no. 2, pp. 317-321, 2008.

[30] A. L. Patterson, "The Scherrer Formula for X-Ray Particle Size Determination," *Physical Review*, vol. 56, no. 10, pp. 978-982, 1939.

[31] M. K. Bahl, "ESCA studies of some niobium compounds," *Journal of Physics and Chemistry of Solids*, vol. 36, no. 6, pp. 485-491, 1975.

[32] Y. Jung, W. Yang, C. Y. Koo, K. Song, and J. Moon, "High performance and high stability low temperature aqueous solution-derived Li-Zr co-doped ZnO thin film transistors," *Journal of Materials Chemistry*, vol. 22, no. 12, pp. 5390-5397, 2012.

[33] E. Guziewicz, M. Godlewski, L. Wachnicki, T. A. Krajewski, G. Luka, S. Gieraltowska, R. Jakiela, A. Stonert, W. Lisowski, M. Krawczyk, J. W. Sobczak, and A. Jablonski, "ALD grown zinc oxide with controllable electrical properties," *Semiconductor Science and Technology*, vol. 27, no. 7, p. 074011, 2012.

[34] J. Laube, D. Nübling, H. Beh, S. Gutsch, D. Hiller, and M. Zacharias, "Resistivity of atomic layer deposition grown ZnO: The influence of deposition temperature and post-annealing," *Thin Solid Films*, vol. 603, pp. 377-381, 2016.

[35] F. Torricelli, J. R. Meijboom, E. Smits, A. K. Tripathi, M. Ferroni, S. Federici, G. H. Gelinck, L. Colalongo, Z. M. Kovacs-Vajna, D. d. Leeuw, and E. Cantatore, "Transport Physics and Device Modeling of Zinc Oxide Thin-Film Transistors Part I: Long-Channel Devices," *IEEE Transactions on Electron Devices*, vol. 58, no. 8, pp. 2610-2619, 2011.

[36] J. Robertson, "Disorder and instability processes in amorphous conducting oxides," *physica status solidi (b)*, vol. 245, no. 6, pp. 1026-1032, 2008.

[37] A. K. Das, P. Misra, and L. M. Kukreja, "Effect of Si doping on electrical and optical properties of ZnO thin films grown by sequential pulsed laser deposition," *Journal of Physics D: Applied Physics*, vol. 42, no. 16, p. 165405, 2009.

[38] S. Lee, S. Park, S. Kim, Y. Jeon, K. Jeon, J. H. Park, J. Park, I. Song, C. J. Kim, Y. Park, D. M. Kim, and D. H. Kim, "Extraction of Subgap Density of States in Amorphous InGaZnO Thin-Film Transistors by Using Multifrequency Capacitance-Voltage Characteristics," *IEEE Electron Device Letters*, vol. 31, no. 3, pp. 231-233, 2010.

[39] J. Jang, J. Kim, M. Bae, J. Lee, D. M. Kim, D. H. Kim, J. Lee, B.-L. Lee, B. Koo, and Y. W. Jin, "Extraction of the sub-bandgap density-of-states in polymer thin-film transistors with the multi-frequency capacitance-voltage spectroscopy," *Applied Physics Letters*, vol. 100, no. 13, p. 133506, 2012.

[40] K. Jeon, C. Kim, I. Song, J. Park, S. Kim, S. Kim, Y. Park, J.-H. Park, S. Lee, D. M. Kim, and D. H. Kim, "Modeling of amorphous InGaZnO thin-film transistors based on the density of states extracted from the optical response of capacitance-voltage characteristics," *Applied Physics Letters*, vol. 93, no. 18, p. 182102, 2008.

[41] J. H. Park, K. Jeon, S. Lee, S. Kim, S. Kim, I. Song, C. J. Kim, J. Park, Y. Park, D. M. Kim, and D. H. Kim, "Extraction of Density of States in Amorphous GaInZnO Thin-Film Transistors by Combining an Optical Charge Pumping and Capacitance-Voltage Characteristics," *IEEE Electron Device Letters*, vol. 29, no. 12, pp. 1292-1295, 2008.

[42] C. N. Berglund, "Surface states at steam-grown silicon-silicon dioxide interfaces," *IEEE Transactions on Electron Devices*, vol. ED-13, no. 10, pp. 701-705, 1966.

Chapter 6

6. Plasma enhanced atomic layer deposition zinc oxide Schottky diodes

6.1. Introduction

High quality Schottky contacts are an integral requirement for a wide range of electronic applications. The use of Schottky contacts on ZnO films has a range of proposed applications including: gas sensors [1-3], metal-semiconductor FETs and ultraviolet photo-detectors [4, 5]. The effective use of Schottky contacts on ZnO thin-films remains a challenge due to the dependence of high quality interface properties between the metal-ZnO and the electrical properties of ZnO.

For ZnO Schottky contacts, metals with a large work function are required for producing a sufficiently high barrier height (ϕ_B) due to the high electron affinity (χ) of ZnO. The preferred Schottky contacts for ZnO are gold (Au), silver (Ag), palladium (Pd) and platinum (Pt) [6-12] due to their high conductivity and large work functions. Typically, bulk ZnO is the preferred growth technique as highlighted in Table 2.5, however, studies using ZnO thin-films deposited by metal organic chemical vapour deposition (MO*C*VD) [6, 7], pulse layer deposition (PLD) [8, 9], sputtering [10] and ALD [11] have been demonstrated, although ALD ZnO Schottky diodes suffer from large ideality factors, typically > 2.

The Schottky contacts outlined above should, theoretically, produce a large ϕ_B and relatively low ideality factors. However, defect states within the ZnO films give rise to a high density of traps within the band gap [13]. These states are predominantly associated with oxygen vacancies and zinc interstitials and tend to allow for trap-assisted tunnelling. Another factor for low barrier height contacts is the high densities of surface oxygen deficiencies [14] which can be mitigated by depositing thin layers of oxidised metals such as Ag_xO, Pd_xO and PtO_x [15-18]. The use of oxygen reduces the surface deficiencies to create a homogenous interface between the ZnO and Schottky contact. These metals are commonly deposited by reactive RF sputtering with small concentration of oxygen added to the chamber. The effect of metal oxide Schottky contacts is to increase the rectification ratio and help to reduce the ideality factor (η) [15, 16, 19].

In this chapter ZnO films deposited by plasma enhanced atomic layer deposition (PEALD) for Schottky diodes using contacts subject to oxygen treatment are investigated.

6.2. Current-voltage characterisation

The current density-voltage (*J-V*) characteristics in this chapter are analysed assuming thermionic emission as the dominant conduction mechanism given as:

$$J = J_o\left[\exp\left(\frac{q(V - JR_s)}{\eta kT}\right) - 1\right] \tag{6.1}$$

where V is the applied voltage at the Schottky contact η is the ideality factor R_s is the series resistance, k is Boltzmann's constant, T is the measurement temperature, q is the charge of the electron and J_o is the zero-bias current density given as:

$$J_o = A^* T^2 \exp\left(-\frac{q\phi_B}{kT}\right) \tag{6.2}$$

A^* is the Richardson constant with a theoretical value of 32 $cm^{-2}K^{-2}$ for ZnO [19]. The rectification ratio is defined here as the difference in current density between ± 1 V and is indicated in the *J-V* characteristics in Fig. 6.1(a). By taking the inverse of the steepest slope in the log-linear *J-V* characteristics, η can be found as shown from the red dashed line in Fig. 6.1(a). Obtaining an accurate J_o from the intercept with the *y*-axis is problematic for ideality factors greater than 1. Rhoderick and Williams [20] outlined a method whereby plotting $\ln[J/(1-\exp(qV/kT))]$ against V gives an accurate estimate for J_o. Using this technique, J_o is obtained from the intercept with the *y*-axis and this technique is shown in Fig. 6.1(b). Once J_o is known, the barrier height is determined by re-arranging Eqn. (6.2). The Schottky diode shown in Fig. 6.1 has the following characteristics; rectification ratio of 1×10^7, η = 1.44 and $\phi_{B,\,J\text{-}V}$ = 0.71 eV. The value for ideality is very high and not consistent with the thermionic emission theory. This matter is discussed later.

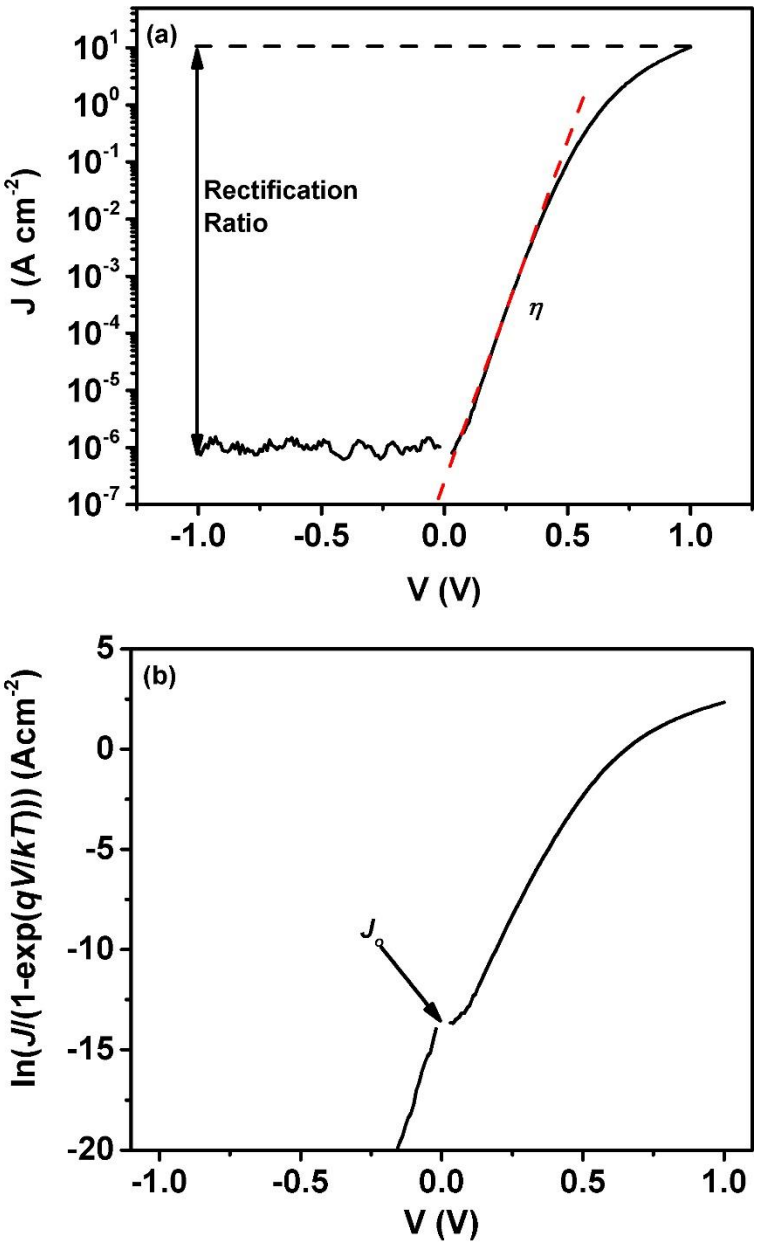

Fig. 6.1(a) typical *J-V* characteristics of a Schottky diode showing the extraction of the rectification ratio and η and (b) J_o using the method outlined by Rhoderick and Williams [20]

6.3.Initial thermal-ALD Schottky diodes

Initial experiments were performed on thermally deposited ALD ZnO films. The ZnO layers were fabricated on SiO_2/Si substrates to a thickness of 50 nm with a substrate temperature of 200 ^oC, using ALD with DEZn (Strem) and DI water as the precursors. The ZnO layers were deposited by the functional material research group at the University of Liverpool. Lateral Schottky diodes were fabricated with the device structure shown in the inset of Fig. 6.2. Both ohmic and Schottky contacts were thermally evaporated using Al (Fisher Scientific) and Ag

(Kurt J. Lesker) respectively, to a thickness of approximately 70 nm, which was measured using the internal quartz thickness monitor.

The *J-V* characteristics of the Schottky diode for the best as-deposited, 160 and 200 ^{o}C post deposition annealed are shown in Fig. 6.2. For each sample 5 devices were measured on separate substrates where the ZnO was deposited with the same chamber conditions. It is evident that for all the Schottky diodes, the rectification ratio is below 10 (7.6, 2.6 and 6 for as-deposited, 160 and 200 ^{o}C annealed respectively). The effect of annealing serves a similar purpose to ZnO TFTs as shown in Chapters 4 and 5, where the conductivity of the film is reduced by decreasing the current density. However, there is no significant reduction to the reverse current. The large reverse current is indictive of the films not being fully depleted as the film are too conductive, i.e. the maximum depletion width is less than the films thickness.

The ideality factors (η) for each Schottky diode was taken from the steepest slope in the forward *J-V* characteristic as outlined in section 6.2 and are 5.4, 5.8 and 5.7 for as-deposited, 160 and 200 ^{o}C annealed respectively. The barrier heights ($\phi_{B,J\text{-}V}$) measured were 0.48,0.53 and 0.58 eV for as-deposited, 160 and 200 ^{o}C annealed respectively. The barrier heights increase for the annealed Schottky diodes by up to 0.1 eV as the film becomes more resistive and the Fermi-level is moves further from the conduction band edge. The high ideality factors are suggestive of tunnelling current being the dominant conduction mechanism for these ALD Schottky diodes. Moreover, the low barrier heights indicate poor interface properties, which result in Fermi-level pinning and conductive films, where the Fermi level is in close proximity to the conduction band.

Notably, annealing the Schottky diodes at temperatures above 200 ^{o}C resulted in no rectification behaviour, which is believed to be due to the breakdown of the Ag Schottky contact. It is evident that the Schottky diodes shown in Fig. 6.2 are highly none ideal and are similar to other reported ALD based Schottky diodes. There are two distinct difficulties which require addressing: the successful reduction of the ZnO conductivity to $< 10^{17}$ cm^{-3} and improvement of the interface properties between the Schottky contact and ZnO. From the difficulties outlined, the focus of this chapter will be on PEALD ZnO and the use of oxidised metals. Although, PEALD can increase the complexity of deposition, it has been shown to be an effective method into reducing ZnO conductivity relative to the deposition temperature [21].

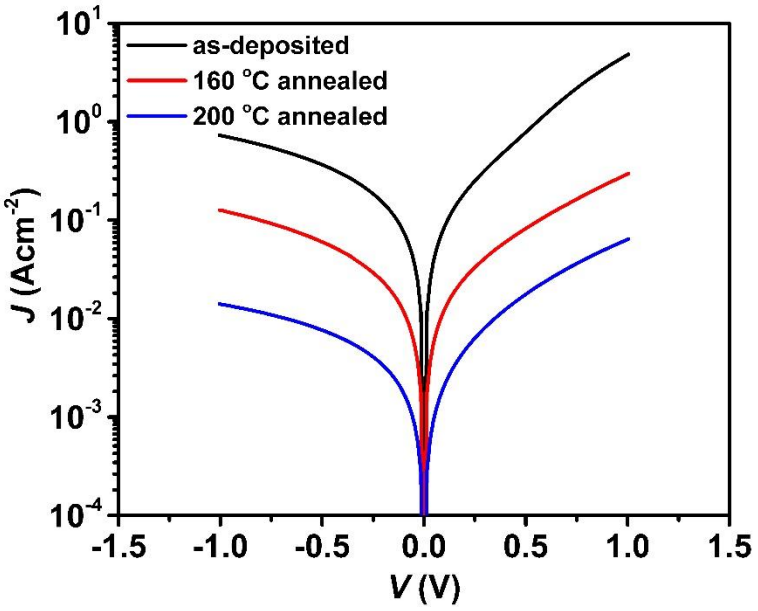

Fig. 6.2 200 °C ALD deposited ZnO Schottky diodes with Ag as the Schottky contact, post deposition annealed at various temperatures

6.4. Experimental details

The schematic of the fabricated Schottky diodes is shown in Fig. 6.3. A 70 nm thick Ti layer was deposited as the Ohmic contact on top of a SiO_2/Si substrate. The Ti was deposited by RF sputtering using a Moorfield nanoPVD with a target purity of 99.995 %(Kurt J. Lesker) at 73 W, in pure Ar atmosphere at a chamber pressure of 3.5×10^{-3} mbar. The samples were loaded into an Oxford Instruments Plasma OPAL reactor for deposition of the PEALD ZnO, where PEALD deposition was done by the functional materials research group at the University of Liverpool. The Zn precursor and oxidising reagent used were DEZn (Strem) and an Ar/O_2 plasma, where the DEZn entered the chamber at room temperature. The O_2 plasma consisted of gas flow rates of 100 and 60 sccm for the Ar and O_2 gases respectively, with an RF power of 300 W. The DEZn and O_2 plasma were sequentially introduced into the chamber with an Ar purge to ensure the self-limiting reaction occurred on the surface. After ZnO deposition, the films were etched with glacial acetic acid (Fisher Scientific) diluted to 1 % with DI water for 10 s to expose the Ohmic Ti contact. The Schottky contacts were subsequently RF sputtered and defined via a shadow mask with a device area of 78.5×10^{-6} cm^{-2}. All Schottky contacts were subject to a chamber atmosphere consisting of Ar/O_2 to form the metal oxide contact and each contact was capped with a 10 nm layer of un-oxidised metal. For example, an Ag_xO Schottky contact is deposited with an RF power of 45 W and an Ar/O_2 flow rate of 1/1 sccm to a thickness of 10 nm. Subsequently a pure Ag capping layer was deposited without breaking the chamber with a power of 45 W and an Ar/O_2 flow rate of 1/0 sccm to a thickness of 40 nm. In this case a 2" Ar target (99.99 %,

Kurt J. Lesker) was used for both layers. The influence of deposition temperature, O_2 plasma time and film thickness were investigated and are reported below. The Schottky contacts were deposited by Dr. J. Jin.

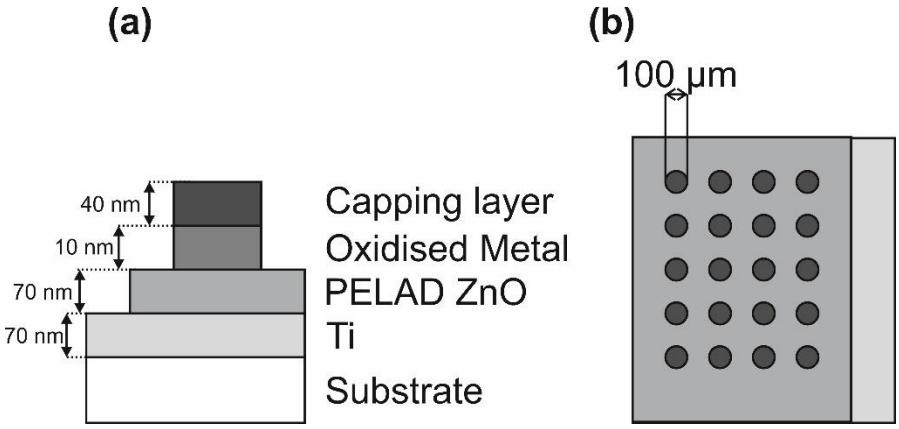

Fig. 6.3 (a) Cross sectional and (b) top view diagram for the fabricated Schottky diodes

6.5. Optimisation of PEALD using silver oxide

According to Allen [16], the optimisation of Ag_xO Schottky contacts can be achieved by observing the appearance. It was determined, from experiments, that observation of an opaque yellow/brown tinge provided the best results. Similar experiments were performed here by fixing the deposition pressure at ~ 4×10^{-3} mbar and varying the ratio of Ar/O_2 flow rates between 1.3/0.2 sccm to 1/1 sccm with a fixed RF power of 45 W. Fig. 6.4 shows the effect of increasing the O_2 flow rate during sputtering, where it was identified that a flow rate ratio of 1/0.8 to 1/1 sccm gives a semi-transparent yellow/brown appearance.

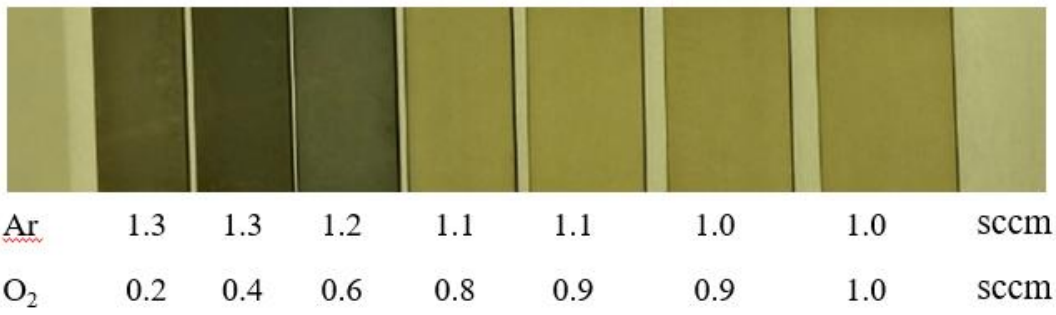

Fig. 6.4 Effect on appearance of increasing O_2 flow rate in RF sputtered Ag films

Ag_xO Schottky contacts were deposited with an Ar/O_2 flow rate of 1/1 sccm onto PEALD ZnO thin-films with various deposition conditions. The deposition conditions of the ZnO were varied, including substrate temperature and plasma time. Initially the substrate temperature was investigated with a constant plasma time of 5 s and the temperatures tested were 80, 100

and 120 °C. The *J-V* characteristics for the best device for each deposition temperature are given in Fig. 6.1(a). It is evident in Fig. 6.1(a) that reducing the deposition temperature serves to reduce both the forward and reverse currents, indicative of a reduction in the carrier concentration [22]. This can be explained by the increasing barrier height as shown in Table 6.1, as the energy difference between the Fermi-level and conduction band is increased. The corresponding device parameters are given in Table 6.1and shows that the effect of lowering the deposition temperature is to improve both ϕ_B and η due to a lower effective net doping density which is further explained in the capacitance-voltage analysis.

Further optimisation of PEALD ZnO Schottky diodes was investigated by increasing the plasma time from 30 to 70 s with a deposition temperature of 80 °C. Fig. 6.1(b) shows results for O_2 plasma times of 30, 50 and 70 s. Good diode behaviour is observed with large rectification ratios > 10^5 and ϕ_B ranging between 0.8 and 0.83 eV. It is shown in Table 6.1 that by increasing the plasma time from 30 to 50 s, the η is improved from 1.46 to 1.33. However, as the plasma time is further increased to 70 s, η degrades to 1.47. Ideality factors for all measured Schottky diodes are large compared with typical diodes that follow thermionic emission (η = 1 – 1.1). However, Werner *et al.* [23] demonstrated that grain boundaries can introduce inhomogeneities at the semiconductor-metal interface. For ZnO Schottky diodes, von Wenckstern *et al.* [8] showed that, for grain sizes ~ 100 nm, thermionic emission remains valid for ideality factors ~ 1.5 in accordance with the proposal of Werner *et al.* [23]. Validation of thermionic emission as the dominant conduction mechanism will be discussed in the next section.

Table 6.1 *J-V* characteristics of the mean PEALD Schottky diodes with different deposition conditions using Ag_xO as the contact. The mean was determined from 5 devices

Deposition temperature (°C)	**O_2 Plasma time (s)**	**Rectification ratio ± 1V**	η	$\phi_{B,\,J\text{-}V}$ **(eV)**
80		7.5×10^4	1.42	0.82
100	**5**	2.2×10^5	1.47	0.80
120		8.7×10^4	1.59	0.76
	30	1.6×10^5	1.46	0.82
80	**50**	3.1×10^5	1.33	0.80
	70	4.1×10^5	1.47	0.83

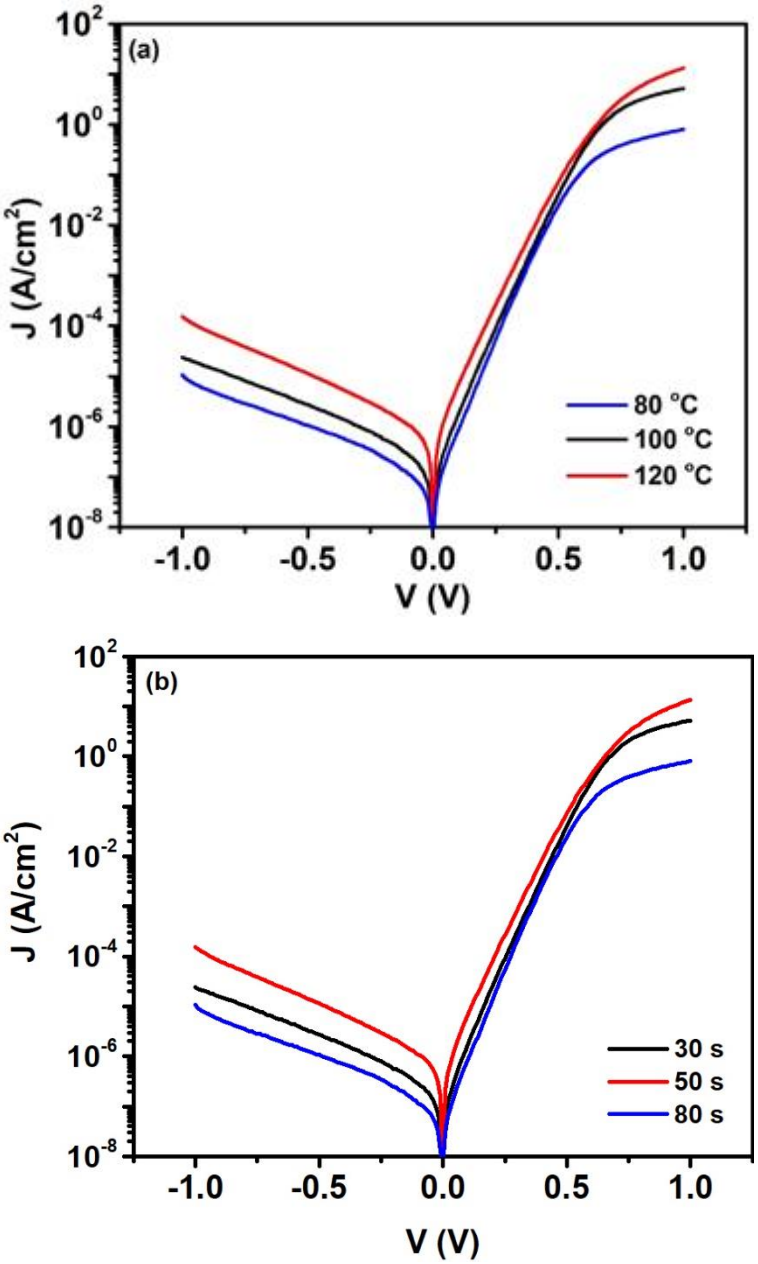

Fig. 6.5 *J-V* characteristics of Ag_xO Schottky contact with different deposition conditions (a) constant O_2 plasma time of 5 s, with and deposition temperatures 80, 100 and 120 ^oC and (b) fixed deposition temperature of 80 ^oC with O_2 plasma times of 30, 50 and 70 s

Interestingly, a wide range of barrier heights have been quoted for Ag/ZnO Schottky interfaces ranging from as low as 0.7 eV to 1.2 eV [6, 9, 11, 16, 19, 24-26]. Several factors have been given for the large variation in obtained values from crystal orientation of the ZnO, Zn- or O-plane [16, 19], device structure (vertical or horizontal) [16], various deposition methods and surface treatment prior to Ag deposition [6, 9, 11, 25]. Typically for Ag contacts on Zn-polar faces achieve greater barrier heights than O-polar faces by approximately 0.1-0.2 eV, due to Fermi-level pinning [19]. This is due to the O-polar ZnO containing a large density of interface states, as the exposed surface is more sensitive to oxygen. For these PEALD ZnO

films, the final deposition layer is an O_2 plasma layer resulting in an O-polar face which may account for the relatively low $\phi_{B,\ J\text{-}V}$. It is worth noting that the act of annealing caused degradation of the ideality factor and an increase in the reverse bias current. Similar effects have been reported by Frenzel *et al.* [9] where annealing above 150 ^oC was seen to cause irreversible degradation of the ideality factor and barrier height. It is believed that annealing above 140 ^oC causes the silver to diffuse into the ZnO layer which degrades the film by effectively increasing the conductivity, resulting in ohmic behaviour of the diode.

The reproducibly of the diodes using Ag_xO was tested by measuring 5 devices fabricated under the same processing conditions and η and ϕ_B were analysed for each device. Fig. 6.6 shows the average barrier height and ideality factors for each deposition condition, with the standard deviation indicated by the error bars. It is evident that for all deposition conditions, small standard deviations are achieved demonstrating good device reproducibility and film uniformity. Moreover, it is apparent that a deposition temperature of 80 ^oC and O_2 plasma time of 50 s produces the most consistent devices due to the lowest standard deviation of 0.014 and 4.4 meV for the ideality factor and barrier height respectively. However, further investigation into the effect of increasing the plasma time for 100 and 120 ^oC films will be required to confirm the good characteristics for PEALD ZnO deposited at 80 ^oC with a plasma time of 50 s.

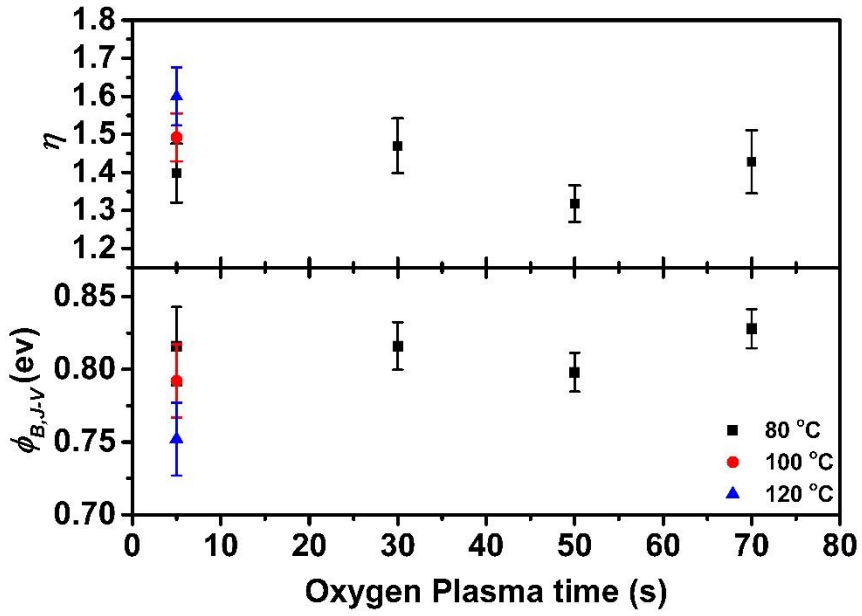

Fig. 6.6 The effect of barrier height and ideality factor for ZnO Schottky diodes with different deposition conditions, indicating 3 standard deviations as the error bars

6.5.1 Capacitance-voltage measurements

Capacitance-voltage measurements were performed on the devices given in Table 6.1 to obtain the $\phi_{B,\,C\text{-}V}$ and net doping density (N_{dep}). The voltage dependent depletion capacitance of a Schottky diode is expressed as:

$$C = \sqrt{\frac{q\varepsilon_o\varepsilon_s N_{dep}}{2V}}A \tag{6.3}$$

where ε_o is the permittivity of free space, ε_s is the dielectric constant for ZnO assumed to be 8.5 [27] and A is the device area. The net doping density can be obtained by plotting A^2/C^2 against V and using:

$$\frac{A^2}{C^2} = \left(\frac{2}{q\varepsilon_o\varepsilon_s N_{dep}}\right)^{1/2}\left(V_{bi} - \frac{kT}{q} - V\right) \tag{6.4}$$

where V_{bi} is the built-in potential. The gradient of the line allows a value for N_{dep} to be obtained. It should be noted that N_{dep} does not solely correspond to the free charge density in the film; instead a combination of the free carriers and the ionised deep level traps. The intercept with the x-axis gives V_{bi}. The barrier height is given by $\phi_{B,\,C\text{-}V} = V_{bi} + kT/q + V_i$, where V_i is the difference between the Fermi-level and conduction band, defined as $V_t \ln\left(N_C/N_{dep}\right)$, where N_c is the density of states within the conduction band, theoretically calculated to be 2.9×10^{18} cm^{-3}, using the effective mass of an electron $0.27m_e$ for ZnO [28]. Strictly speaking, to calculate V_i the free electron concentration (N_e) is required rather than N_{dep}. However, as this is unknown for these films, N_{dep} is used which will underestimate $\phi_{B,\,C\text{-}V}$ as $N_{dep} > N_e$. The C-V characteristics for increasing deposition temperature and plasma times are given in Fig. 6.7(a) and (b) respectively.

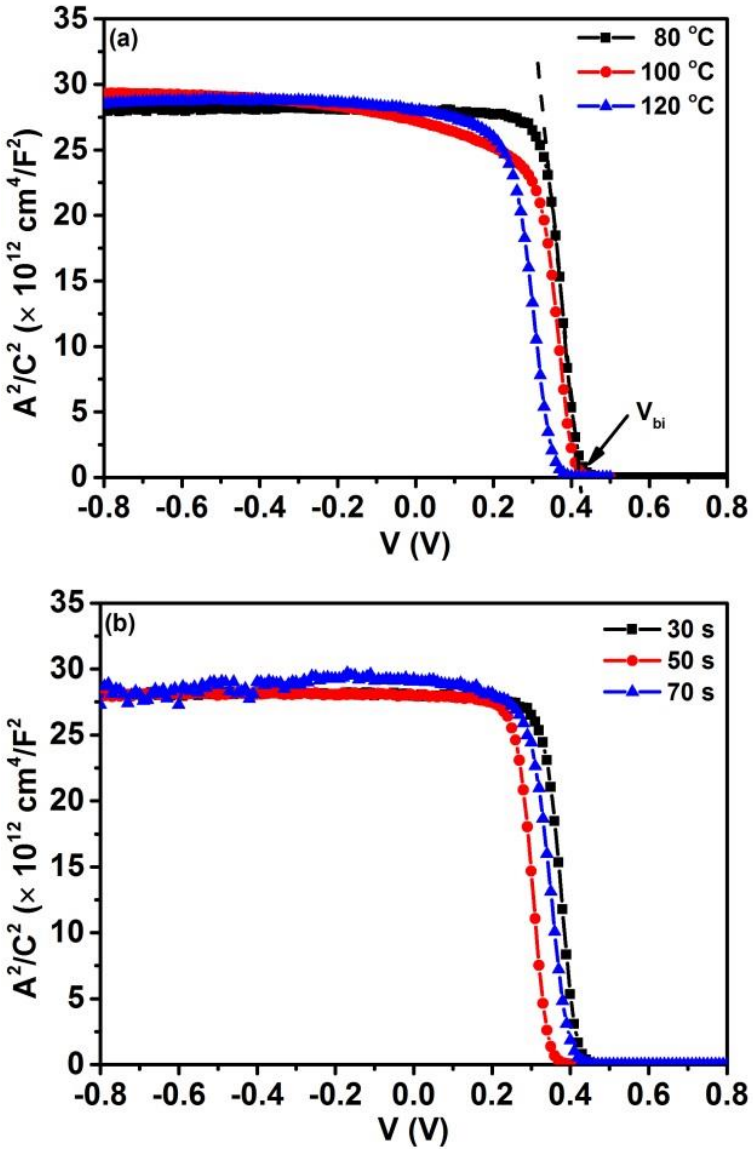

Fig. 6.7 *C-V* characteristics for Ag_xO Schottky diodes with different PEALD deposition conditions (a) constant plasma time of 5 s and deposition temperatures of 80, 100 and 120 °C and (b) deposition temperature of 80 °C with increased plasma times of 30, 50 and 70 s

For all *C-V* characteristics shown in Fig. 6.7(a) and (b), for large negative voltages, the curves are flat demonstrating that the ZnO films are fully depleted. The net doping density, N_{dep} is estimated from the steepest gradient and is highlighted by the dashed line in Fig. 6.7(a) for the 80 °C characteristic. As the deposition temperature is reduced from 120 to 80 °C, N_{dep} is reduced from 5.2 to 1.8 × 10^{17} cm^{-3} as shown in Table 6.2. This reduction is indicative of PEALD ZnO films deposited at lower temperatures. The effect of increasing the O_2 plasma time serves to further decrease N_{dep} to 3.9 × 10^{16} cm^{-3} with a plasma time of 70 s. However, a slight increase is observed in N_{dep} with a plasma time of 50 s, which relates to the slight increase in *J-V* characteristics for this deposition condition shown in Fig. 6.5(b). Incidecently, by using Eqn. (2.11) and the worst case N_{dep} it can be determined that the factor

that predicts the conduction mechanism (E_{00}) is 1×10^{-24} which is less than kT. Hence the valid assumption that thermionic emission is the dominant, conduction mechanism in these Schottky diodes. The extraction of the built-in potential, V_{bi} is indicated in Fig. 6.7(b) and is given in Table 6.2. There is a small lateral shift in V_{bi} observed in Fig. 6.7(a) as an effect of reducing the deposition temperature. Comparing $\phi_{B,\,J\text{-}V}$ and $\phi_{B,\,C\text{-}V}$ in Table 6.2 however, it is evident that for all the measured diodes, $\phi_{B,\,C\text{-}V}$ is smaller by 0.27 - 0.33 meV. However, a more appropriate estimate for ϕ_B would be to use N_e which can be estimated from the series resistance of a diode. By examining the best performing diode with a deposition temperature of 80 ^{o}C and plasma time of 50 s, a R_s of 721 Ω is calculated. Using a nominal electron mobility of 10 cm^2/Vs, $N_e = 8 \times 10^{14}$ cm^{-3} which results in a $V_i = 0.22$ eV. Therefore, $\phi_{B,\,C\text{-}V} = 0.59$ eV, approximately 20 meV lower than *J-V* estimates. Interestingly this effect has been reported for Ag_xO contacts on vertical bulk ZnO Schottky diodes [16]. This is probably due to the formation of interfacial dipoles from hydroxide bonds on the ZnO interface. The metal oxide forming a Schottky contact is likely to involve the dehydrogenation of the hydroxide, hence creating an interfacial layer of metal oxide bonds. This explanation has been used for vertical PEDOT:PSS/ZnO Schottky diodes by Nakano *et al.* [29], although further work is required to confirm the cause for the PEALD ZnO reported here.

Table 6.2 The average extracted parameters from *C-V* measurements for Ag_xO PEALD ZnO Schottky diodes with various ZnO deposition conditions. 5 devices were measured per deposition condition

Deposition temperature (^{o}C)	**O_2Plasma time (s)**	**V_{bi} (V)**	**$\Phi_{B,\,C\text{-}V}$ (eV)**	**N_{dep} (cm^{-3})**
80		0.41	0.45	1.8×10^{17}
100	**5**	0.40	0.50	2.2×10^{17}
120		0.35	0.49	5.2×10^{17}
	30	0.42	0.54	5.9×10^{16}
80	**50**	0.37	0.47	6.8×10^{16}
	70	0.39	0.53	3.9×10^{16}

6.5.2 X-ray photoelectron spectroscopy

The effect of O_2 plasma time on the composition of the PEALD was investigated using XPS due to the better Schottky characteristics as shown in Fig. 6.5 and Table 6.1. ZnO films with a thickness ~ 20 nm were deposited on glass substrates; the measurement details can be found in section 4.2.2. The obtained O 1s core level spectra for ZnO samples are shown in Fig. 6.8(a)-(c), where two sub-peaks are used to fit the spectra. The lower binding energy sub-peak occurs at 529, 530 and 530.5 eV for a plasma time of 30, 50 and 70 s respectively

and is related to Zn-O bonding. The higher binding energy sub-peak of 532 eV has been shown to be associated with O-H bonds in ZnO films [30-32]. The ratio between Zn-O and O-H sub-peaks were calculated to be 0.43, 0.34 and 0.46 for O_2 plasma times of 30, 50 and 70 s. Interestingly studies by Kwon *et al*. [33] and Huby *et al*. [34] have shown that the ratio O-H bonds are inversely proportional with carrier concentration in ZnO films and can explain the formation of trap sites due to interstitials O-H [33]. Therefore, this may explain a correlation between the observed N_{dep} shown in Table 6.2 and the O-H bond ratio for different O_2 plasma times.

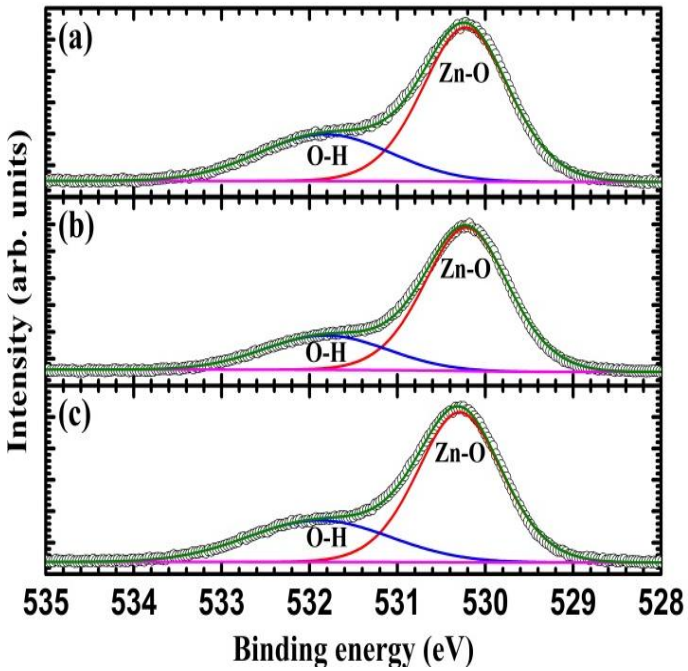

Fig. 6.8 O 1s spectra for PEALD ZnO films deposited at 80 ^oC with plasma times of (a) 30, (b) 50 and (c) 70 s

6.5.3 X-ray diffraction

X-ray diffraction (XRD) measurements were performed to determine the effect of O_2 plasma time on the crystallographic nature of the ZnO films. The experimental details are provided in section 4.2.2. The XRD pattern is given in Fig. 6.9, where it is evident that there are two dominant peaks representing (100) and (002) crystal orientations. The FWHM for the (100) and (002) are 0.401 and 0.381 respectively indicating that growth in the (002) plane is slightly more dominant than (100). Using the Scherrer Eqn. (3.11), an average grain size of 25.6 nm is estimated for this film deposited at 80 ^oC with a 50 s O_2 plasma time.

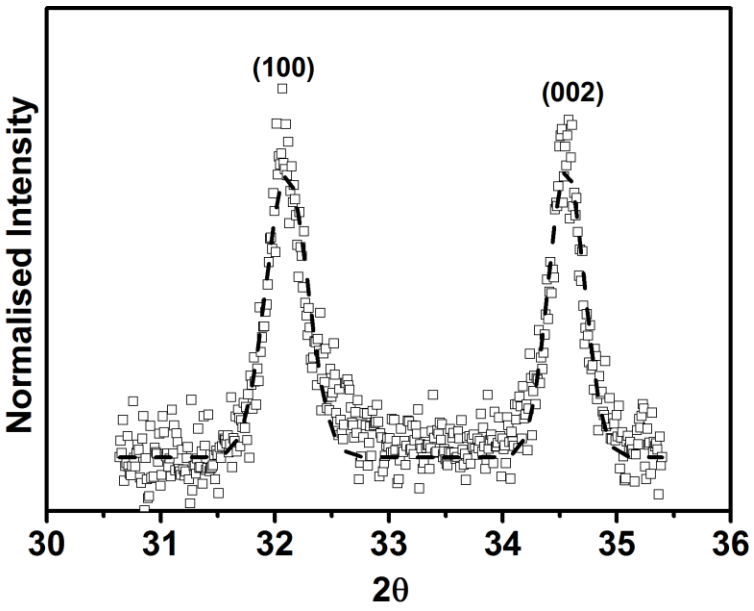

Fig. 6.9 XRD pattern of 80 °C PEALD with a plasma time of 50 s, where the dashed lines are the fitted peaks for to calculate the FWHM

6.6. Platinum oxide

As outlined in the introduction, platinum is widely used as Schottky contact in ZnO based diodes. The same principle to Ag_xO will be investigated to fabricate lightly oxidised platinum (PtO_x) Schottky contacts and compared with Ag_xO. The PtO_x contacts were deposited on 80 nm 80 °C PEALD ZnO with a plasma time of 50 s. The PtO_x was deposited to a nominal thickness of 40 nm via RF sputtering, using a pure Pt target (99.9 %, Kurt J. Lesker) with an RF power of 73.5 W and Ar/O_2 flow rate of 1/1 sccm. A Pt capping layer was subsequently deposited to a thickness of 30 nm. The typical *J-V* characteristics of a PtO_x Schottky diode are shown in Fig. 6.10(a), demonstrating good diode behaviour. The PtO_x diode has a low off-current, a large rectification ratio of 1.3×10^7 at ± 1 V, $\eta = 1.33$ and $\phi_B = 0.83$ eV. Although improved in comparison with Ag_xO contacts, the relatively large η is again explained by contact inhomogeneities as a result of the nano-crystalline nature of the PEALD thin-film as indicated in Fig. 6.9. It is evident that the ideality factor and barrier heights have small standard deviations of 0.03 and 0.02 respectively. The collated results from *J-V* characteristics for all measured PtO_x contacts on the sample are shown in Table 6.3 demonstrating insignificant variation across the sample in the extracted *J-V* characteristics. The series resistance (R_s) was extrapolated in the usual manner, whereby the exponential region is extrapolated to higher currents to find the deviation in voltage (ΔV) for given values of current. Fig. 6.10(b) shows ΔV against I and taking the slope gives R_s. The variation in R_s is shown in Table 6.3, with an average of 1.2 ± 0.51 kΩ. This range of R_s can be attributed to either inhomogeneities in the ZnO/PtO_x interface or the over oxidation of the PtO_x increasing the resistance of the Schottky contact. Furthermore, as there is insignificant variation in the ideality factor and barrier height,

inhomogeneity at the ZnO/PtO_x interface is unlikely to cause this wide variation in R_s but cannot be ruled out without further investigation.

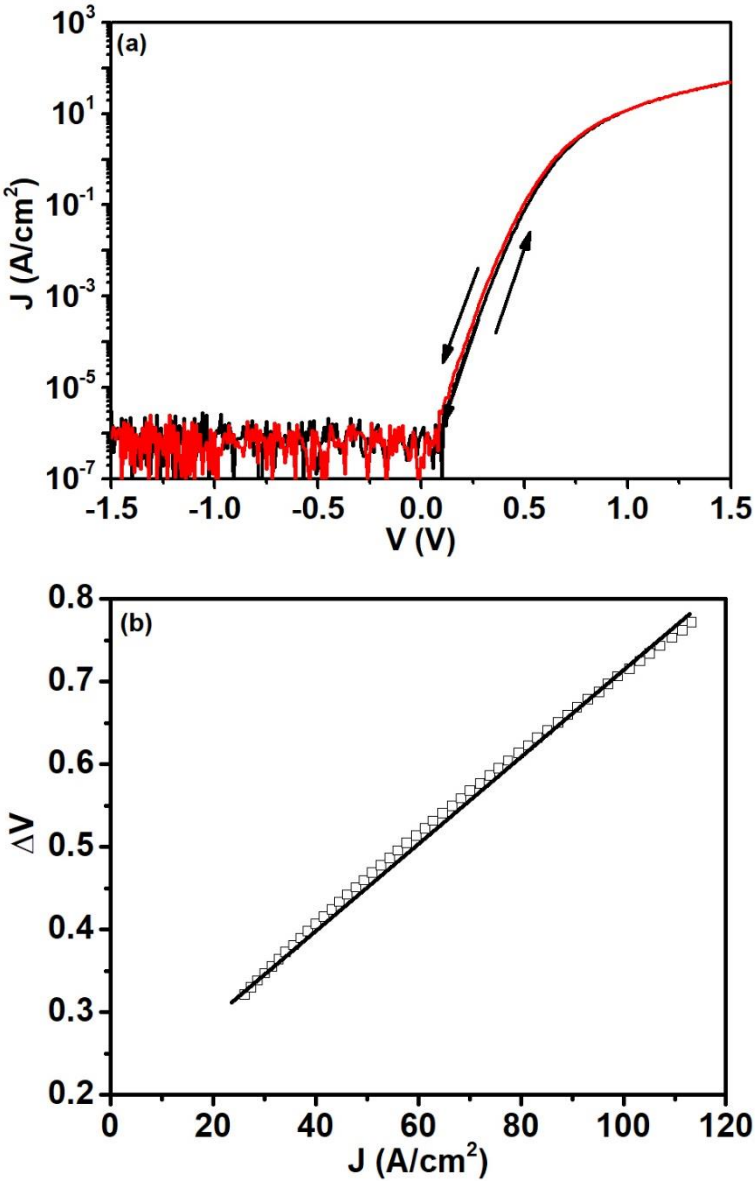

Fig. 6.10 (a) Typical *J-V* characteristics of a Pt_xO Schottky contact (b) extraction technique for R_s, where R_s = 820 Ω

The *C-V* characteristics over the frequency range of 10 kHz, 100 kHz and 1 MHz for the best performing PtO_x Schottky diode are given in Fig. 6.11. The reverse characteristics demonstrate a constant capacitance for a bias less than −0.2 V indicating that the ZnO film is fully depleted. By using the 10 kHz curve and taking the steepest gradient, an average effective carrier concentration of $N_{dep} = 2.8 \times 10^{16}$ cm^{-3} is obtained. From the resulting intercept with the *x*-axis V_{bi} = 0.27 V and hence a value of ϕ_B = 0.42 eV is determined. The extracted results from *C-V* for all measured devices are given in Table 6.3. It is evident from Table 6.3 that there is a large variation in the ϕ_B values obtained from *J-V* and *C-V* characteristics, where

$\phi_{B.\ J\text{-}V} > \phi_{B.C\text{-}V}$ by approximately 0.41 eV. This was observed for vertical oxidised metal Schottky diodes on bulk hydrothermal O-polar face of ZnO by Allen [16]. The formation of an interface dipole, due to the polarisation of chemical bonding of the metal oxide and ZnO interface, may explain the difference between $\phi_{B.\ J\text{-}V}$ and $\phi_{B.C\text{-}V}$. However, a more appropriate estimate for $\phi_{B.C\text{-}V}$ is to use an estimate for the free carrier concentration, N_e in calculating V_i. An estimate for N_e is obtained from R_s by using a nominal mobility of 10 cm^2/Vs. A value of $N_e = 8 \times 10^{13}$ cm^{-3} is then estimated, resulting in a value of $\phi_{B.C\text{-}V} \sim 0.6$ eV, approximately 0.2 eV lower than that found from *J-V* measurements. The same difference was reported by Allen [16]. By comparing the PEALD Schottky diodes with Ag_xO and PtO_x contacts, it is evident that similar ideality factors and barrier heights are obtained. However, an improvement in the off-state current by at least an order of magnitude is observed in the PtO_x diode at – 1 V shown in Fig. 6.10(a). The on-state current is comparable for the diode with the same deposition condition (temperate = 80 ^oC, O_2 plasma time = 50 s) as shown in Fig. 6.5(b).

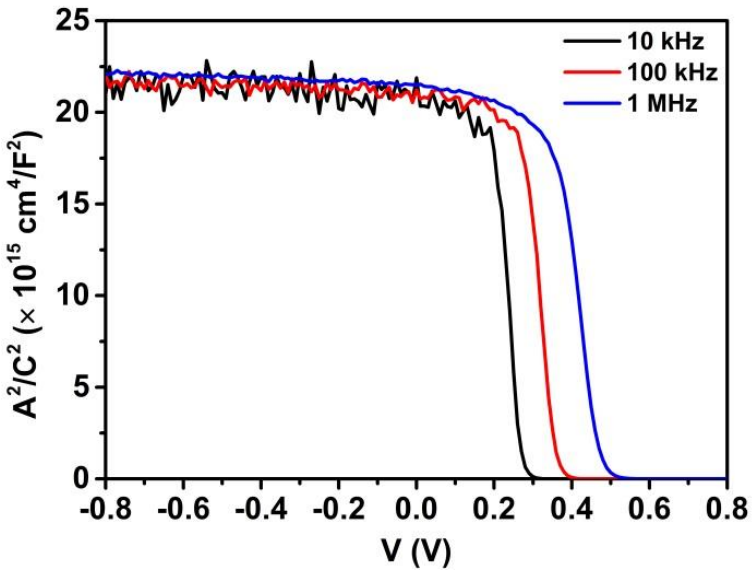

Fig. 6.11 A^2/C^2 versus V for the PtO_x Schottky diode for the frequencies 10, 100 kHz and 1 MHz

Table 6.3 Schottky characteristics obtained from *J-V* and *C-V* measurements on 80 nm PEALD ZnO with PtO_x

Device Number	***Rectification ratio* ± 1 V**	***η***	**$\phi_{B,\ J\text{-}V}$ (eV)**	**$\phi_{B,\ C\text{-}V}$ (eV)**	**R_s (kΩ)**	**N_{dep} (cm^{-3})**
1	1.0×10^7	1.37	0.84	0.40	0.71	7.6×10^{16}
2	1.3×10^7	1.32	0.82	0.43	1.54	2.8×10^{16}
3	1.3×10^7	1.32	0.80	0.42	0.82	5.0×10^{16}
4	1.8×10^7	1.41	0.85	0.44	1.76	9.7×10^{15}
5	2.1×10^7	1.34	0.80	0.44	1.10	1.0×10^{16}
6	7.8×10^6	1.35	0.81	0.44	1.06	9.4×10^{16}
7	8.0×10^6	1.42	0.85	0.44	1.05	1.2×10^{16}
	1.2×10^7 ± 0.2	1.36 ± 0.04	0.83 ± 0.03	0.42 ± 0.02	1.20 ± 0.51	2.8×10^{16} ± 2.0

6.6.1 Alternative extraction methods for PtO_x contacts

The barrier height $\phi_{B,J\text{-}V}$ above, was extracted from a method outlined by Rhoderick *et al.* [20] which removes the dependence of small variations in calculating J_o. Two widely utilised extraction techniques were developed by Norde *et al.* [35] and by Cheung and Cheung [36] based the on voltage and current dependent functions respectively. The advantage of the use of these techniques is that it enables accurate determination of potentially large R_s.

For Schottky diodes with a large series resistance, Norde's method developed in 1970s is a favoured technique to obtain both R_s and ϕ_B [35]. This technique is advantageous for small linear regions in a log-lin plot, where potentially a large error in determining J_o is observed. Norde uses the function:

$$F(V) = \frac{V}{2} - \frac{kT}{q}\ln\left(\frac{I}{AA^*T^2}\right) \tag{6.5}$$

where it can be shown that for the ideal case ($R_s = 0$), a straight line with a gradient of − ½ and the intercept is ϕ_B, whereas if R_s is large, a gradient of ½ is obtained [35]. As R_s varies between the extremes, the lines approach a minimum. This minimum corresponds to the solution for both ϕ_B and R_s using the following equations:

$$\phi_B = F(V_{\min}) + \frac{V_{\min}}{2} - \frac{kT}{q} \tag{6.6}$$

$$R_s = \frac{kT}{qI_o} \tag{6.7}$$

where $F(V_{min})$ is the minima of the function $F(V)$, V_{min} and I_o is the corresponding voltage and current respectively. However, as these Schottky diodes are non-ideal the method by Sato *et al*. [37] to account for ideality factors greater than 1.2 is adopted. Therefore, Eqns. (6.6) and (6.7) are modified to the following:

$$\phi_B = F(V_{\min}) + \left(\frac{1}{\eta} - \frac{1}{\gamma}\right)V_{\min} - \left(\frac{\eta}{\gamma} - 1\right)\frac{kT}{q} \tag{6.8}$$

$$R_s = \frac{kT(\gamma - \eta)}{qI_o} \tag{6.9}$$

where γ is the nearest integer to η (e.g. η = 1.5 then γ = 2). An example plot of $F(V)$ against V, is shown in Fig. 6.12 depicting the general shape obtained and point of which $F(V_{min})$ and V_{min} are determined. It is worth noting that the extraction of R_s through the modified Norde's method by Sato *et al*. [37] will not be analysed. This due to measurements at two temperatures being required to accurately determine R_s.

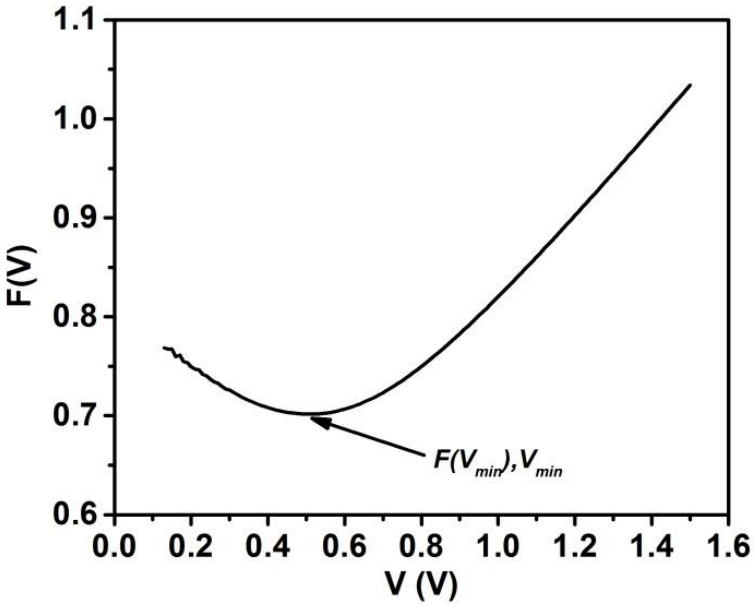

Fig. 6.12 Plot of $F(V)$ against V for PtO_x Schottky diodes used in the extraction of ϕ_B and R_s using Norde's methods

Another method for determining R_s developed in 1980s by Cheung and Cheung, uses two current dependent functions which can also be used to extract η and ϕ_B [36]. Cheung's method requires the rearrangement of Eqn. (6.1) to find V and is given as:

$$V = R_s AJ + \eta\phi_B - \frac{\eta kT}{q}\ln\left(\frac{J}{A^* T^2}\right) \tag{6.10}$$

The first function employed by Cheung's method is obtained by differentiating Eqn. (6.10) with respect with J and gives:

$$\frac{dV}{d\ln(J)} = R_s AJ + \frac{\eta kT}{q} \tag{6.11}$$

By plotting $dV/d\ln(J)$ against J, R_s is obtained from the gradient and η from the intercept with the y-axis. As η has been identified the second function $H(J)$ is calculated and is given by:

$$H(J) = V - \frac{\eta kT}{q}\ln\left(\frac{J}{A^* T^2}\right) \tag{6.12}$$

and by combining Eqns. (6.10) and (6.12)

$$H(J) = RAJ + \eta\phi_B \tag{6.13}$$

Plotting, $H(J)$ against J a straight line is obtained with R_s dependent on the gradient and ϕ_B with the y-axis intercept. Fig. 6.13 shows the plots $dV/d\ln(J)$ against J and $H(J)$ against J used in Cheung's method. In both Fig. 6.13(a) and (b), the dashed red line indicated the region where the gradient and intercepts are selected to extract R_s, η and ϕ_B. It is worth noting that in Fig. 6.13(a), there is large fluctuation in the region where the gradient is taken, and this increases the possibility of variation in the exact solution of the y-axis. This may lead to large irregularities between η obtained from the different techniques.

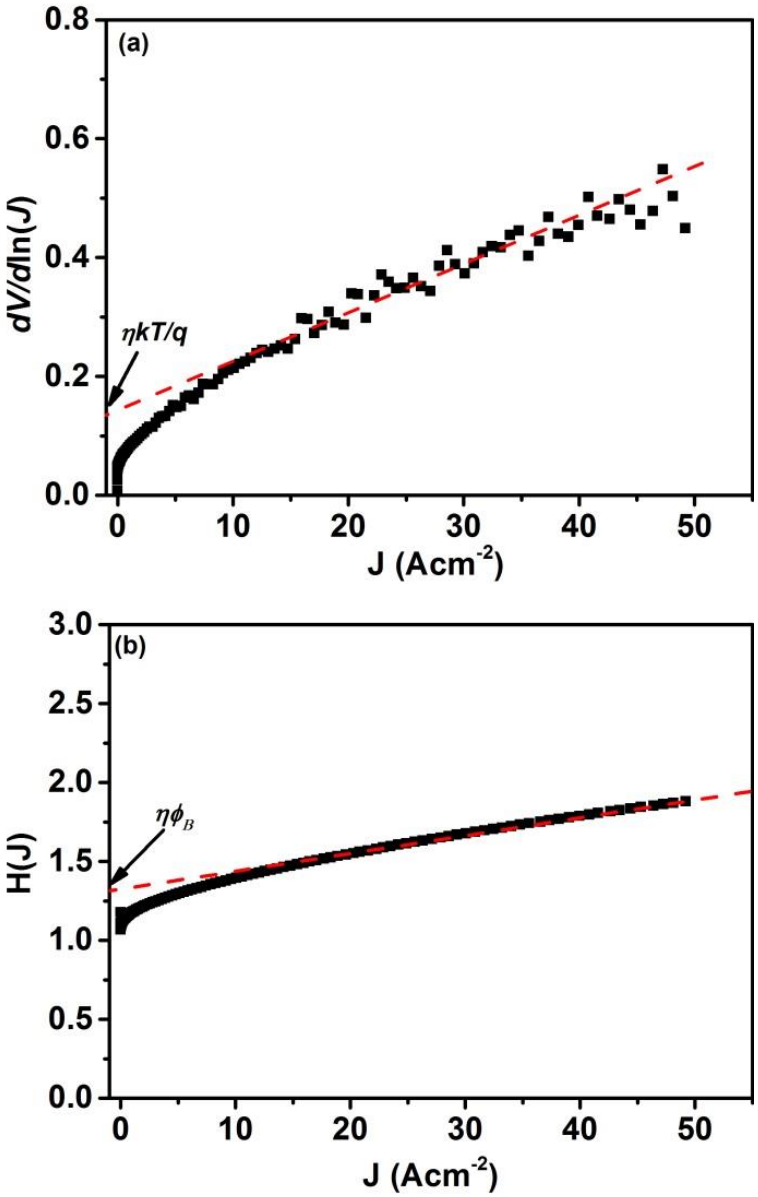

Fig. 6.13 Cheung's method plots (a) *dV/d*ln*(J)* and (b) *H(J)* indicating the regions where η and ϕ_B are extracted

A comparison between the extraction methods outlined for PEALD ZnO Schottky diodes with PtO_x contacts are given in Table 6.4, where the original results from Table 6.4 are included for ease of comparison. Firstly, the standard method and that of Rhoderick's show very good agreement with respect to η and ϕ_B. Rhoderick's method gives a slightly larger estimation of barrier height which is due to the reduction of measurement error in comparison to the standard method, especially for non-ideal Schottky diodes where there is a small linear region in the log-linear *J-V* characteristics, hence increasing the error for J_o. As outlined above, Rhoderick's method suffers from an increase in this measurement error. Norde's method demonstrates accurate estimation of ϕ_B in-line with the standard and Rhoderick's methods.

The parameters extracted from both approaches of Cheung's methods *dV/dln(J)* and *H(J)* are given in Table 6.4. From *dV/dln(J)* plots, the calculated R_s is consistently lower than that obtained from the standard method by approximately 20 %. Although different, the 20 % difference may arise due to the variation observed in the high current density region as shown in Fig. 6.13(a). Moreover, the ideality factor calculated by this method is 4 times larger than the standard and Rhoderick's method, as η is calculated under higher potentials which is dominated by the large series resistance. Instead of using η from Cheung's method for the calculation of *H(J)* in Eqn. (6.12), the ideality factor from standard analysis is utilised. From this method (*H(J)*) the parameterised R_s is close to the measured series resistance from the standard measurements. However, ϕ_B experiences 17 % higher values than standard and Rhoderick's method.

From this comparative investigation there are slight differences in the extracted parameters, notably R_s and η from Norde's and Cheung's method respectively. The higher than unity ideality demonstrates the difficulty in Norde's method, hence Sato *et al.* [37] approach is employed. However, without the second measurement at a different temperature it is no longer possible to determine the series resistance effectively. Conversely both of Cheung's plots are effective for extracting the series resistance as it is found from linear regression over a large current range. However, as the R_s is calculated from the high current region, the ideality factor is sensitive to small variations in R_s from *dV/dln(J)* vs. *J*. The latter demonstrates the unsuitability of Cheung's technique for extracting the ideality factor. Therefore, a combination of techniques results in an effective self-consistent verification method for validating the Schottky parameters using thermionic emission theory. These limitations in Schottky diode analysis for high series resistance was identified by Aubry and Meyer [38]. where it was identified that a combination of methods is preferred to reduce the uncertainty especially for large R_s diodes. The average Schottky parameters for PtO_x on PEALD ZnO are; η = 1.36, ϕ_B = 0.83 eV and R_s = 1.15 kΩ. The large R_s may arise from the ~ 20 nm PtO_x layer, where oxygen surface treatment could provide lower R_s. In general, the ideality factor and series resistance are non-ideal, however, present promising results for PLEAD ZnO Schottky diodes.

Table 6.4 A comparative study between the extracted Schottky parameters using the standard, Rhoderick's, Norde's and Cheung's methods where for Cheung's *H(J)* function η from the standard method was used

Device	**Standard method**			**Rhoderick's method**			**Norde's method**			**Chueng's method** *[dV/d*ln(*J*)*]*			**Chueng's method** *[H(J)]*		
	η	$\phi_{B,\ J\text{-}V}$ (eV)	R_s (kΩ)	η	$\phi_{B,\ J\text{-}V}$ (eV)	R_s (kΩ)	η	$\phi_{B,\ J\text{-}V}$ (eV)	R_s (kΩ)	η	$\phi_{B,\ J\text{-}V}$ (eV)	R_s (kΩ)	η	$\phi_{B,\ J\text{-}V}$ (eV)	R_s (kΩ)
1	1.37	0.79	0.71	1.38	0.84	--	--	0.68	--	4.84	--	0.54	--	0.93	0.72
2	1.32	0.81	1.54	1.33	0.82	--	--	0.70	--	4.16	--	1.38	--	0.96	1.60
3	1.32	0.81	0.82	1.35	0.80	--	--	0.82	--	4.37	--	0.65	--	0.96	0.81
4	1.41	0.79	1.76	1.34	0.85	--	--	0.81	--	5.70	--	1.33	--	0.99	1.91
5	1.34	0.80	1.10	1.34	0.80	--	--	0.82	--	5.23	--	0.84	--	0.98	0.82
6	1.35	0.79	1.06	1.32	0.81	--	--	0.82	--	4.79	--	0.84	--	1.00	1.08
7	1.42	0.79	1.05	1.42	0.85	--	--	0.79	--	5.43	--	0.76	--	0.97	1.04
	1.36 ± 0.04	0.80 ± 0.01	1.15 ± 0.35	1.35 ± 0.03	0.82 ± 0.02	--	--	0.78 ± 0.06	--	4.93 ± 0.52	--	0.91 ± 0.3	--	0.97 ± 0.03	1.04 ± 0.42

6.7. Conclusion

Schottky diodes have been realised on PEALD ZnO using the metal oxides Ag_xO and PtO_x. The effect of varying the deposition temperature and plasma time during the deposition of ZnO was explored, where reducing the temperature to 80 ^oC and a plasma time of 50 s between each cycle provided the best *J-V* characteristics. From *C-V* characteristics, this PEALD deposition condition was seen to reduce the effective carrier concentration below 10^{17} cm^{-3}. This can be explained from a lower O-H ratio in the 1 Os spectra as shown by the XPS analysis, as N_{dep} is inversely proportional to O-H ratios. By using PtO_x, improved Schottky characteristics are achieved with a lower ideality factor and higher barrier presumably due to improve interface homogeneity in comparison with Ag_xO. However, the relative high ideality factors are dependent on the nano-crystalline nature of the PEALD ZnO thin-film. Furthermore, compositional analysis of the oxidised metal contacts and the interface properties of the Schottky contact is required to obtain the optimum metal-oxygen ratio. A comparative study of 5 techniques for the extraction of Schottky characteristics were conducted on the PtO_x devices. A large variation in ideality factor was determined between the Rhoderick's and Cheung's analysis methods which was attributed to the differences in the region of extraction. The barrier height remains constant throughout all techniques demonstrating the effectiveness of extracting this parameter with each analysis method. The standard and Cheung's methods give rise to constant series resistance values. However, Norde's method overestimates R_s as it is highly dependent on the minima in the *F(V)* function, which occurs at low bias's in comparison to the resistive region of the *J-V* characteristics. Overall, neither Norde's or Cheung's method can be used to accurately determine all the Schottky diode parameters but, taken together, can provide a self-consistent method to verify the parameters using the model of thermionic emission.

6.8. References

[1] C. Weichsel, O. Pagni, and A. W. R. Leitch, "Electrical and hydrogen sensing characteristics of Pd/ZnO Schottky diodes grown on GaAs," *Semiconductor Science and Technology,* vol. 20, no. 8, pp. 840-843, 2005.

[2] J. Yu, S. J. Ippolito, W. Wlodarski, M. Strano, and K. Kalantar-zadeh, "Nanorod based Schottky contact gas sensors in reversed bias condition," *Nanotechnology,* vol. 21, no. 26, p. 265502, 2010.

[3] Y. Liu, J. Yu, and P. T. Lai, "Investigation of WO_3/ZnO thin-film heterojunction-based Schottky diodes for H2 gas sensing," *International Journal of Hydrogen Energy,* vol. 39, no. 19, pp. 10313-10319, 2014.

[4] H. Frenzel, A. Lajn, M. Brandt, H. Von Wenckstern, G. Biehne, H. Hochmuth, M. Lorenz, and M. Grundmann, "ZnO metal-semiconductor field-effect transistors with Ag-Schottky gates," *Applied Physics Letters,* vol. 92, no. 19, 2008.

[5] H. Frenzel, M. Lorenz, A. Lajn, H. Von Wenckstern, G. Biehne, H. Hochmuth, and M. Grundmann, "ZnO-based metal-semiconductor field-effect transistors on glass substrates," *Applied Physics Letters,* vol. 95, no. 15, 2009.

[6] H. Sheng, S. Muthukumar, N. W. Emanetoglu, and Y. Lu, "Schottky diode with Ag on $(11\bar{2}0)$ epitaxial ZnO film," *Applied Physics Letters,* vol. 80, no. 12, pp. 2132-2134, 2002.

[7] G. M. Ali, A. D. D. Dwivedi, S. Singh, and P. Chakrabarti, "Interface properties and junction behavior of Pd contact on ZnO thin film grown by vacuum deposition technique," *physica status solidi (c),* vol. 7, no. 2, pp. 252-255, 2010.

[8] H. von Wenckstern, G. Biehne, R. A. Rahman, H. Hochmuth, M. Lorenz, and M. Grundmann, "Mean barrier height of Pd Schottky contacts on ZnO thin films," *Applied Physics Letters,* vol. 88, no. 9, p. 092102, 2006.

[9] H. Frenzel, A. Lajn, H. von Wenckstern, G. Biehne, H. Hochmuth, and M. Grundmann, "ZnO-based metal-semiconductor field-effect transistors with Ag-, Pt-, Pd-, and Au-Schottky gates," *Thin Solid Films,* vol. 518, no. 4, pp. 1119-1123, 2009.

[10] C. Tsiarapas, D. Girginoudi, and N. Georgoulas, "Electrical characteristics of Pd Schottky contacts on ZnO films," *Materials Science in Semiconductor Processing,* vol. 17, pp. 199-206, 2014.

[11] T. A. Krajewski, G. Luka, L. Wachnicki, A. J. Zakrzewski, B. S. Witkowski, M. I. Lukasiewicz, P. Kruszewski, E. Lusakowska, R. Jakiela, M. Godlewski, and E. Guziewicz, "Electrical parameters of ZnO films and ZnO-based junctions obtained by atomic layer deposition," *Semiconductor Science and Technology,* vol. 26, no. 8, p. 085013, 2011.

[12] B. J. Coppa, R. F. Davis, and R. J. Nemanich, "Gold Schottky contacts on oxygen plasma-treated, n-type ZnO(000$\bar{1}$)," *Applied Physics Letters,* vol. 82, no. 3, pp. 400-402, 2003.

[13] A. Klein, F. Säuberlich, B. Späth, T. Schulmeyer, and D. Kraft, "Non-stoichiometry and electronic properties of interfaces," *Journal of Materials Science,* vol. 42, no. 6, pp. 1890-1900, 2007.

[14] M. W. Allen and S. M. Durbin, "Influence of oxygen vacancies on Schottky contacts to ZnO," *Applied Physics Letters,* vol. 92, no. 12, 2008.

[15] M. W. Allen, S. M. Durbin, and J. B. Metson, "Silver oxide Schottky contacts on n-type ZnO," *Applied Physics Letters,* vol. 91, no. 5, 2007.

[16] M. W. Allen, "Schottky Contact Formation to Bulk Zinc Oxide," Doctoral, Electrical Engineering, University of Canterbury, 2008.

[17] A. Lajn, H. Wenckstern, G. Benndorf, C. P. Dietrich, M. Brandt, G. Biehne, H. Hochmuth, M. Lorenz, and M. Grundmann, "Shallow Donors and Compensation in Homoepitaxial ZnO Thin Films," *Journal of Electronic Materials,* Article vol. 39, no. 5, pp. 595-600, 2010.

[18] S. Muller, H. v. Wenckstern, O. Breitenstein, J. Lenzner, and M. Grundmann, "Microscopic Identification of Hot Spots in Multibarrier Schottky Contacts on Pulsed Laser Deposition Grown Zinc Oxide Thin Films," *IEEE Transactions on Electron Devices,* vol. 59, no. 3, pp. 536-541, 2012.

[19] M. W. Allen, M. M. Alkaisi, and S. M. Durbin, "Metal Schottky diodes on Zn-polar and O-polar bulk ZnO," *Applied Physics Letters,* vol. 89, no. 10, 2006.

[20] E. H. Rhoderick and R. H. Williams, *Metal-Semiconductor Contacts*, 2 ed. Oxford: Clarendon Press, 1988.

[21] J. Zhang, H. Yang, Q.-l. Zhang, S. Dong, and J. K. Luo, "Structural, optical, electrical and resistive switching properties of ZnO thin films deposited by thermal and plasma-enhanced atomic layer deposition," *Applied Surface Science*, vol. 282, pp. 390-395, 2013.

[22] E. Guziewicz, M. Godlewski, L. Wachnicki, T. Krajewski, G. Luka, S. Gieraltowska, R. Jakiela, A. Stonert, W. Lisowski, and M. Krawczyk, "ALD grown zinc oxide with controllable electrical properties," *Semiconductor Science and Technology*, vol. 27, no. 7, p. 074011, 2012.

[23] J. H. Werner and H. H. Güttler, "Barrier inhomogeneities at Schottky contacts," *Journal of Applied Physics*, vol. 69, no. 3, pp. 1522-1533, 1991.

[24] M. W. Allen, M. M. Alkaisi, and S. M. Durbin, "Metal Schottky diodes on Zn-polar and O-polar bulk ZnO," *Applied Physics Letters*, vol. 89, no. 10, p. 103520, 2006.

[25] H. Kim, H. Kim, and D.-W. Kim, "Effect of oxygen plasma treatment on the electrical properties in Ag/bulk ZnO Schottky diodes," *Vacuum*, vol. 101, pp. 92-97, 2014.

[26] A. Y. Polyakov, N. B. Smirnov, E. A. Kozhukhova, V. I. Vdovin, K. Ip, Y. W. Heo, D. P. Norton, and S. J. Pearton, "Electrical characteristics of Au and Ag Schottky contacts on n-ZnO," *Applied Physics Letters*, vol. 83, no. 8, pp. 1575-1577, 2003.

[27] T. Hanada, "Basic properties of ZnO, GaN, and related materials," *Oxide and nitride semiconductors*, pp. 1-19, 2009.

[28] M. Shen, A. Afshar, M. Gupta, G. Shoute, K. Cadien, Y. Y. Tsui, and D. Barlage, "Electrical characteristics of TiW/ZnO Schottky contact with ALD and PLD," in *Materials Research Society Symposium Proceedings*, 2014, vol. 1635.

[29] M. Nakano, A. Tsukazaki, R. Y. Gunji, K. Ueno, A. Ohtomo, T. Fukumura, and M. Kawasaki, "Schottky contact on a ZnO (0001) single crystal with conducting polymer," *Applied Physics Letters*, vol. 91, no. 14, 2007.

[30] M. Kunat, S. Gil Girol, T. Becker, U. Burghaus, and C. Wöll, "Stability of the polar surfaces of ZnO: A reinvestigation using He-atom scattering," *Physical Review B - Condensed Matter and Materials Physics*, vol. 66, no. 8, pp. 814021-814023, 2002.

[31] A. Önsten, D. Stoltz, P. Palmgren, S. Yu, M. Göthelid, and U. O. Karlsson, "Water adsorption on znO(0001): Transition from triangular surface structures to a disordered hydroxyl terminated phase," *Journal of Physical Chemistry C,* vol. 114, no. 25, pp. 11157-11161, 2010.

[32] M. W. Allen, D. Y. Zemlyanov, G. I. N. Waterhouse, J. B. Metson, T. D. Veal, C. F. McConville, and S. M. Durbin, "Polarity effects in the x-ray photoemission of ZnO and other wurtzite semiconductors," *Applied Physics Letters,* vol. 98, no. 10, 2011.

[33] J. D. Kwon, J. W. Lee, K. S. Nam, D. H. Kim, Y. Jeong, S. H. Kwon, and J. S. Park, "The impact on in-situ-hydrogen-plasma treatment for zinc oxide plasma enhanced atomic layer deposition," *Current Applied Physics,* vol. 12, no. 2, pp. S134-S138, 2012.

[34] N. Huby, S. Ferrari, E. Guziewicz, M. Godlewski, and V. Osinniy, "Electrical behavior of zinc oxide layers grown by low temperature atomic layer deposition," *Applied Physics Letters,* vol. 92, no. 2, 2008.

[35] H. Norde, "A modified forward I-V plot for Schottky diodes with high series resistance," *Journal of Applied Physics,* vol. 50, no. 7, pp. 5052-5053, 1979.

[36] S. K. Cheung and N. W. Cheung, "Extraction of Schottky diode parameters from forward current-voltage characteristics," *Applied Physics Letters,* vol. 49, no. 2, pp. 85-87, 1986.

[37] K. Sato and Y. Yasumura, "Study of forward I-V plot for Schottky diodes with high series resistance," *Journal of Applied Physics,* vol. 58, no. 9, pp. 3655-3657, 1985.

[38] V. Aubry and F. Meyer, "Schottky diodes with high series resistance: Limitations of forward I-V methods," *Journal of Applied Physics,* Article vol. 76, no. 12, p. 7973, 1994.

Chapter 7

7. Conclusions and future work

7.1. Conclusions

The development of ZnO thin-films deposited by ALD for transparent electronics has been investigated in this thesis, focusing on TFT and Schottky diode applications. Despite the recent success of IGZO and ZnO for these applications, ALD deposited ZnO has eluded the research community due to the inherently conductive films. Two potential solutions to reduce the film conductivity that have been outlined are; substitutional dopants for Zn ions and the use of PEALD.

The use of metals to act as substitutional dopants for Zn ions in the crystal in order to reduce the films conductivity has been successfully demonstrated for TFT applications. This was achieved by altering the ratios between the Zn and dopant precursor during the ALD reaction. It was established that Nb and Mg achieved the desired effect, where using Nb resulted in a lower cycle ratio than Mg to achieve the optimum TFT performance. This is explained by the occurrence of the Nb^{5+} oxidation state compared to Mg^{2+}. Hence, a lower concentration is required to reduce the oxygen vacancies in the ZnO crystal. Furthermore, from PL measurements, a decrease in the peak at 500 eV was observed for small Nb cycle ratios, demonstrating the reduction of oxygen vacancies within the film. Another effect of doping ZnO with Mg and Nb, was to increase the band gap from 3.3 eV to 3.44 and 3.57 eV respectively. This occurs due to an alloying process, whereby the respective oxides are MgO and Nb_2O_5 are formed, which were confirmed from XPS analysis.

TFTs were fabricated on substrates comprising highly doped n-type Si wafers, with 50 nm thermally grown SiO_2 and a thin (5 nm) Al_2O_3 capping layer. The electrical characteristics for Mg and Nb doped ZnO TFTs were both improved with respect to un-doped ALD ZnO. It was established that post-deposition annealing in air at 300 ^oC was key in achieving good transfer and output characteristics. Annealing served to further reduce the conductivity by oxidising the film to remove the oxygen vacancies. Optimum cycle ratios of 7:1 and 25:1 of ZnO:Mg and ZnO:Nb respectively were obtained where similar current *On/off* ratios were achieved (10^8) for devices patterned by photolithography. The saturation mobility was 4 and 7.9 cm^2/Vs for MgZnO and NbZnO respectively. NbZnO exhibited a larger saturation mobility although both films had similar grain sizes. The origin of the higher mobility was explained by the 5s spin orbital of Nb not forming a high density of sub band gap traps close to the conduction band edge.

The current voltage conduction mechanism for these TFTs were examined using a multi-trapping and release model. Electrons are thermally excited and move towards the conduction band before they contribute to the conduction. This model was shown to be valid for MgZnO and NbZnO TFTs, where MgZnO had a large sub-band gap trap density. This steeper sub-threshold slope indicates that Nb acts as a more suitable substitutional dopant which serves to reduce the sub-band gap defects in the ZnO crystal structure and improve the electrical characteristics. Moreover, the sub-band gap trap density for NbZnO was validated through capacitance voltage measurements by analysing the multi-frequency characteristics. The large frequency dispersion was attributed to these bulk trapping states.

ZnO active layers for Schottky applications were deposited by PEALD with a Ti Ohmic contact and the Schottky initially Ag_xO. The effect of the deposition conditions was examined by altering the deposition temperature and plasma time. It was established that increasing the plasma time to 50 s and reducing the deposition temperature to 80 ^oC gave the highest rectification ratio and lowest ideality factor of 1.33. From capacitance analysis, a background doping density (N_{dep}) of 10^{16} cm^{-3} was measured, which is a combination of the free carrier and trap density. Furthermore, a comparative study of Schottky parameter extraction techniques for non-ideal diodes was undertaken on PtO_x diodes. Interestingly, there were inconsistencies between these techniques. The voltage function technique of Norde gave a barrier height consistent with the standard analysis method but overestimated the series resistance. In contrast, the current function technique of Cheung overestimated the ideality factor, but the barrier height and series resistance were self-consistent with standard analysis methods.

In summary, it has been demonstrated that by doping ZnO thin-films with Nb or Mg, good TFT characteristics are be achieved for ALD deposited films. Furthermore, high performance Schottky diodes using PEALD as the active layer have been demonstrated. The work presented in is thesis outlines effectively the potential solutions to reduce the intrinsically high conductivity of ALD ZnO to produce devices with good performance.

7.2. Future Work

The elements of achieving good TFT and Schottky performance has been outlined for ALD based ZnO films without the use of indium or gallium. However, there are a number of key objectives that require addressing before an alternative for IGZO can be effectively suggested.

Although promising TFT characteristics are demonstrated especially for NbZnO, it is essential that TFT structures fabricated with independent gates are studied. Also, by not using Si as the gate electrode, optimisation of the gate and oxide will can be optimised to obtain the ideal

TFT characteristics. Moreover, temperature dependence of *I-V* measurements will further enable the validation of the MTR model as the power is temperature dependent. Once the *I-V* theory is validated, a SPICE model can be established to investigate the potential applications for these TFTs.

Before potential Schottky applications are identified an understanding of the oxidised metal contacts requires further investigation. The question remains, as to whether the oxygen ratio is optimised for the studied Ag and Pt. Once these Schottky contacts are fully optimised, alternative contacts with large work functions such as Au, Pd or Ir will be investigated. Furthermore, the use of temperature dependent measurements is required to confirm the origin of the ideality factors, which are proposed to originate from grain boundaries at the interface giving rise to a distribution of barrier heights across the device. Once fully optimised, a metal-semiconductor field effect transistor (MESFET) can be considered. The advantage of using MESFETs compared to TFTs is the fewer required processing steps and lower operating voltage, resulting in potentially lower cost electronic devices for transparent applications.

Appendix

8. Appendix A

The core level spectra of interfacial measurements for bulk SiO_2, ZnO/SiO_2 and $MgZnO/SiO_2$ interfaces are given in the following figures respectively.

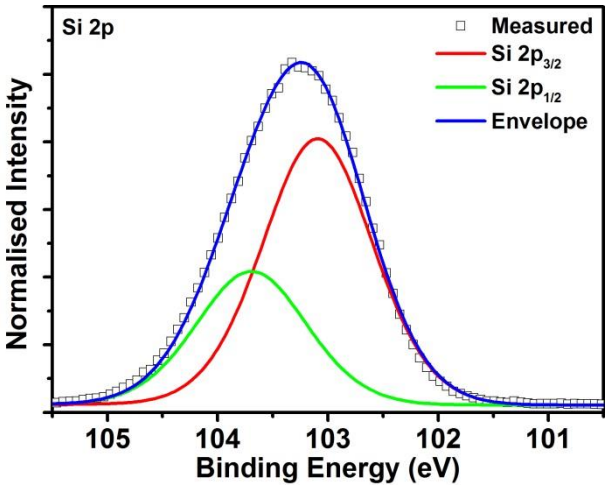

Fig. A.1 Si 2p core level spectra for bulk (50 nm) SiO_2 on Si, showing the fitted

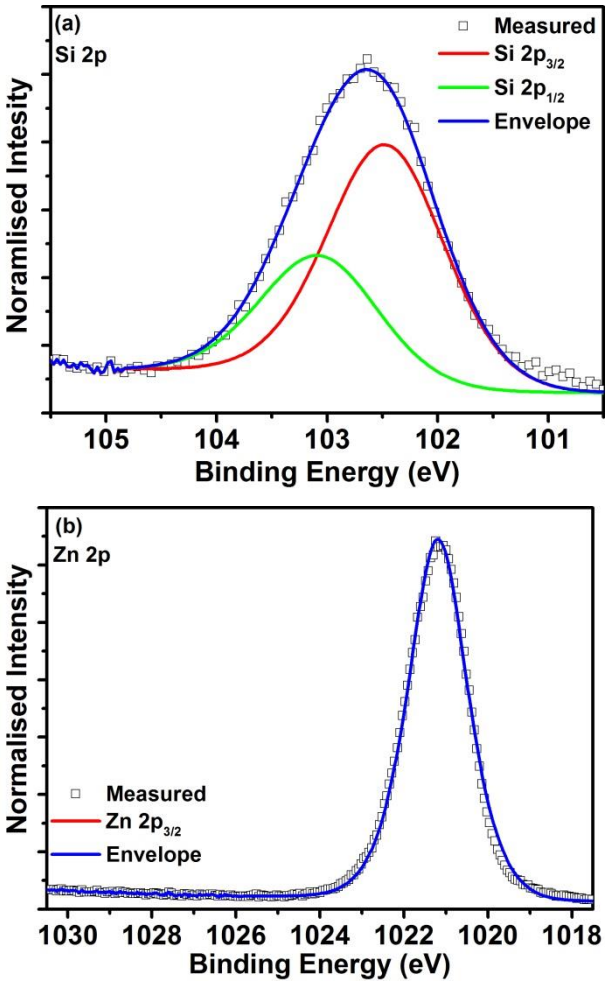

Fig. A.2 Core level spectra of (a) Si 2p and (b) for Zn 2p ZnO/SiO_2 interfaces

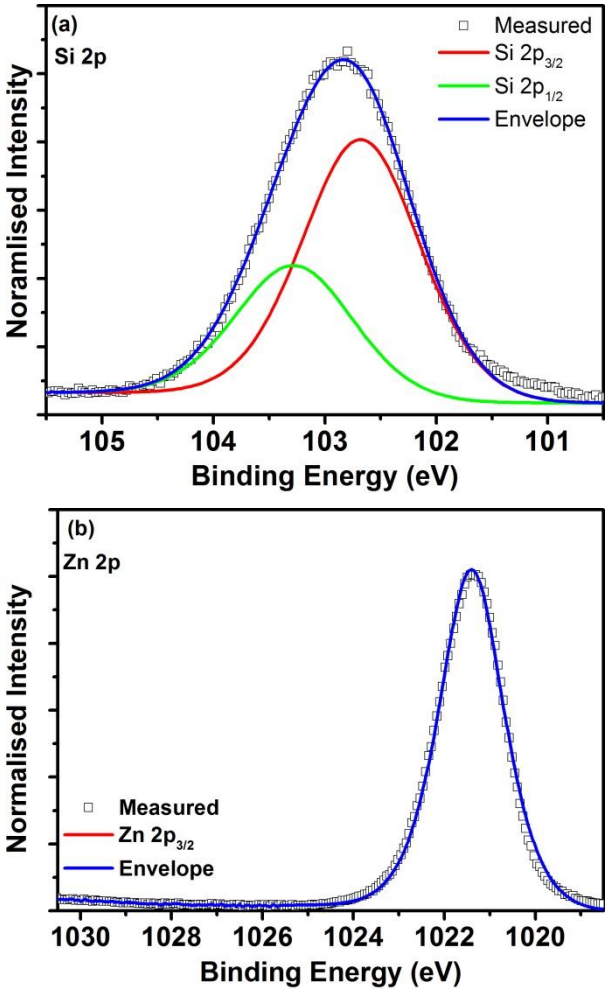

Fig. A.3 Core level spectra of (a) Si 2p and (b) for Zn 2p MgZnO/SiO_2 interfaces